Effect of Disk Structure on the Distribution of Water in Protoplanetary Disks and Planets

by

Anusha Kalyaan

A Dissertation Presented in Partial Fulfillment
of the Requirement for the Degree
Doctor of Philosophy

Approved November 2018 by the
Graduate Supervisory Committee:

Steven J Desch, Chair
Christopher Groppi
Patrick Young
Evgenya Shkolnik
James Bell

ARIZONA STATE UNIVERSITY

December 2018

ABSTRACT

The composition of planets and their volatile contents are intimately connected to the structure and evolution of their parent protoplanetary disks. The transport of momentum and volatiles is often parameterized by a turbulent viscosity parameter α, which is usually assumed to be spatially and temporally uniform across the disk. I show that variable α(r,z) (where r is radius, and z is height from the midplane) attributable to angular momentum transport due to MRI can yield disks with significantly different structure, as mass piles up in the 1-10 AU region resulting in steep slopes of p > 2 here (where p is the power law exponent in $\Sigma \propto r^{-p}$). I also show that the transition radius (where bulk mass flow switches from inward to outward) can move as close in as 3 AU; this effect (especially prominent in externally photoevaporated disks) may significantly influence the radial water content available during planet formation.

I then investigate the transport of water in disks with different variable profiles. While radial temperature profile sets the location of the water snowline (i.e., inside of which water is present as vapor; outside of which, as ice on solids), it is the rates of diffusion and drift of small icy solids and diffusion of vapor across the snow line that determine the radial water distribution. All of these processes are highly sensitive to local α. I calculate the effect of radially varying on water transport, by tracking the abundance of vapor in the inner disk, and fraction of ice in particles and larger asteroids beyond the snow line. I find one profile attributable to winds and hydrodynamical instabilities, and motivated by meteoritic constraints, to show considerable agreement with inferred water contents observed in solar system asteroids.

Finally, I calculate the timing of gap formation due to the formation of a planet in disks around different stars. Here, I assume that pebble accretion is the dominant mechanism for planetary growth and that the core of the first protoplanet forms at

the water snow line. I discuss the dependence of gap timing to various stellar and disk properties.

ACKNOWLEDGMENTS

I have wanted to be a scientist for a long time. But my path towards research in science was never linear nor was it obvious. Perhaps this is why I am bursting with gratitude towards so many people whose kindness helped me stay on it, and continue to achieve one of my wildest dreams:

My earliest mentors: Prof Subramanium Ananthakrishnan (NCRA), Prof Bhanu Pratap Das (then IIA), Dr Padmakar Parihar (IIA), Dr Ravinder Banyal (IIA) who went out of their way with their kindness by providing mentorship, support and opportunities for me to learn and grow, and Dr Banyal for his persistent kindness and faith in me;

Prof Murthy (PRL) who provided me the opportunity to pursue my first research projects in planetary astronomy;

My graduate committee members for their continuous support and advice throughout the past six years, and Chris for his valuable mentorship when it was needed;

Joan Najita and my future post-doc advisor Máté Ádámkovics for giving me an opportunity to continue working in the field;

My graduate and postgraduate colleagues who went out of their way to counsel me in times of difficulty - Jackie, Prajkta, Kim, Teresa, Svet, Marc, Lev, Maitrayee, Wanda, Chuhong, Aishwarya, Ed, Aprinda, Jon, Arundhati; My office-mates Aishwarya, Chuhong, Wanda, who made living in the office fun; Jackie and Rolf who took time out of their lives to train me in the extensive operational procedures of the VATT telescope;

My closest friends in India who kept in touch with me during the last six years in spite of myself;

My incredibly supportive extended family including my grandparents (I know it was not easy for you to let me stay so far away), adoring aunts and cousins;

My little sister, my GPS, who brings me back to earth, from wherever I am lost;

My amazing parents, who never tired of encouraging and supporting me through everything; moral boosts from dad; and long motivational talks from mom; could not have done this without you both;

My incredibly smart and kind PhD advisor, who never stopped supporting me, and persistently retained faith in me, with a lot of patience, during my numerous low-points. I am very grateful you took me on as your student. I learned so much working with you; so much of which I thought I never could. (And I am glad you now let me troll you about your 80s song-recognition skills);

Finally, my crazy partner, my rock, Nikhil, whose unwavering and unflinching presence, and whose constant faith in my abilities and my goodness has been my greatest source of strength during the last six years.

TABLE OF CONTENTS

CHAPTER Page

CHAPTER Page

CHAPTER Page

LIST OF TABLES

LIST OF FIGURES

Figure Page

Figure Page

Chapter 1

INTRODUCTION

1.1 Overview

It has long been known that the Sun, the Moon and the solar system planets all move in a small narrow strip across the sky. The periodic motion of the Sun and the planets across the distant background stars of the "Zodiacal Belt" has fascinated humans for centuries, giving birth to astrological studies that attempted to understand the effect of planetary motions on our everyday lives. However, it was only after we accepted the Sun-centric Copernican model of the solar system that we began to glean deep insights behind these simple observations and ultimately fathom the origin of the Sun, the planets, of life, and of ourselves. The motion of the Sun and other planets within nearly the same orbital plane led Kant and Laplace to hypothesize that our Sun was born with a disk of gaseous material from which the planets formed. This disk is now known as the "protoplanetary disk" and its existence has since been extensively verified by astronomical observations in the last few decades. The first detection of circumstellar material was made by the Infrared Astronomical Satellite (IRAS) in 1983 by the observation of infrared excesses over and above the black-body spectra of stars, which betrayed the presence of warm surrounding material. Later, the Hubble Space Telescope discovered photoevaporating protoplanetary disks, also known as proplyds in the Orion Nebula, illuminated in silhouette by the resident O-star θ^1 Ori C (McCaughrean & O'dell 1995). In fact, the discovery of hundreds of proplyds in the Orion Nebula, as well as thousands of exoplanets discovered by Kepler, has informed us that stars commonly form with these disks, which eventually

probably form planets.

In only the last few years, high resolution disk observations by the Atacama Large Millimeter Array (ALMA) has discovered structure (gaps, rings or warps) within disks around several neighboring stars (Van der Marel et al. 2015). A striking example is the multiple gaps observed in the dust disk around $\sim$ 1 Myr old HL Tau (ALMA Partnership et al. 2015). Observations of such structure in young disks show signs of advanced stages of solid growth and even the presence of a planetary companion capable of gravitationally clearing material. Such observations indicate that planet formation is well underway within the first few Myr.

Since planets are born within disks, disk evolution and planet formation are necessarily linked to each other. Planets are composed of the material that the disk is made of. Additionally, being highly dynamic systems, disks continually lose mass into the star, may viscously spread out or be gradually depleted by photoevaporation. Species such as small solids and volatiles are affected by additional physical processes such as particle drag or condensation. It is crucial to thoroughly investigate the behavior of physical processes during disk evolution, as these processes may have a significant impact on the composition of planets that form at different locations in the disk. In this respect, I argue that it is vital to consider the potential physical mechanism responsible for angular momentum transport that drives the evolution of the disk. Most disk models rely on an assumption of constant or uniform efficiency of turbulent transport in the disk. In this thesis, I try to deviate from this assumption and investigate what disks look like with non-uniform turbulent viscosity. I then attempt to understand how volatile transport and distribution can be different in such disks. I finally predict locations of gap formation in disks around different stars. The relative positions of gaps and the snow lines in these disks is likely crucial in dictating volatile contents of planets that form in the disk. Water is a key ingredient for the origin and

sustenance of life; therefore the study of water transport in disks would be beneficial to understand how much water planets may be able to accrete from the disk if they formed at various locations in the disk and at various times. This would ultimately help us ascertain the likelihood of habitable planets around different types of stars.

1.2 Formation of a Protoplanetary Disk

Many of the major theoretical ideas for the formation and evolution of the star and disk system are inspired by the study of our own Solar System and its planets. As mentioned before, it was first observed by Kant and Laplace that the solar system planets all orbit in the same direction around the sun, each deviating only by a small angle from a common orbital plane. It was therefore posited in the "nebular hypothesis" that stars formed from the gravitational collapse of a slowly rotating cloud of gas and dust. From this spherical envelope, gas infalling onto the stellar core at an angle to the axis of rotation would first fall onto a rotationally supported disk, which is then slowly transported through the disk to be accreted onto the star. Observations of disks in the last few decades inform us that these ideas are largely correct. Excesses observed in cooler wavelengths in spectral energy distribution (SED) profiles of stars reveal varying masses of circumstellar material present at different temperatures around the star. These SED profiles have provided a basis for classification of these objects based on the power law slope of the SED between 2 and 25 μm (Lada et al. 1987). Objects that show a slope greater than about 0.3 are classified as Class I, where the mass of the disk and the envelope are comparable. Objects with slope between 0.3 and -0.3 are known as Class II, undergoing a more advanced stage of evolution where most of their envelope has dissipated (Williams & Cieza 2011). High-resolution observations also reveal rotational velocity profiles for the material infalling from the surrounding envelope onto the disk distinct from those present in

the disk. The former shows $v_{\rm rot} \propto r^{-1}$, while the latter shows $v_{\rm rot} \propto r^{-0.5}$ consistent with Keplerian rotation for a disk (Li et al. 2014).

Upon further scrutiny however, this theory runs into a critical problem: it does not explain how a collapsing cloud core could lead to a planetary system where the planets carry 99% of the angular momentum while the star has almost all of the mass of the system (Mestel 1965 a,b). Extensive study has since shown that formation of a disk is most likely not merely a result of only hydrodynamic collapse as described above, but rather the collapse is affected by the presence of magnetic field in complex ways. It is still not known clearly how infalling material from the envelope is able to lose sufficient angular momentum to reach the stellar core. Many possible mechanisms of "magnetic braking" are being extensively investigated in the literature including the effects of non-ideal magnetohydrodynamics (MHD), turbulence, and magnetic field and rotation misalignment (Li et al. 2014). However, it is important to distinguish a truly rotationally supported structure with that of a flattened structure produced when magnetic field lines frozen into the gas are dragged inward as the gas collapses onto the core, known as the pseudo-disk (Galli & Shu 1993; Belloche et al. 2013; Li et al. 2014).

Recent high-resolution observations have confirmed the presence of a centrifugal barrier (Sakai et al. 2014), the radius at which the centrifugal force and gravitational force on the rotating material are equal to each other. At this radius, only if angular momentum is extracted in some way will the material flow inward towards the star. Still more recent observations of molecular emission in CCH and SO show that at the centrifugal barrier, movement of gas is slowed and then pushed vertically away from the midplane, hinting at the possibility of outflows at this radius (Sakai et al. 2017). With more detailed numerical calculations and still more high-resolution ALMA observations on the way, we are on the brink of new insights in our understanding of

disk formation at the very early stages.

1.3 Evolution of the Protoplanetary Disk

After the envelope dissipates, the rotationally stable disk with mass roughly tenth that of the star slowly accretes onto it. This proceeds for a few Myr until most of the gas is accreted or dispersed. It is during this time that there exists a quasi-stable environment for the growth of particles and planetesimals, and planetary embryos, the precursors of planets. The masses of planets, where they form, and how rapidly they grow are all dependent on the physical conditions in the disk such as the surface density and temperature at each radius r. They are also dependent on how efficiently mass is transported through the disk and therefore dependent on the dominant mechanism of angular momentum transport in operation, as well as how long gas persists in the disk before being dissipated away. In this section, I briefly discuss the above topics, especially as it relates to the research work that is presented in this thesis. I will in particular discuss some common assumptions made in the research presented in the following chapters:

1.3.1 Surface Density (Σ) Profile

The knowledge of the distribution of mass with distance from the star is crucial for modeling the formation of planets. This is usually denoted in terms of the surface density or Σ, which is equal to the vertically integrated density at each r, as follows:

$$\Sigma(r) = \int_{-\infty}^{\infty} \rho\,(r, z)\; dz \tag{1.1}$$

It is difficult to constrain $\Sigma(r)$. Only recently has it been possible to infer $\Sigma(r)$ from observations. Andrews et al. (2009, 2010), assuming $\Sigma(r) \propto r^{-p}$, find power law slopes of 0.4 to 1.1, with a median value ≈ 0.9 in disks in Ophiuchus. One also may infer $\Sigma(r)$

from the knowledge of masses of the Solar System planets; smearing the planet mass at their current orbital locations and augmenting them to solar composition reveals a profile that is commonly known as the minimum mass solar nebula (MMSN); given as follows:

$$\Sigma_{\rm MMSN} = 1700\left(\frac{r}{r_0}\right)^{-1.5} {\rm g\,cm^{-2}}. \quad (1.2)$$

The assumptions of the MMSN profile may underestimate Σ, as it does not include the mass of solids that did not end up in the final eight planets. It also assumes that planets formed at their current orbital locations. In this thesis, I have assumed $\Sigma(r)$ to be uniformly more massive throughout the disk ($\sim 5\times$ MMSN), resulting from the assumption of a more compact configuration of formation locations of planets before the giant planet instability predicted by the Nice Model (Gomes et al. 2005). This compact configuration adopted from Desch (2007) assumes that all the planets formed within a radius of 15 AU, and then spread outward with time. With Kepler's extensive dataset of multiple planetary systems, this analysis has been repeated for exoplanetary systems to retrieve a Minimum Mass Extrasolar Nebula, which is more or less is similar to that inferred from MMSN (Chiang & Laughlin 2013; Raymond & Cussou 2014) albeit with assumptions made for planet composition and mass (usually inferred from a radius from an assumed mass-radius relation).

1.3.2 Temperature Profile T(r)

There are two dominant sources of heating in a disk. The disk is either heated solely by the irradiation from the central star, or it is also able to generate some heat on its own via viscous dissipation. While the former is dependent on stellar properties such as stellar luminosity and mass as well as distance from the star, the latter is dependent on disk properties, such as surface density, disk viscosity and the opacity of its material at each r. In the presented studies, I have assumed either only the case

of a passively irradiated disk, or only the accretional heating, or both, summing both the thermal contributions in quadrature. Accretional heating dominates closest to the star. In cases where both are considered, a transition can be seen at a particular radius $r_{\rm vp}$ where the temperature profile returns to the shallower passively irradiated $T(r)$. In only the case of the disk that is heated by viscous accretion, temperature has an effect on mass transport. In addition, temperature also specifically affects the transport and distribution of condensible volatiles such as water by determining where the disk was cold enough for it to condense and where it was not.

1.3.3 Angular Momentum Transport

Despite extensive research efforts in the last two decades, it is not certain what physical mechanism transports angular momentum and drives disk evolution. Molecular viscosity is an unlikely candidate for momentum transport as if it were so, then disks would take too long to evolve with the typical gas densities (Armitage, 2017). Turbulent viscosity, however, can yield viscous timescales of ~ 1 Myr, consistent with observations (Hartmann et al. 1998), and disk models evolving the evolution equations of Lynden-Bell & Pringle (1973) often use a standard prescription of disk viscosity where viscosity ν is considered to be a dimensionless factor α times the product of sound speed c_s, taken here to be the maximum speed of turbulent eddies and disk scale height H, taken here to be the maximum size of the eddies. This prescription though vague (it could represent slow, large eddies or small, fast-moving eddies) has been widely used in disk evolution models as it relieves the modeler from assuming any physics behind the turbulence.

Until recently, magnetorotational instability (MRI; Balbus & Hawley 1992) was widely accepted to be the dominant mechanism behind angular momentum transport. In Chapter II (Paper I), the presented work assumed MRI viscosity to calculate

a radially-varying efficiency for transport of mass and momentum in order to determine the resulting disk structure. It is now not certain if there may be any regions in the disk where the MRI is not completely suppressed by the action of non-ideal magnetohydrodynamic effects such as ohmic resistivity, ambipolar diffusion and the Hall Effect (Bai & Stone 2013; Bai 2014; Bai et al. 2017; Gressel et al. 2015; Simon et al. 2015), and is now the consensus that perhaps disks are dominantly driven by the action of magnetic winds (Bai 2014; Suzuki et al. 2016). With recent advances in 3D computational calculations, it has also been found that a variety of hydrodynamic instabilities are capable of producing turbulence corresponding to $\alpha = 10^{-4}$ throughout the disk, even in poorly ionized dense midplane regions known as the dead zones. I discuss the latest research pertaining to these advancements in detail in Chapter III (Paper II), and accordingly consider three distinct $\alpha(r)$ profiles, one with constant α and two with radially varying α profiles inspired by these recent developments, to investigate their effect on volatile transport.

1.3.4 Disk Dissipation

An important consideration for planet formation models is the time available for planets to accrete surrounding disk material in their vicinity, i.e., time until the gas disk dissipates. This is related inextricably to all of the above-mentioned disk properties such as: i) the initial mass available in the disk and the radius at which the planet forms; ii) efficiency at which viscous accretion is able to transport mass through the disk, which is dependent on α (or $\alpha(r)$, if radially varying); and iii) the temperature $T(r)$ if the disk is heated by viscous dissipation, which is also dependent on $\alpha(r)$. It is, however, also dependent on some additional processes that may remove gas from the disk causing a local depletion of gas, such as the presence of a nearby massive star, as in the Orion Nebula, or the presence of growing protoplanet. The

intense irradiation from the O star in the Orion Nebula has been linked to high mass-loss rates (Henney & O'Dell 1999) and low observed masses of the proplyds (Mann et al. 2014). In Chapter II (Paper I), I discuss various compelling lines of evidence to argue that the solar disk itself could have been externally photoevaporated. I include a prescription for mass loss rate by photoevaporation from the outer edge of the disk from Adams et al. (2004), and study the effect on the structure of the outer disk. In this work, I did not consider photoevaporation that could result from the radiation of the central star itself, which is especially important to consider at later stages of disk evolution ($>$ few Myr). However, several studies have modeled the effect of central photoevaporation on disk evolution and dissipation (Anderson et al. 2013; Gorti et al. 2009, 2015). Gorti et al. (2015) find that central photoevaporation most efficiently removes mass from the disk at a few AU from the star when the rates of accretion and mass removal through the photoevaporative wind are comparable ($\sim$ few Myr). At this location, the gas disk is eventually depleted to form a gap.

A gap in the disk can also be produced by a growing protoplanet. Rapid growth of protoplanetary cores can be achieved via pebble accretion (Johansen & Lambrechts 2017). When such a body is massive enough to start accreting gas in its vicinity, it eventually carves a gap in the gaseous disk. A gap whether formed by a protoplanet or photoevaporation is likely to substantially alter disk lifetimes by starving the inner disk of material from the outer disk, as well as leaving the outer disk isolated and exposed to direct sources of radiation. This would result in quicker disk dissipation that would also halt the supply of disk material toward further growth of other planetary cores.

1.4 Radial Transport of Volatiles

Snow lines are the regions in the protoplanetary disk that demarcate where temperature and pressure conditions allow condensable volatiles (such as water) to either be present as vapor or as ice on solid particles. The water snow line is often considered critical for initiating planet formation in the disk. This is because solid particles with water ice on their surfaces tend to be more "sticky" than bare silicate particles (Gundlach & Blum 2015). Effective sticking of icy particles, as well as the backward diffusion of vapor through the snow line and subsequent condensation onto solids (Ros & Johansen 2013) also can increase the density of solid particles at the snow line. Higher solids-gas ratios here can trigger the onset of streaming instability that can lead to the rapid growth of small mm-cm sized solids to meter-size and larger (Johansen et al. 2007). Temperature and pressure conditions in the disk mainly determine the location of the water snow line. However, rates of diffusion and drift of solids icy particles as well as diffusion of vapor across r can significantly affect the transport and distribution of water in the disk. Across the snow line region, water vapor tends to diffuse outward to eventually condense as ice onto surfaces of small solid particles beyond the snow line. Icy particles from the outer disk drift inwards on facing the headwind from the pressure-supported gas that causes them to spiral inwards. Upon crossing the snow line, the ice on them sublimates to replenish some of the vapor that was earlier lost by outward diffusion. The rates and timescales of these two competing processes are regulated by the α parameter and its radial variation as discussed above. In Chapter III (Paper II), I motivate the use of three α profiles as follows: i) uniform α profile for comparison, ii) α profile derived from the magnetorotational instability as used in Chapter II (Paper I); and iii) an α profile derived from cosmochemical constraints as discussed in Desch et al. 2018 (contributed-Paper

V). I use the detailed formulations for the radial diffusion and advection motion of volatiles and solids as discussed in Desch et al. 2017 (contributed-Paper IV). I found that the radial variation of the α parameter and its gradient across the snow line are critical in determining the effective flow of water across the snow line and can be extremely insightful to understand the bulk water abundances of planets formed at different radial distances from the star.

1.5 Other Contributed Work

The following is a list of papers I have co-authored that are pertinent to the topic of this thesis. These papers mark some key intermediate theoretical and numerical developments that benefited and provided key insights to the later works presented in this thesis. I summarize the main results of both papers as well as my contributions to each in the following subsections.

1.5.1 Desch et al. (2017): Formulas for Radial Transport in Protoplanetary Disks

The topic of radial transport of volatiles has been investigated by several research works in the last few decades (Stevenson & Lunine 1988; Gail 2001; Cuzzi & Zahnle 2004; Guillot & Hueso 2006; Ciesla & Cuzzi 2006; to name a few). These works, however, adopt varying numerical treatments that are distinct from each other. Among these works exist treatments that ignore a gradient in density or diffusion coefficient (Stevenson & Lunine 1988; hereafter SL88) or treat vapor in the same manner as the bulk gas of the disk, rather than a tracer component in it (Guillot & Hueso 2006; Ciesla & Cuzzi 2006; hereafter GH06/CC06). Among the nine works reviewed by Desch, Estrada, Kalyaan & Cuzzi (2017; hereafter D17) existed six distinct, original treatments of volatile transport. D17 assumed the volatile to be a tracer in the bulk disk gas and derived the advection-diffusion equations for volatiles in the disk using

the Fick's Law of Diffusion from first principles, to arrive at the following equation for radial transport rates of the tracer species (subscript c);

$$\dot{M}_{\rm c} = c\,\dot{M} + 2\pi r\,\mathcal{D}_{\rm g}\,\Sigma\,\frac{\partial c}{\partial r}, \tag{1.3}$$

Here, c denotes concentration of the tracer species and $\mathcal{D}$ is its diffusivity. In this equation, derived first by Clarke & Pringle (1988) the first term on the right hand side deals with advection, and second term deals with diffusion of the tracer species. The following equation shows the evolution equation of this species with time, when the Schmidt number is considered to be $\sim$1 (i.e., when viscosity ν is equal to the diffusivity D of the volatile species).

$$\frac{\partial c}{\partial t} = \nu\left[(\frac{5}{2} + 4Q)\,\frac{1}{r}\frac{\partial c}{\partial r} + \frac{\partial^2 c}{\partial r^2}\right]. \tag{1.4}$$

For particles, an additional term for particle drift is applied, to result in the following equation:

$$\dot{M}_{\rm c} = c\dot{M} - 2\pi r\,c\Sigma\,(\Delta u) + 2\pi r\,\mathcal{D}_{\rm p}\,\Sigma\,\frac{\partial c}{\partial r} \tag{1.5}$$

Here, drift velocity (with respect to the velocity of the bulk gas) is given as Δu, where:

$$\Delta u = V_{{\rm p},r} - V_{{\rm g},r} = \frac{-{\rm St}^2\,V_{{\rm g},r} - \eta\,{\rm St}\,r\,\Omega_{\rm K}}{1 + {\rm St}^2}, \tag{1.6}$$

Here St is the Stokes number of the particle, a dimensionless quantity to quantify how aerodynamically coupled to the gas a particle is in a flow, and therefore that depends on particle properties such as particle size and density, and the density of the medium it flows in (such as the gaseous surface density in the disk).

D17 found that their results matched that of previous works of Clarke & Pringle (1988), Gail (2001) and Bockelee & Morvan (2002). I compared two distinct treatments with that adopted in our work, by incorporating each into the same disk evolution model, and determining how quickly vapor in an annular region diffused

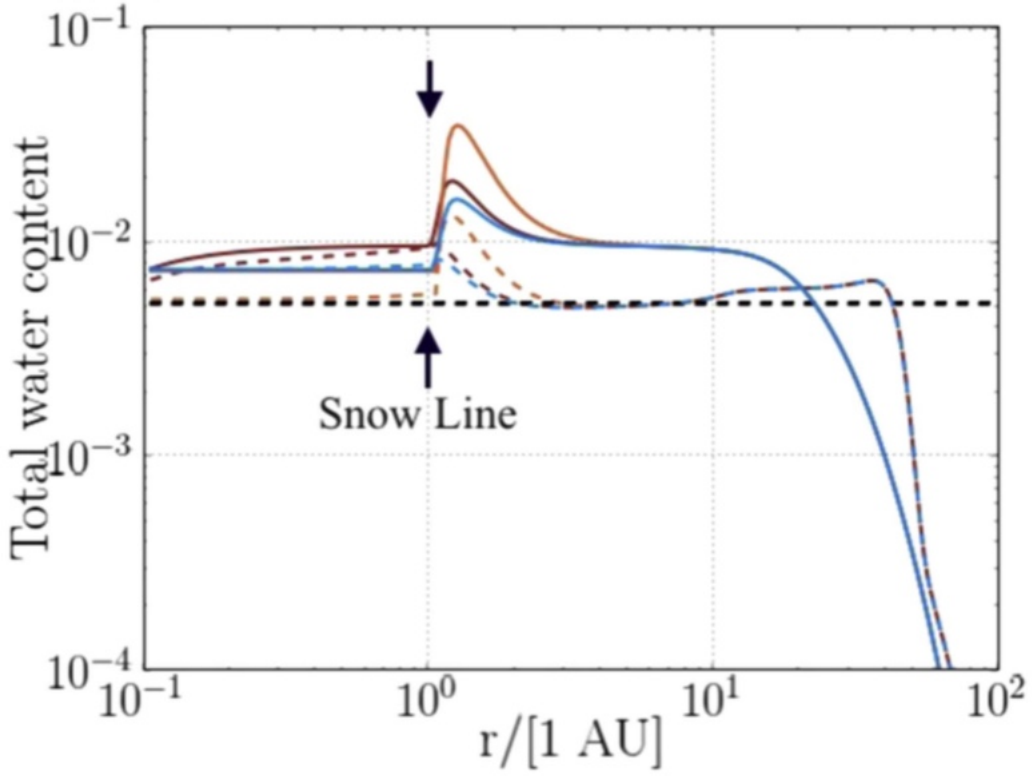

Figure 1: Simulated evolution over time of the total water abundance across disk radius r. Total water abundance implies abundance of water in vapor, chondrules and asteroids per unit bulk H_2 gas. Blue profiles show 0.1 Myr (dashed) and 1Myr (solid) with the formulation used here (cf. Gail 2001). Orange profiles similarly show treatments incorporated by GH06/CC06, and brown profiles show that by SL88. The sharp drop in the concentration at ~ 1 AU denotes the location of water snow line, within which all water is vapor, and outside of it as ice on solid bodies. The different formulations yield similar, but quantiatively different results.

through the rest of the disk in each case. I also incorporated the three treatments in a snow line model that incorporated volatile and particle diffusion, inward drift of icy particles as well as phase change of vapor/ice. I compared the abundance of ice (with respect to bulk gas) present in each case beyond the snow line. Figure 1 shows subtle differences in the quantity of ice that accumulates beyond the snow line for three different treatments of volatile transport.

1.5.2 Desch et al. (2018): Effect of Jupiter's Formation on the Distribution of Refractory Elements and Inclusions in Meteorites

Recent work by Kruijer et al. (2017) (building over previous work by Warren (2011) had suggested that within 1 Myr, there may have been two distinct isotopic reservoirs in the solar nebula. They posited that this likely resulted from the formation of Jupiter's core that attained sufficient mass enough to carve out a gap in the gaseous nebula. Motivated by this study, Desch, Kalyaan & Alexander (2018; hereafter D18) proposed a comprehensive disk model that modeled the diffusive transport of refractory inclusions first created in the innermost hot disk. Although most of the refractory particles are accreted onto the star, some diffuse through the rest of the disk. Once the gap is formed at a distance of few AU (similar to Jupiter's current location in our own nebula; ~ 3 AU), a pressure bump beyond the gap is also formed. As drifting particles drift toward a negative pressure gradient, they are accumulated and trapped here, where these inclusions are eventually incorporated into carbonaceous chondrites. I contributed to the disk modeling for this paper, which necessitated an extensive parameter study that yielded a disk model consistent with many known meteoritic findings, including known refractory abundances and water ice fractions in various chondrites. Anchored by these findings, our disk model is able to predict the timing and location of formation of 5 achondrite and 11 chondrite bodies, as shown in Figure 2. Our model also constrains a radially varying turbulent viscosity profile that is required for the observed distribution of refractory inclusions in different chondrites. I show a schematic of our model here, reproduced from the corresponding paper:

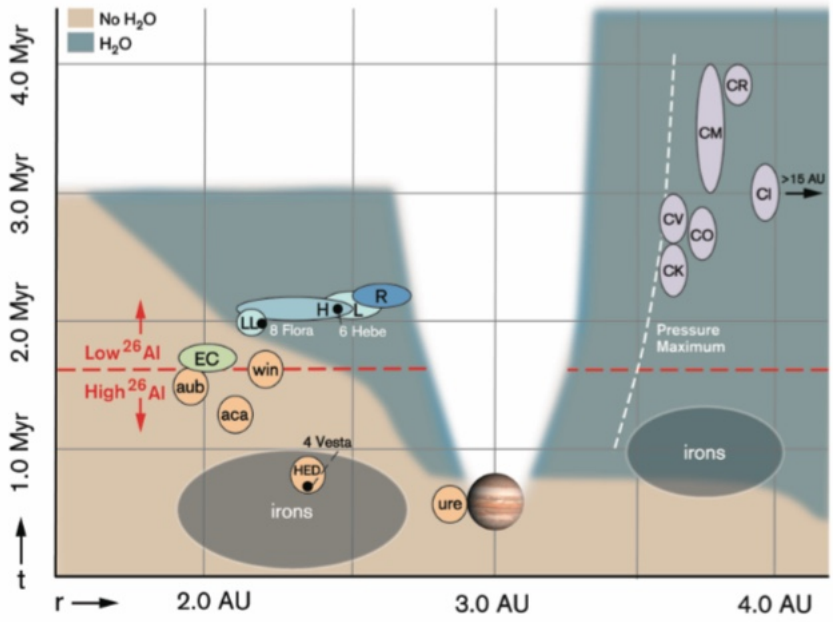

Figure 2: Schematic depicting the formation locations and times of 6 achondrites (ureilites, howardite-eucrite-diogenites (HED), acapulcoite-lodranites, aubrites, winonaites; orange circles) and 11 chondrites (enstatite (EC; green circle), ordinary (LL, L, H; blue circles) and carbonaceous chondrites (CK, CV, CO, CM, CR, CI; lavender circles) as well as Rumuruti chondrites (R; dark-blue circle). Red line denotes which bodies formed with a high/low abundance of Al-26. Brown indicates times and disk regions that were warm; blue indicates times and regions cold enough for vapor to be condensed as ice. The transition between the two tracks the snow line as it moves inward through the disk with time. At $\sim$ Jupiter clear a gap and thereafter strongly influences transport of inclusions, resulting in this depicted scenario.

1.6 Key Questions and Overall Organization

In this section, I will briefly discuss three key questions that I have addressed in this work and briefly summarize the general results obtained. I will also point out which chapters contain results pertaining to each question.

1.6.1 How do disks evolve with non-uniform α, photoevaporation and gaps evolve?

It is likely unrealistic to expect disks to evolve with a constant global α. Unfortunately, in the absence of information regarding the angular momentum transport mechanism behind disk evolution, most disk models have preferred to assume radially

and temporally constant α. Nevertheless, it is imperative for models to go beyond this assumption and explore what disks may look like with non-uniform α. In this regard, I have considered two radially varying α profiles: (i) MRI-α profile; and (ii) a Hybrid α profile. Chapter II (Paper I) discusses the disk structure and evolution of disk model with an MRI-α profile in detail, while Chapter III considers a hybrid $\alpha(r)$ that is attributable to disk winds and hydrodynamic instabilities. I compare both models with that of the standard uniform α disk and find significant deviations in the Σ structure of these disks compared with the uniform case. While the MRI-α profile yields a disk with a steep $\Sigma(r)$ profile ($p > 2 - 3$), the hybrid case consisting of a more turbulent inner disk region yields a flat $\Sigma(r)$ ou to 20 AU.

Besides non-uniform turbulent viscosity, disk structure is also affected by the presence of photoevaporation and growing planets. In Chapter II, I have explored the effect of external photoevaporation due to a nearby massive star on disk structure and have found that photoevaporation results in truncation of the outer disk radius as well as a slightly steeper disk profile ($p \sim 1.6$); though not as drastic as the effect of non-uniform α. In Chapter IV, I have explored the structure of disks with a gap formed by a growing protoplanetary core. I have determined that a growing core strongly affects the local gaseous structure, but has little effect on it far away from the gap, as gas is still slowly transported through the gap. This is not true for the distribution of solids as discussed in D18.

1.6.2 How is water transported in disks?

It is not known how water is transported in disks with non-uniform α. In Chapter III, I therefore investigate this question by considering disk models with the α profiles discussed before and overlay a volatile transport model that incorporates condensation and evaporation of volatiles at their snow line, diffusion of volatiles and particles and

drift of particles, as well as a simple parameterized growth of particles into larger bodies. This disk + snowline model incorporates the advection-diffusion equations as discussed in D17 (and earlier in this chapter) and tracks the vapor content in the inner disk and water to rock ratios in small particles and asteroids formed beyond the snow line at various times. I discuss consistencies of the resulting model water distribution with known water ice fractions of asteroids in the solar system.

1.6.3 Do the largest planets always form at the snow line?

Finally, in Chapter IV, I embarked on a numerical investigation of the radial efficiency of planet growth by pebble accretion. In this study, I investigated how long it would take for a core growing by pebble accretion to attain pebble isolation mass. I found that the there is a unique region in the disk where time taken for a core to form a gap (assumed to be close in time to when the core attains isolation mass) in the disk is minimum, and exists at the boundary of the region where the disk transitions from an inner disk largely heated by viscous dissipation to a cooler outer disk heated mainly by irradiation from the central star. This leads to an interesting insight that the snow line is perhaps not the only region where the first (and therefore the largest) surviving planets may form.

1.7 Summary

The primary motivation of the presented thesis work is to understand what might be the physical conditions that are relevant to planets formed in the protoplanetary disk around their stars, and what factors might influence if they could be habitable for life. Water is argued to be a bio-essential component for life on earth, and therefore possibly determines the habitability of an exoplanet. I have explored what may have been the primordial bulk water distribution in the solar nebula by considering

physical effects not included before in previous disk models, such as variable turbulent α viscosity profiles. I have also investigated where the first protoplanets may form in disks around different stars. Gaps created in disks by protoplanets may affect the bulk water content in closer-in rocky planets in those planetary systems. This is analogous to the study of our own Solar System terrestrial planets whose water content was very likely dictated by altered physical processes induced by the gap created by Jupiter. This thesis work is organized as follows: Chapter II is a reproduction of the work *Kalyaan et al. (2015)* published in *The Astrophysical Journal*; Chapter III is a reproduction of the prepared work about to be submitted to *The Astrophysical Journal*; Chapter IV is a report of analytical and numerical findings prepared for future publication into *The Astrophysical Journal*; and, finally, Chapter V discusses important conclusions of the presented research work.

Chapter 2

EFFECT OF NON-UNIFORM TURBULENT VISCOSITY AND EXTERNAL PHOTOEVAPORATION ON DISK STRUCTURE AND EVOLUTION

The following chapter is a reproduction of the publication Kalyaan et al. (2015) titled: *External Photoevaporation of the Solar Nebula II: Effects on Disk Structure and Evolution with Non-Uniform Turbulent Viscosity due to the Magnetorotational Instability*. It is formatted for inclusion into this document.

2.1 Introduction

Protoplanetary disks form around low mass stars as a consequence of stellar formation when collapse of a slowly spinning molecular cloud core transforms it into a rapidly rotating star-disk system. Once formed, the disk undergoes viscous evolution via shearing stresses that are set up through differential rotation of its gas and dust constituents. Much of the disk mass flows inward and accretes onto the star, while simultaneously a portion of its mass is transported far outward (to conserve angular momentum), causing the disk to continuously spread outwards throughout its ~ 10 Myr evolution (Pringle 1981). Planetesimals and planetary cores form via coagulation and accretion of the remaining dust and gas on timescales of a few Myr or less, before the disk is dissipated. All of these processes, and the mass available for planet formation, rely on the details of how matter is moved through protoplanetary disks. The surface density profile $\Sigma(r)$ - or mass per area of disk as a function of distance from the star r - determines how much of mass might have been available in the feeding regions of the planets; its evolution over time determines how mass moves in the disk and also how the planetary masses grow. Theoretical models of disk evolu-

tion are based on the canonical equations by Lynden-Bell & Pringle (1974; hereafter LBP). These models assume that the disk evolves via shearing stresses mediated by a turbulent viscosity ν that varies as $\nu \propto r^{\gamma}$ where $\gamma \sim 1$. They predict that $\Sigma(r,t)$ should approximate a power law $\Sigma(r) = \Sigma_0(r/r_0)^{-p}$ across much of the disk, with slope $p \sim 1$. Model predictions of disk integrated properties appear consistent with observations of disks in low mass star forming regions such as Taurus (Hartmann et al. 1998). Observations of resolved disks, on the other hand, can provide direct estimates of $\Sigma(r)$. Recent work with millimeter wavelength surveys of disks in another low-mass star forming region, Ophiuchus (Andrews et al. 2009; Andrews et al. 2010), fit $\Sigma(r)$ to a profile $\Sigma \propto (R/R_c)^{-\gamma}\exp[-(R/R_c)^{2-\gamma}]$ (R_c is the characteristic radius where the shape of the Σ profile changes from the power-law to the exponential taper) which is similar to the LBP similarity solutions, and find γ to be within the range 0.4 - 1.1, with a median value of about 0.9. This seems to be consistent with theoretical predictions of $\Sigma(r)$ of viscously evolving disks. Despite this tentative match, one must use caution when inferring the distribution of mass from such observations. It is not even certain that all the mass is being observed, as several factors may lead to the disk mass in any annulus being underestimated. The millimeter opacity of solids is sensitive to changes in grain size and composition (Beckwith et al. 1990, Beckwith & Sargent 1991). Converting a solids mass to a mass of gas requires knowledge of the uncertain dust-to-gas mass ratio. Also, some massive disks may still be optically thick in the sub-mm regime, hence shadowing some of the disk mass (Andrews & Williams 2005). Sub-mm observations are also not sensitive to >mm-sized dust grains, and hence may not account for mass locked up in larger grains, or even planets that have already formed, as they will remain undetectable for several Myr. Thus it is difficult to definitively derive $\Sigma(r)$ from astronomical observations.

Although the Sun's protoplanetary disk has long ago dissipated, an estimate of

$\Sigma(r)$ (in a snapshot or time-averaged sense) can be obtained from the known masses and compositions of the planets. Weidenschilling (1977b) and later, Hayashi (1981) developed the so-called Minimum Mass Solar Nebula (MMSN) model in which an estimate of the surface density profile of the solar nebula is found by augmenting the known mass of each planet (located in its present day orbit) with H_2/He gas to bring it to solar composition, and then dividing this augmented mass by the area of the annulus in which it orbits. An estimate of $\Sigma(r)$ is found at each planet's radial location r, and a power law can be fit to these points. A widely used equation for the MMSN model put forward by Hayashi (1981) is :

$$\Sigma(r) = 1700 \left(\frac{r}{1\,\mathrm{AU}}\right)^{-3/2} \mathrm{g\,cm^{-2}}. \tag{2.1}$$

Later, this model was extended to extrasolar planetary systems as the Minimum Mass Extrasolar Nebula (MMEN) model (Kuchner 2004; Chiang & Laughlin 2013; and Raymond & Cossou 2014), using some of the > 470 known multiple planet systems. For such close-in planetary systems, $\Sigma(r)$ can only be inferred up to a few AU. Chiang & Laughlin (2013) find the slope of $\Sigma(r)$ to be $p \sim 1.6$ - 1.8, while Raymond & Cossou (2014) argue that $\Sigma(r)$ varies wildly amongst planetary systems and ~ 1.6 is only a median value. With future data from more widely separated planetary systems, any universal or median MMEN will provide for much better comparison with the MMSN model than current data. The slopes for $\Sigma(r)$ inferred from the MMSN and MMEN models, $p \approx 1.5$-1.6, are steeper than the slope of the profile measured from observations or predicted by theory. However, the MMSN and MMEN models suffer from many shortcomings. For the MMEN model, there are large uncertainties or lack of data on mass, radii and the composition of planets, and drawing out a surface density profile mandates assuming a uniform (usually chondritic) composition, and usually a mass from a known radius assuming a mass-radius relation (Chiang &

Laughlin 2013). It also inherently assumes that the planets were formed where they are now observed. As for the MMSN, while it offers a direct reference measurement of $\Sigma(r)$ from our own solar system, it only accounts for the minimum amount of mass in the solar nebula that was sequestered into the final planets. It assumes that no solids were lost from the nebula throughout its evolution and also only samples the disk at one given point in nebular history, i.e., after the outer planets assumed their final positions in their current orbits. Both the MMSN and the MMEN models do not account for the migration of planets in the disk, when numerous observations of close-in hot massive planets in exoplanetary systems suggest significant planetary migration driven by exchange of angular momentum with the disk gas as well as planetesimals (Armitage 2007; Crida 2007; Walsh et al. 2011; Kley & Nelson 2012). Planetary migration, if present, can later dramatically modify the initial surface density profile that was available for planet formation.

It was in this context that Desch (2007) argued that the dynamical constraints from the Nice Model (Tsiganis et al. 2005; Gomes et al. 2005; Morbidelli et al. 2005) at $\sim$ 880 Myr after the formation of the disk provide for an MMSN model better suited for studying the structure of the early disk. The Nice Model argues that the giant planets are likely to have formed from a more compact configuration, at 5.45, 8.18, 11.5 and 14.2 AU for Jupiter, Saturn, Neptune and Uranus respectively (in which the two ice giants likely swapped places). Substantial migration of outer planets eventually led to their final positions today, spread across 5-30 AU. With this configuration, the Nice Model successfully explains many dynamical constraints of the solar system including the observed orbital parameters of the giant planets, as well as the halt of Neptune's migration, dynamical classes of the Kuiper Belt, origin of the Jovian Trojan asteroids and the Late Heavy Bombardment. Desch (2007) used these updated positions of the giant planets in the MMSN model to find a $\Sigma(r)$ profile

that was steeper than the MMSN model with a slope of $p \sim 2.2$:

$$\Sigma(r) = 343 \left(\frac{f_p}{0.5}\right)^{-1} \left(\frac{r}{10\,\mathrm{AU}}\right)^{-2.168} \mathrm{g\,cm^{-2}}, \tag{2.2}$$

where f_p is a factor describing the fraction of solids in dust at the end of planet formation. This compact architecture results in a higher $\Sigma(r)$ throughout the disk and also in a steeper Σ profile. Desch (2007) found that such a steep profile matches very well with the solution of a steady-state *decretion disk* (Lee et al. 1991) i.e., a disk which is losing mass radially *outward*. He argued that this disk mass loss process can be explained very well by photoevaporation due to intense far ultraviolet (FUV) radiation from a nearby massive star.

Photoevaporation is an efficient mechanism for disk dispersal, in which the disk is impinged by external extreme-ultraviolet (EUV) or FUV radiation that causes the gas in the upper atmosphere of the disk to heat to $\sim 10^2$ K and escape the gravitational potential of the star. It was directly observed in the Trapezium cluster of the Orion Nebula where disks close to θ^1 Ori C (the O star in the Orion Nebula) were not only found to be truncated (McCaughrean & O′Dell 1996) but also were observed to be losing mass steadily with mass-loss rates of up to $\sim 10^{-7}$ $\mathrm{M_\odot\,yr^{-1}}$ (Henney & O′Dell 1999). Recent Atacama Large Millimeter Array (ALMA) observations by Mann et al. (2014) rule out any observational bias and confirm a distinct lack of massive disks close to the O star ($\sim$ 0.03 pc). Disks born in low-mass star forming regions (like Taurus or Ophiuchus) however, viscously spread to large radii $\sim$ 300 AU (Hartmann et al. 1998; Andrews & Williams 2007; Andrews et al. 2009, 2010), in contrast to truncated photoevaporated disks.

It is very likely that the Sun's protoplanetary disk experienced photoevaporation. From observations of nearby clusters, it is expected that roughly 50% of all disks are likely to be present in intensely irradiated birth environments with sufficient

FUV flux to cause significant mass loss via external photoevaporation (Lada & Lada 2003). The abundances of short-lived radionuclides that are more likely to have been created in nearby supernovae (Wadhwa et al. 2007) and then injected into the solar nebula (Ouellette et al. 2010; Pan et al. 2012) very likely betray the presence of nearby massive stars. The orbit of Sedna also suggests that it is likely to have been perturbed inward into the solar system due to a nearby passing star (Kenyon & Bromley 2004). The edge of the Kuiper Belt at ∼47 AU is also consistent with a disk that is seemingly truncated in a clustered environment, which could be attributed to either cluster dynamics where a passing star strips material off of the disk (Clarke & Pringle 1993; Kobayashi & Ida 2001; Adams 2010) or truncation due to photoevaporation (Trujillo & Brown 2001; Hollenbach & Adams 2004). Finally, the oxygen isotope anomalies found in Ca-Al inclusions in meteorites is likely resolved by an isotopically selective fractionation caused by the self-shielding of CO against photodissociation by external FUV radiation (Lyons et al. 2009). It has also been argued that external FUV radiation is also likely to create enormous quantities of amorphous ice in the cold outer disk (Ciesla 2014; Monga & Desch 2015) that will be able to trap noble gases, which upon radially migrating inward lead to the noble gas abundances measured by the Galileo mission in Jupiter's atmosphere (Monga & Desch 2015). External photoevaporation therefore very likely affected the structure and dynamics within our protoplanetary disk.

If external photoevaporation affected the surface density profile of our protoplanetary disk in the manner predicted by Desch (2007), the outer parts of the solar nebula would be described as a steady-state decretion disk. Mass would flow from a reservoir in the inner disk, outward with a constant mass decretion rate $\dot{M}$ through the outer disk, to an outer edge where it is lost by photoevaporation. In the 5-30 AU region of the disk, a slope $p \approx 2.2$ is predicted. More recently, Mitchell & Stewart

(2010) performed numerical simulations of disks subjected to external photoevaporation to test whether the steady-state decretion disk solution of Desch (2007) applied. From their simulations, they report quasi-steady state disks with less steep profiles having slopes $p \sim 1.6$ - 1.8. This is not as steep as the profile inferred by Desch (2007), but the discrepancy may have to do with the way viscosity is handled. The viscosity of Mitchell & Stewart (2010) was parameterized in the usual way, with the fiducial α scaling relation from Shakura & Sunyaev (1973) in which $\nu = \alpha\, c_s H$, where c_s is the speed of sound, which denotes the maximum velocity scale of turbulence; $H = c_s/\Omega$ is the scale height of the disk, which denotes the maximum size scale of turbulence assumed; and α is the dimensionless scaling factor for turbulent viscosity that represents the efficiency for angular momentum transport. It is important to note that Mitchell & Stewart (2010) assumed a uniform value for α throughout the radial extent of the disk. We assert that this is an ad hoc assumption unless an actual mechanism for angular momentum transport is identified. Likely mechanisms do not predict uniform α. For example, one mechanism that has often been proposed for angular momentum transport - at least early in the evolution of the disk, while it is still massive - is the gravitational instability (GI) in which α depends on the Toomre parameter $Q_T = c_s\,\Omega/\pi G\,\Sigma$ (here Ω is the orbital frequency) as given by the following prescription from Lin & Pringle (1990) :

$$\alpha = 0.01 \left(\left[\frac{Q_{\rm crit}}{Q_T} \right]^2 - 1 \right), \tag{2.3}$$

where $Q_{\rm crit}$ is the minimum value of Q_T at which the disk becomes gravitationally unstable. Since Q_T is clearly dependent on r, α can be expected to be variable through the radius of the disk, if disk viscosity originated due to GI.

The most widely accepted mechanism attributed to the transport of mass and angular momentum across the disk is the magnetorotational instability, or MRI (Balbus

& Hawley 1998; Gammie 1996), whose operation is dominant in regions of the disk where gas with a sufficiently high ionization fraction is coupled to the magnetic field. A disk with a varying density profile across radius and height, ionized mainly by stellar X rays and cosmic radiation, would have an ionization fraction varying by several orders of magnitude. Such variation in ionization levels is also apparently observed in the TW Hya disk by Cleeves et al. (2015), which is possibly due to the spatially varying ability of stellar wind to repel cosmic rays (Cleeves et al. 2014). A varying ion fraction would also result in a variable α across the disk. Dense gas and dust-rich protoplanetary disks are only partially ionized systems, and hence it is important to consider the effects of non-ideal magnetohydrodynamics (MHD) in the operation of the MRI. Ambipolar diffusion takes particular importance as it operates in the highly ionized and low density regime which primarily constitutes the disk atmosphere and large portions of the outer disk (Bai & Stone 2011). We begin our simulations with disk mass $M_d = 0.1$ $M_\odot$ - the expected upper threshold for a gravitationally stable disk, and incorporate the formulation of Bai & Stone (2011) for deriving MRI-viscosity from ionization state by including the non-ideal MHD effects of ambipolar diffusion, to estimate the value of α across the radial and vertical extent of the disk. A similar effort of including MRI derived viscosity with non-ideal MHD effects in PPD simulations was also undertaken by Landry et al. (2013). They perform simulations where they include ambipolar diffusion using the prescription of Bai & Stone (2011) as well as ohmic resistivity, but do not discuss photoevaporation that can also significantly affect disk behavior. In this work, we argue and show that considering a variable value for α in disk models can significantly affect the steepness of the disk profile. We also simultaneously incorporate external photoevaporation (important for the Sun's disk) in our models and show how disk structure and evolution are dramatically altered by considering both non-uniform α and external photoevaporation.

Finally, gas and dust grain chemistry play a vital role in determining the ionization fraction in each region of the disk. Previous works have employed: i) simple dust models that include only a single ion-based chemistry (molecular ion- or metal ion-based) adapting work from Oppenheimer & Dalgarno (1974) (e.g. Fromang et al. 2002); ii) more complex chemical networks that account for multiple interacting species (e.g. Sano et al. 2000; Ilgner & Nelson 2006); and iii) reduced chemical networks that attempt to simplify the complex reaction networks into simpler networks for easier computation (e.g. Semenov et al. 2004). Ilgner & Nelson (2006) present a comprehensive comparison between different models that are commonly used for dust chemistry in disks. We use a simple dust model based on the first approach: a single ion-based approach. We also vary different sources of ionization. We test different models that focus on chemistry of either metal atoms or molecular ions, and show how they each affect the structure of the disk.

The following sections are organized as follows. Section 2 will describe the details of our numerical models, how we include the effects of non-uniform α and photoevaporation, as well as our dust chemistry model. Section 3 will discuss the main results of the time evolution of $\Sigma(r,t)$ from our simulations with reference to a canonical simulation with typical values of each variable parameter in our models. We will also describe the effect of variation of each parameter. Finally, in Section 4, we discuss in detail what implications our results have towards planet formation.

2.2 Methods

In this section, we will discuss the numerical model for disk evolution in detail. We will first describe the underlying viscous disk evolution code, then our implementation of ionization equilibrium with dust chemistry throughout the radial and vertical extent of the disk in order to estimate α from MRI-viscosity, and finally the treatment of

Run	G_0	α	g/d	β_g	Ł$_{xr}$	CR Exc	Comment	Figures
1	1	10^{-3}	N/A	N/A	N/A	N/A	Assigned α without PE	Fig. 3
2	1000	10^{-3}	N/A	N/A	N/A	N/A	Assigned α with PE	Figs. 4 - 6
3	1000	10^{-4}	N/A	N/A	N/A	N/A	Effect of assigned uniform α	Fig. 7
(2)	1000	10^{-3}	N/A	N/A	N/A	N/A		
4	1000	10^{-2}	N/A	N/A	N/A	N/A		
5	1	N/A	N/A	10^{-8}	10^{29}	No	MRI α without PE (DUST-FREE)	Figs. 8, 9
6	1000	N/A	N/A	10^{-8}	10^{29}	No	MRI α with PE (DUST-FREE)	Figs. 10 - 13
7	1	N/A	1000	10^{-8}	10^{29}	No	MRI α without PE + DUST	Figs. 14, 15
8	1000	N/A	1000	10^{-8}	10^{29}	No	MRI α with PE + DUST	Figs. 16 - 19
9	300	N/A	1000	10^{-8}	10^{29}	No	(MRI α + DUST + PE) Effect of G_0	Fig. 20
(8)	1000	N/A	1000	10^{-8}	10^{29}	No		
10	3000	N/A	1000	10^{-8}	10^{29}	No		
11	1000	N/A	100	10^{-8}	10^{29}	No	(MRI α + DUST + PE) Effect of (g/d)	Fig. 21
(8)	1000	N/A	1000	10^{-8}	10^{29}	No		
12	1000	N/A	10000	10^{-8}	10^{29}	No		
13	1000	N/A	1000	10^{-6}	10^{29}	No	(MRI α + DUST + PE) Effect of β_g	Fig. 22
(8)	1000	N/A	1000	10^{-8}	10^{29}	No		
14	1000	N/A	1000	$3 \times 10^{-11}/T^{0.5}$	10^{29}	No		
15	1000	N/A	1000	10^{-8}	10^{28}	No	(MRI α + DUST + PE) Effect of $L_{\rm xr}$	Fig. 23
(8)	1000	N/A	1000	10^{-8}	10^{29}	No		
16	1000	N/A	1000	10^{-8}	10^{29}	Yes	(MRI α + DUST + PE) CR Exclusion	Fig. 24
(8)	1000	N/A	1000	10^{-8}	10^{29}	No		

Table 1: Table of Simulations

external photoevaporation due to FUV radiation from a nearby massive star. To understand how the Sun's nebula might have probably evolved, it is important to include the effects of external photoevaporation into a non-uniform α viscosity disk evolution model.

2.2.1 Viscous Disk Evolution

Our '1.5-D' disk evolution code employs the fiducial equations of viscous disk evolution from LBP where the rate of change of surface density $\Sigma(r)$ is related to

$\dot{M}(r)$, the rate of inward mass flow through an annulus of the disk:

$$\frac{\partial \Sigma}{\partial t} = \frac{1}{2\pi r} \frac{\partial \dot{M}}{\partial r}\,, \tag{2.4}$$

where

$$\dot{M} = 6\pi r^{1/2} \frac{\partial}{\partial r} \left(r^{1/2} \Sigma \nu \right). \tag{2.5}$$

Here $\dot{M} > 0$ refers to an inward mass flow toward the star, while $\dot{M} < 0$ refers to an outward flow towards the disk edge. Equation 2.5 can also be written as :

$$\dot{M} = 3\pi \Sigma \nu \left[1 + 2Q \right], \tag{2.6}$$

where $Q = \partial \ln(\Sigma\nu) / \partial \ln r$. The above equations are discretized into a logarithmic grid of 60 radial zones split across 0.1 AU to 100 AU for all of our runs (excepting the uniform α runs where we use a 100 radial zones, instead of 60). These are explicitly integrated in time. Mass fluxes are considered at the boundaries of each annulus, while viscosity $\nu(r)$, surface density $\Sigma(r)$, density ρ, ion abundance N_i and electron abundance N_e are all considered at the midpoint of each annulus.

We implement an initial surface density profile at time $t = 0$ from the LBP self-similar solutions (Hartmann 1998):

$$\Sigma(r) = \frac{M_0}{2\pi R_0\, r} \exp\left(-\frac{r}{R_0} \right), \tag{2.7}$$

where initial disk mass M_0 is assumed to be 0.1 $\mathrm{M}_\odot$, and R_0 denotes initial disk radius, assumed to be 100 AU. We assume the mass of the host star is 1 $\mathrm{M}_\odot$. The ratio of stellar mass to disk mass of 0.1 represents the typical value of a most massive disk that is likely gravitationally stable. We incorporate the temperature profile for a disk undergoing layered accretion from Lesniak & Desch (2011), which is suitable for a passively heated disk or a disk heated by MRI-driven accretion with $\dot{M} < 10^{-7}\,\mathrm{M}_\odot\,\mathrm{yr}^{-1}$:

$$T(r) = 100 \left(\frac{r}{1\,\mathrm{AU}} \right)^{-0.5} \mathrm{K} \tag{2.8}$$

We allow the disk to extend freely out to an outer computational boundary $r_{\rm out}$ by assuming that at $r_{\rm out} \gg r_{\rm disk}$, $\dot{M} = 0$. For the inner boundary, we assume the zero-torque boundary condition, assuming that gas at some point becomes coupled to the slowly rotating star and must orbit at less than Keplerian velocity. This forces $\partial\,\Omega/\partial\,r > 0$ close to the star, $\partial\,\Omega/\partial\,r = 0$ at some boundary, merging with Keplerian rotation with $\partial\,\Omega/\partial\,r < 0$ beyond that boundary. The boundary is fixed to be close to the stellar radius, although magnetospheric truncation of the disk (Bouvier et al. 2007) could move the boundary outward. This may slightly alter the structure of the disk in the innermost few tenths of an AU but will not affect its evolution in the outer disk that is the focus of the present work. Our boundary criterion is derived from the following analytical solution of Equations 2.4 and 2.5:

$$\Sigma(r) = \frac{\dot{M}}{3\pi\nu}\left[1 - \left(\frac{r_0}{r}\right)^{1/2}\right], \tag{2.9}$$

where a uniform $\dot{M}$ and a narrow first zone are assumed. We then solve for Q (from Equation 2.6) for the first zone by integrating the analytical solution (Equation 2.9) with r to obtain the total mass of the first zone. Dividing by the surface area of the first annulus, this Σ_1 is equated to the analytical solution to solve for Q, and thereafter $\dot{M}_1$. We have evolved all simulations for 10 Myr, except in the cases where photoevaporation dissipates most of the disk such that the radius of the disk is truncated to 5 AU or less within the simulation timescales. In these cases, the simulations are terminated when the size of the disk shrinks to $\leq$ 5 AU in radius.

We incorporate the standard α parameterization for turbulent viscosity by Shakura & Sunyaev (1973), where $\nu = \alpha\, c_s H$ and α is the turbulent viscosity coefficient, c_s is the sound speed and H is the disk scale height. From measurements of disk masses and accretion rates in disks in Taurus and Chameleon I star forming regions ($\sim$ 1 Myr old), Hartmann et al. (1998) inferred a globally averaged $\alpha \sim 0.01$, the value

most disk models use. More recent studies (Andrews et al. 2009, 2010) find a range of $\alpha \approx 0.0005$ - 0.08 in resolved disks in the $\sim$ 1 Myr old Ophiuchus star-forming regions. We emphasize that any realistic physical mechanism of angular momentum transport is not likely to yield a constant value of α throughout the radius of the disk and its lifetime. In the following subsection, we will describe how we incorporate a non-uniform value of α derived from MRI viscosity.

2.2.2 Viscosity from Magnetorotational Instability

Ionization Equilibrium with Dust

We divide each radial zone further into 25 vertical zones across the thickness of the disk, from the midplane to its surface, to estimate the ionization fraction across radius r and height z of the disk. Vertical zones are chosen with the help of weights and abscissa of the Gaussian-Legendre quadrature. We assume that the disk is isothermal with height, and hence incorporate a simple gaussian profile for density ρ across the height of the disk centered on the mid-plane:

$$\rho(r, z) = \frac{1}{2}\,\rho_o(r)\exp\left(-\frac{z^2}{2H^2}\right). \tag{2.10}$$

We thereafter assume that the disk is ionized by two sources of non-thermal radiation: X rays from the central host star itself, and cosmic radiation. Cosmic radiation, less intense than X-ray radiation, impinges the disk equally throughout r. As a consequence it affects a large fraction of the optically thin outer disk as well as the disk surface layers closer to the star. For the cosmic ray ionization rate across r and z, we incorporate the widely used expression for Galactic cosmic rays given by Umebayashi & Nakano (1981):

$$\zeta_{\rm cr}(z) = 1 \times 10^{-17}\exp\left(\frac{-\sigma_\perp}{100\,{\rm g\,cm^{-2}}}\right)\ \ {\rm s^{-1}} \tag{2.11}$$

Stellar X rays, on the other hand, will strongly illuminate and penetrate the innermost disk and the optically thin surface layers. The disk midplane regions are likely to be shadowed by the dense inner regions, but the outer flared disk will be illuminated by central star's X rays, although not as intensely as in the inner disk; the X-ray ionization rate reduces with r. We use the X-ray ionization rates of Glassgold et al. (1997), who consider an X-ray emitting region of size $\sim 10\,R_\odot$ centered on the star :

$$\zeta_{\rm xr}(z) = \zeta_0\, Z_0 \quad {\rm s}^{-1}\ , \tag{2.12}$$

where ζ_0 is given by

$$\zeta_0(z) = 6.45\times10^{10}\,\tilde{\sigma}\,\left(\frac{kT_{\rm xr}}{1\,{\rm keV}}\right)^{-n}\left(\frac{L_{\rm xr}}{1\times10^{29}\,{\rm ergs\,s^{-1}}}\right)\left(\frac{r_{\rm mid}}{1\,{\rm AU}}\right)^{-1}\cos\theta \quad {\rm s}^{-1}, \tag{2.13}$$

$\tilde{\sigma} = 2.27\times10^{-22}\,{\rm cm}^2$ is the photoionization cross section at 1 keV, $T_{\rm xr}$ and $L_{\rm xr}$ are the X-ray temperature and X-ray luminosity, respectively. Here, $kT_{\rm xr}$ is assumed to be 5 keV and $n = 2.485$. $Z_0(z)$ is given by

$$Z_0(z) = A\,[\tau(z)]^{-a}\exp\left[-B\tau(z)^b\right], \tag{2.14}$$

where the respective constants are $A = 0.800$, $B = 1.821$, $a = 0.57$ and $b = 0.287$ (Glassgold et al. 1997). For the above equations, as shown in Fig. 1 (in Glassgold et al. 1997) we define optical depth $\tau(z) = 1$ where $\tau(z) < 1$. For higher optical depths, we assume the following expression from Glassgold et al. (1997):

$$\tau(z) = 42.76\,\sigma_\perp(z)\,\tilde{\sigma}\,\left(\frac{kT_{\rm xr}}{1\,{\rm keV}}\right)^{-n}\frac{1}{\cos\theta}, \tag{2.15}$$

where, $\sigma_\perp(z)$ is the surface density normal to the disk mid-plane at about a height z ($\Sigma = 2\,\sigma_\perp(z)/\sigma_{\rm total}$; similar to column mass density as a function of z). In the above equations, we have included a factor $\cos\theta$ to account for the disk flaring angle at each r, as the fraction of the disk that would actually intercept the stellar X rays at each

r is dependent on the flare angle, and is implemented here as follows. The disk is divided into two regions: the first is an innermost disk $\leq$ 2AU, where radius of the X ray-emitting region $R_{\rm xr} \approx 10\,R_{\odot}$ is comparable to the disk thickness. In this region, the disk flare angle $\cos\theta = R_{\rm xr}/r$. The second region is the outer disk beyond $\sim$ 2AU, where the flare angle is given by $\cos\theta = 4\,(dH/dr - H/r) \equiv 4\,r\,d\,(H/r)/dr$ (Lesniak & Desch 2011). We make the following assumption that scale height H varies with r as $H \approx H_0\,(r/1\,{\rm AU})^{1.25}$ with $H_0 \approx 0.02$ at 1 AU, to derive the following equations for $\cos\theta$, whose solutions match at $r \approx 2$ AU:

$$\cos\theta = 0.047\left(\frac{r}{1\,{\rm AU}}\right)^{-1}, r \leq 2{\rm AU} \tag{2.16}$$

$$\cos\theta = 0.02\left(\frac{r}{1\,{\rm AU}}\right)^{0.25}, r \geq 2{\rm AU}. \tag{2.17}$$

We implement a steady state ionization-recombination equilibrium with gas-grain chemistry by considering ionization by X rays and cosmic rays, and recombination of ions and electrons in the gas phase and on dust grains, with the following equations:

$$\frac{dn_e}{dt} = \zeta n_{H_2} - n_e n_{\rm gr} \pi a_{\rm gr}^2 C_e S_e \tilde{J}_e - \beta_g n_e n_i \tag{2.18}$$

$$\frac{dn_i}{dt} = \zeta n_{H_2} - n_i n_{\rm gr} \pi a_{\rm gr}^2 C_i S_i \tilde{J}_i - \beta_g n_e n_i \tag{2.19}$$

Ionization and recombination are both assumed to quickly establish equilibrium, and hence rates of change in electron and ion density (dn_e/dt and dn_i/dt) on the left hand side of the Equations 2.18 and 2.19 are assumed to be 0. Here, ζ is the sum of the ionization rates due to all ionizing sources, $n_{\rm gr}$ is the number density of dust grains and $a_{\rm gr}$ is the size of the dust grain assumed to be 1 μm. C_k and S_k are the thermal velocity and sticking coefficient of species k respectively. $\tilde{J}_k$ is the collision cross section of k, taken from Draine & Sutin (1987) who consider the effects of grain charging on the probability of collisions of ions and electrons on dust grains. β_g is

the gas phase recombination coefficient. In each zone, overall charge neutrality is assumed to be quickly attained.

When dust is absent, the above equation reduces to a simple ion-balance equation with only gas-phase chemistry:

$$n_i(z) = \left[\frac{\left(\zeta_{\rm xr} + \zeta_{\rm cr} + \zeta_{\rm rad}\right) n_{H_2}}{\beta_g}\right]^{1/2} {\rm cm}^{-3}, \tag{2.20}$$

where we have also included a small $\zeta_{\rm rad} = 7 \times 10^{-19}\,{\rm s}^{-1}$ to account for ionization due to radioactive decay of ^{26}Al, consistent with Umebayashi & Nakano (2009) . We assume that the abundances of short-lived radionuclides like ^{26}Al are uniform across the disk, which may not be true, depending on the spatial distribution of the sources of radionuclides, such as one or more nearby supernovae or AGB stars, and their time of injection, or spallation reactions within the protoplanetary disk (Davis & McKeegan 2014). Ionization by radionuclide decay is in any case a minor contribution.

We calculate the number density of hydrogen molecules as, $n_{H_2}(z) = \rho(z)/1.4\,m_{H_2}$. In each zone, our dust chemistry routine solves Equations 2.18 and 2.19 iteratively for the equilibrium abundances of ions and electrons, and calculates the charge on dust grains, at each r and z in the disk. The grain abundance $n_{\rm gr}$ at each r and z is decided by the gas-to-dust mass (g/d) ratio assumed. This computationally intensive step of directly calculating the equilibrium abundances within the disk evolution code itself motivated our choice for picking a lower number of radial (60) and 25 height zones.

We use a range of values for the gas-to-dust mass ratio (g/d): [100,1000,10000] in order to explore the evolution of the disk in different stages of grain growth, centering on a value of 1000. As the extent of recombination depends primarily on the grain surface available, changing (g/d) while keeping grain size $a_{\rm gr}$ constant is equivalent to changing $a_{\rm gr}$ with a constant (g/d), as both $a_{\rm gr}$ and (g/d) affect the total available

dust grain surface area. We also assume a range of values for β_g to account for disk chemistry that focuses on two different ionic species : i) molecular ion chemistry, where the fast recombination reaction of HCO^+ with electrons is considered ($\beta_g = 1 \times 10^{-6}\,\mathrm{cm^3\,s^{-1}}$); ii) metal ion chemistry, where it is assumed that all molecular ions have transferred their charge to metal ions in comparatively fast charge-transfer reactions, following which these metal ions recombine very slowly with electrons ($\beta_g = 3 \times 10^{-11}/\,T^{1/2})\,\mathrm{cm^3\,s^{-1}}$; here the slow metal-electron recombination reaction dominates the rate; and iii) a simple reduced chemistry network with both species (molecular and atomic ions) that aims to replace both populations with a single species having an intermediate effective $\beta_{g,\mathrm{eff}}$ coefficient that will serve to generate electron densities similar to those attained when both species are present. For this paper, we assume this intermediate effective β_g is $10^{-8}\,\mathrm{cm^3\,s^{-1}}$, taken as the approximate mean between $10^{-6}\,\mathrm{cm^3\,s^{-1}}$ and $10^{-11}\,\mathrm{cm^3\,s^{-1}}$ for molecular-ion and metal-ion dominated chemistry, respectively.

We also explore the effects of different ionization rates on disk structure, as well as the effect of exclusion of cosmic rays due to stellar winds (Cleeves et al. 2014, 2015) by turning off cosmic rays altogether.

α derived from MRI viscosity

To calculate $\alpha(r)$, we first calculate the ion density $\rho_i = n_i(z)\,m_i$, in each zone of the disk, where $m_i = 23\,m_H$. Thereafter, we incorporate the numerical results from Bai & Stone (2011) who consider the effect of non-ideal magnetohydrodynamical (MHD) phenomena in the evolution of magnetorotational instabilities in a protoplanetary disk. Non-ideal MHD effects are especially important in protoplanetary disks which are only partially ionized by cosmic ray and stellar X rays. In 3D shearing box simulations, Bai & Stone (2011) incorporated the effect of ambipolar diffusion via the

parameter Am, that represents the collision frequency of ions and neutral particles in one orbital period:

$$Am = \frac{\gamma \rho_i}{\Omega}. \tag{2.21}$$

Here, $\gamma = 3.5 \times 10^{13}$ cm^3 s^{-1} g^{-1} is the drag coefficient for ion-neutral collisions (Blaes & Balbus 1994; Draine, Roberge & Dalgano 1983) From their numerical simulations, Bai & Stone (2011) find that when turbulence is in saturation in the disk, a strong correlation is found between the turbulence stress factor α (from Shakura & Sunyaev 1973) and the ratio of the gas to magnetic pressure β:

$$\alpha = \frac{1}{2\,\beta_{\rm min}}\,, \tag{2.22}$$

where $\beta_{\rm min}$ is the minimum bound of β below which the magnetic field is too strong to be destabilized by the MRI. From the results of all their simulations, they find a fitting function correlating $\beta_{\rm min}$ and Am:

$$\beta_{\rm min}(Am) = \left[\left(\frac{50}{Am^{1.2}}\right)^2 + \left(\frac{8}{Am^{0.3}} + 1\right)^2\right]^{1/2} \tag{2.23}$$

Using the above Equations 2.21 - 2.23, we calculate a local α at all locations in the disk. Then we compute a vertically integrated and mass-weighted value $\langle \alpha(r) \rangle$ across the height of the disk, that is a function of r. We impose a floor of 1×10^{-5} on α in the inner disk, without which the interior of the disk evolves so slowly that it affects the numerical stability of the code.

2.2.3 Photoevaporation

We implement external photoevaporation due to FUV radiation from nearby massive stars, using the equations for photoevaporative mass loss rates for sub-critical disks (i.e., when disk radius $r_d \ll r_g$, the gravitational radius) from Adams et al.

(2004) as follows:

$$\dot{M}_{\rm pe} = C_0\, N_C\, \langle\mu\rangle\, c_s\, r_g \left(\frac{r_g}{r_d}\right) \exp\left(-\frac{r_g}{2r_d}\right), \tag{2.24}$$

where we assume $C_0 = 4$, r_d is the disk edge, $N_C = 1.25 \times 10^{21}{\rm cm}^{-2}$ is the critical column density for the attenuation of FUV, and r_g is the radius at which gas molecules are sufficiently thermally excited to be able to escape the gravitational potential of the star, given as :

$$r_g = \frac{GM_*\langle\mu\rangle}{kT_{\rm FUV}} \quad {\rm AU}. \tag{2.25}$$

Here $c_s = \left(k\,T_{\rm FUV}\,/\langle\mu\rangle\right)^{1/2}$ and $\mu = 1.25\,m_H$, where m_H is the mass of a hydrogen atom.

The FUV flux is usually expressed as G_0, normalized to the Habing field, where 1 Habing field $= 1.6 \times 10^{-3}\,{\rm ergs\,cm^{-2}\,s^{-1}}$. The average flux of the interstellar FUV radiation field is equivalent to G_0= 1.7 Habings. It is not simple to estimate the temperature of the photoevaporating disk atmosphere due to FUV radiation. From the temperature vs. optical depth profiles in Figure 2 of Adams et al. (2004), temperature is seen to be extremely sensitive to G_0. We estimate a $T_{\rm FUV}$ dependence with G_0 by assuming an average number density $\sim 10^{-4}$, as follows:

$$T_{\rm FUV} = 250 \left(\frac{G_0}{3000}\right)^{0.5} {\rm K}. \tag{2.26}$$

In the treatment of photoevaporation adopted in this work, we only include the $\dot{M}_{\rm pe}$ from the disk edge and do not include any $\dot{M}_{\rm pe}$ from the top and bottom surfaces of the disk such as that given in Appendix A in Adams et al. (2004). Using Equations A7 and A8, we find that >75% of mass is lost from the outer edge. However, we also find that Equation A8 makes inconsistent assumptions about the geometry of the flow that likely overestimates the mass lost from the surface of the disk. We have used a range of G_0 in this study of [300, 1000, 3000]. This is mainly motivated from

the results of Adams et al. (2006, Figure 9) where they find that the median flux experienced by a cluster star is $\sim$ 1000. 300 and 3000 represent particular values below and above this median used by Adams et al. (2004).

2.3 Results

In this section, we describe the results obtained from our numerical simulations of disk evolution where we explore the effect of external photoevaporation (due to FUV radiation from nearby massive star), non-uniform α due to the MRI and dust chemistry.

Our numerical simulations can be best categorized as two sets of disk evolution simulations: one performed with the usual uniform α standardization, and one where we include an MRI derived viscosity treatment from which we obtain a non-uniform variable α as a function of time and disk radius r. We have also performed several sets of simulations to assess the effects of important parameters in our simulations that are likely to have significant impact on disk structure or are known to have a range of possible values via observations. For the uniform α cases, we have explored the effects of different values of α and different radiation environments (via the parameter G_0). For variable α cases, we have tested the effects of different values of G_0, gas-to-dust (g/d) ratio, gas phase recombination coefficient β (to account for atomic or molecular-ion disk chemistry), change in ionization rates due to different stellar X-ray luminosities $L_{\rm xr}$ and cosmic radiation. We vary many of these parameters by an order of magnitude above and below a canonical value. Table 1 summarizes all the simulations carried out in this investigation. We quantify the effects of variation of these parameters by looking at how they change the following disk properties related to its structure: i) mass M_d of the disk; ii) slope $\langle p \rangle$ of the surface density $\Sigma(r,t)$ profile; iii) disk size or outer radius r_d ; and iv) transition radius r_T (the radius at

which the net mass flow in the disk changes its direction from inward to outward (described in detail below).

2.3.1 Uniform α

The following section describes the simulations performed with uniform α, i.e., runs 1, 2, 3 and 4 [See Table 1].

Canonical Case for Uniform α

We present runs 1 and 2 as the canonical case for disk evolution with uniform α. Run 1 is a simple uniform α-disk that viscously expands with time. In run 2, this disk is subjected to external photoevaporation with an FUV flux of $G_0 = 1000$ (assuming the median value from Fig. 11 in Adams et al. 2006). In both runs we adopt $\alpha = 10^{-3}$ as a typical value of α considered averaged throughout r. This choice of α is consistent with the range of α inferred from observations of resolved disks from Andrews et al. (2009, 2010).

Fig. 3 and Fig. 4 show the typical surface density profile $\Sigma(r, t)$ for a uniform α-disk undergoing viscous evolution without photoevaporation ($G_0 = 1$), and with photoevaporation ($G_0 = 1000$), respectively. While a non-photoevaporated disk viscously expands with time (Fig. 3) and loses mass mainly via accretion onto the star, a photoevaporated disk loses mass to both accretion onto the central star, as well as photoevaporation via the outer edge of the disk over 10 Myr, as seen in Fig. 3 and Fig. 5. For the photoevaporated disk, the rates for mass loss due to accretion and photoevaporation are both similar, i.e., $\dot{M}_{\rm acc} \approx \dot{M}_{\rm pe} \sim 10^{-8}\,{\rm M}_\odot\,{\rm yr}^{-1}$. The dip in each curve in Fig. 5 represents the transition radius, r_T, i.e., where the directionality of the net mass flow changes from inward towards the central star to outward.

In order to monitor the average slope of the Σ profile of the disk, for each simula-

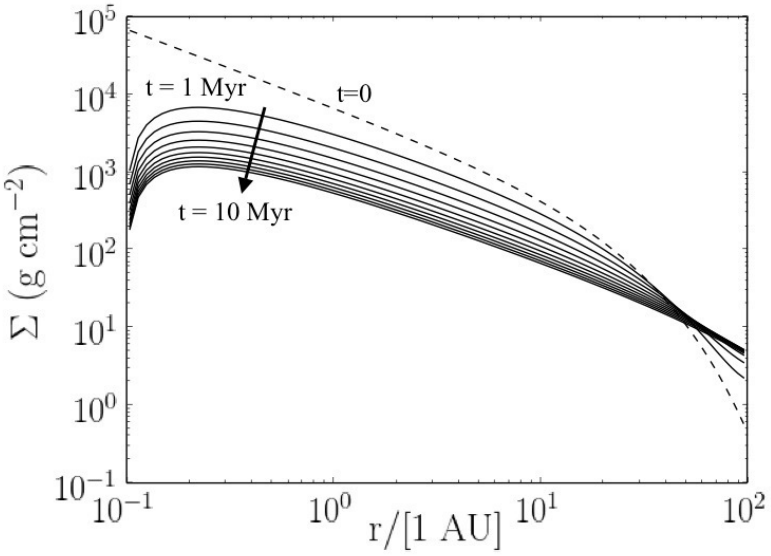

Figure 3: Surface density profiles $\Sigma(r,t)$ of our canonical uniform α case without photoevaporation. α is assumed to be 0.001, and $G_0 = 1$ in this run. Each curve shows the Σ profile at times: 0 Myr (dashed), 1 Myr, 2 Myr, .. , 10 Myr. Note that the non-photoevaporated disk viscously expands with time.

tion, we also plot $\langle p \rangle = d\,(\log \Sigma)/d(\log r)$ with time, in Fig. 6, where $\langle p \rangle$ is spatially averaged over the giant planet formation region, i.e., 5-30 AU (discussed in Desch 2007). Since we use $\langle p \rangle$ across the region 5-30 AU, curves for $\langle p \rangle$ with time for all simulations are plotted till the disk is truncated to 30 AU. A feature that stands out in this set of simulations is that the profile of the disk and its slope remains uniformly preserved throughout its 10 Myr of evolution, as is seen in Figs. 4 and 6. The slope $\langle p \rangle$ is almost constant (~ 1.6) throughout the simulation duration, although a slight increase is noted in the last few Myr of simulation. The profile of the non-photoevaporated disk, in contrast, is seen to flatten towards ~ 1 with time, consistent with theoretical predictions. Fig. 6 also shows the change in disk mass with time for both the non-photoevaporated and photoevaporated cases. As expected, the mass of a photoevaporated disk is considerably lower after 10 Myr, as compared to a non-photoevaporated disk. Fig. 6 additionally shows how the outer radius r_d and

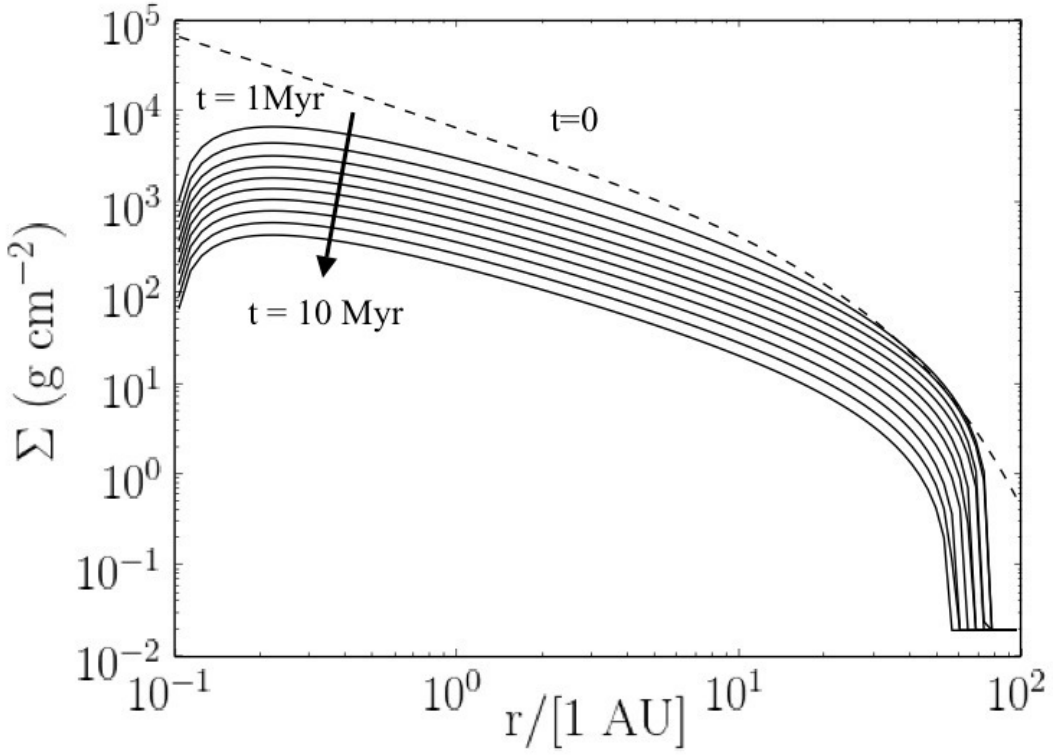

Figure 4: Surface density profiles $\Sigma(r,t)$ of our canonical uniform α case with photoevaporation. α is assumed to be 0.001, and $G_0 = 1000$. Each curve shows the Σ profile at times: 0 Myr (dashed), 1 Myr, 2 Myr, .. , 10 Myr. Note that the disk is truncated to 55 AU after 10 Myr and the shape of the Σ profile remains preserved.

transition radius r_T varies as evolution proceeds. A non-photoevaporated disk viscously expands with time (as seen in Fig. 3; not shown in Fig. 6 as our simulations are only performed to a radius of 100 AU). A photoevaporated disk on the other hand, continually shrinks in size with time due to continuous removal of mass from the outer disk edge by photoevaporation. r_T varies distinctly in both cases, by moving outward with time in a non-photoevaporated viscously spreading disk (see Equation 23 in Hartmann et al. 1998) and moving inward with time in a photoevaporated disk. This leads us to a picture where more and more mass moves outwards in a

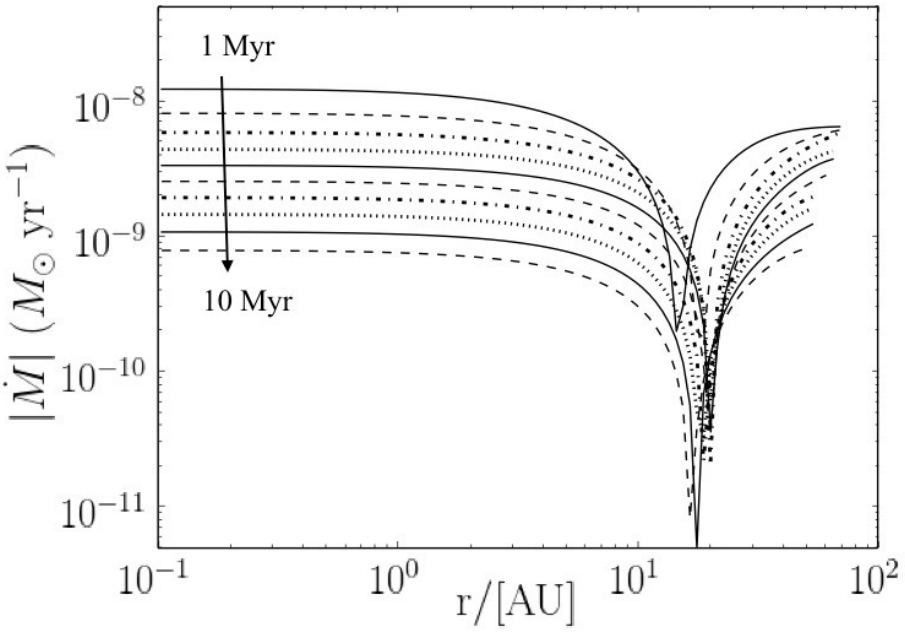

Figure 5: $\dot{\mathrm{M}}$(r) profiles of the disk for each successive Myr: 1 Myr, 2 Myr .. 10 Myr (solid, dashed, dot-dashed, dotted...) for the canonical uniform α case with photoevaporation ($G_0 = 1000$). Mass moves radially inward till radius = r_T (transition radius) where the mass flow changes direction. Beyond r_T, mass flows radially outward due to photoevaporation. The dip in each curve denotes r_T, which is independently plotted in Fig 4.

photoevaporated disk, as the disk itself shrinks in size.

Parameter Study: Effect of α

Runs 2, 3 and 4 explore the effect of variation of the parameter α in photoevaporated ($G_0 = 1000$) uniform α disks. Fig. 7 shows how different disk properties vary with time with different values of globally-averaged α in the disk. As expected, higher the value of α, more rapid is the disk evolution so much so that disks with $\alpha \sim 10^{-2}$ dissipate within ~ 4 Myr. Such a disk loses more than 95% of its mass within 2 Myr. This rapid evolution and movement of most of its mass is also indicated by the rapid change in the slope $\langle p \rangle$ of the 5-30 AU region. On the contrary, disks with $\alpha = 10^{-4}$

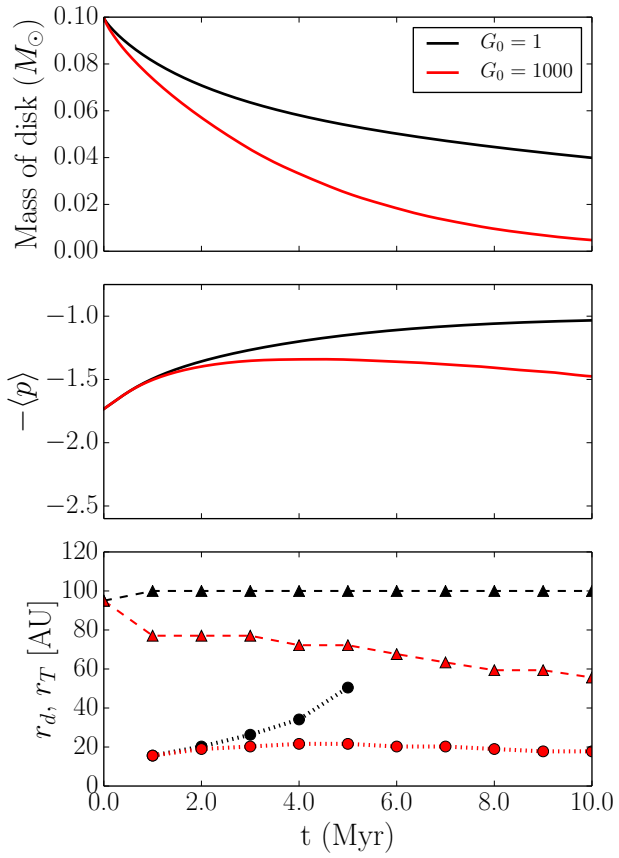

Figure 6: Change in the disk properties (disk mass M_d, slope $\langle p \rangle$ of $\Sigma(r)$, disk outer edge r_d and transition radius r_T) with time for the canonical uniform α case with photoevaporation ($G_0 = 1000$; red). Black curves show the non-photoevaporated case ($G_0 = 1$ with other parameters unchanged) for comparison. Here, $\langle p \rangle$ denotes spatial average of slope p across 5-30 AU, and r_d and r_T are shown at each successive Myr of evolution. Non-photoevaporated case ($G_0 = 1$) is denoted by black triangles (for r_d) and black circles (for r_T), and photoevaporated case ($G_0 = 1000$) is denoted by red triangles (r_d) and circles (r_T). Note that r_T moves outward with time in a non-photoevaporated disk, but moves inward with time in a photoevaporated disk after first few Myr. (For the non-photoevaporated case, r_T moves beyond 100 AU after 5 Myr).

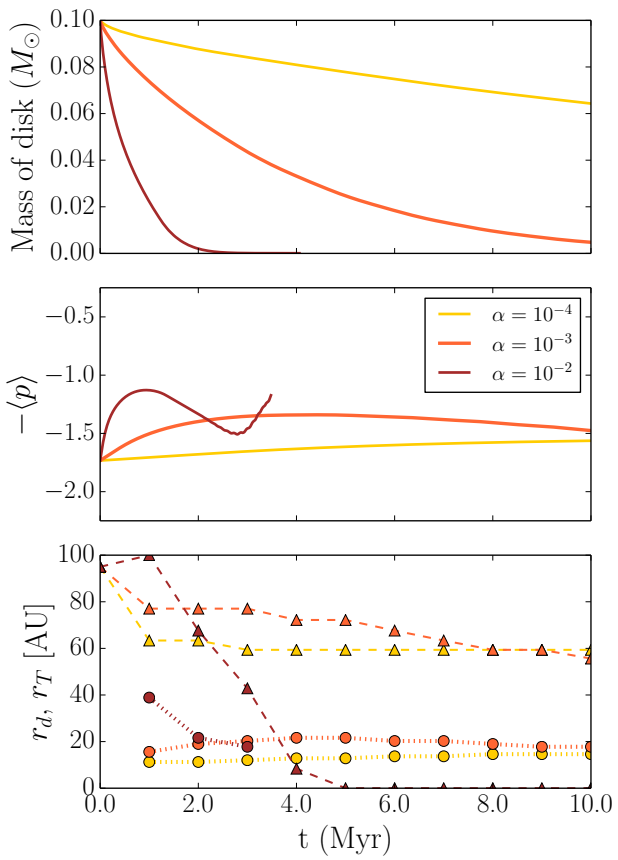

Figure 7: Effect of variation of α on disk properties (disk mass M_d, slope $\langle p \rangle$ of $\Sigma(r)$, disk outer edge r_d and transition radius r_T) with time for the canonical uniform α case with photoevaporation for a range of α values [0.01, 0.001, 0.0001]. Disk with high viscosity (α=0.01) rapidly evolves and shrinks to $\sim$ 10 AU in 4 Myr. $\langle p \rangle$ denotes average of p over 5-30 AU. Triangles denote r_d points and circles denotes r_T points at each Myr. (For $\alpha = 0.01$ case, the disk is too small to retain r_T after 3 Myr).

evolve so slowly that they lose $< 40\%$ of their mass in 10 Myr. $\langle p \rangle$, r_T and r_d in these disks remain more or less constant. Disk simulations with $\alpha = 10^{-3}$ show an intermediate behavior between the two extremes, by retaining $\sim 10\%$ of its mass after 10 Myr with a slowly increasing slope $\langle p \rangle \sim 1.5$, shrinking to a final size of ~ 60 AU after 10 Myr. r_T shows a dual behavior as it initially moves outward over the first 5 Myr, and thereafter moves inwards with time.

Nevertheless, a uniform value for α is not realistic, and we hereafter present simulations where we look at the effect of a radially and temporally varying α on disk

structure.

2.3.2 Non-uniform α

The following section describes in detail simulations performed with computed α, i.e., runs 5-16 [Table 1].

Canonical Case for Non-uniform α: A dust-free disk

Runs 5 and 6 represent the dust-free simulations for varying α shown in Figs. 8-13 taking $L_{\rm xr} = 1 \times 10^{29}\,{\rm ergs\,s^{-1}}$, $\beta_g = 10^{-6}\,{\rm cm^3\,s^{-1}}$, with $G_0 = 1$ for the non-photoevaporated case, and $G_0 = 1000$ for the photoevaporated case. The photoevaporated disk was evolved for ~ 7.5 Myr, after which the simulation was terminated when r_d approached $< 5\,{\rm AU}$.

Figs. 8 and 10 shows the variation of a vertically-averaged mass-weighted $\langle\alpha\rangle$ derived from the MRI (as described in Section 2) with r at 3 different times in disk evolution for $G_0 = 1$ (Fig. 8) and $G_0 = 1000$ (Fig. 10). Initially at $t = 0$, $\langle\alpha\rangle$ varies considerably across the disk, from $\sim$ few $\times\ 10^{-3}$ in the inner disk, to $\sim 10^{-2}$ in the outer disk, in both the non-photoevaporated and photoevaporated cases. This is due to the difference in the ionization fraction between the poorly-ionized dense self-shadowing inner disk and the highly ionized tenuous outer disk. At $t_{mid} = 4 - 5$ Myr, in both cases, the inner disk also attains a higher value of α as much of the inner disk mass is cleared out due to accretion. Thereafter, in the last few Myr, α begins to settles to a constant value of 10^{-2} throughout the disk. High values of α in the outer disk result in increased turbulent mixing and therefore rapid mass movement in the outer disk. Fig. 9 shows $\Sigma(r, t)$ for a non-photoevaporated disk, in which the disk shows comparatively quick dissipation even without photoevaporation. With photoevaporation (Fig. 11) however, very rapid dissipation of the disk truncates the

disk to < 5 AU within 7.5 Myr. This occurs because the high value of α in the outer disk makes it easier for external photoevaporation to remove more mass from the outer edge causing quick disk dispersal. Fig. 12 shows $\dot{M}$ profiles for the photoevaporated disk. The inner disk with lower values of α allows little movement of mass, and hence less mass flow results in the inner regions. $\Sigma(r,t)$ from Fig. 11 and $\langle p \rangle$ vs. time plot from Fig. 13 show that the 5-30 AU slope of the disk profile is maintained at $\langle p \rangle$ ~ 1.75 for upto 1.5 Myr, after which it steepens sharply to $\langle \mathrm{p} \rangle \sim 3.0$ due to increase in mass loss by photoevaporation. Thereafter, as the disk shrinks in, the inward mass loss due to accretion becomes greater than the photoevaporative mass loss rate, ultimately flattening the slope profile towards the end of the simulation. However, the overall disk structure (Fig. 11) is seen to be mostly maintained through the rapid disk dissipation. Fig. 13 also shows the M_d vs. time and r_d and r_T vs. time. r_T is seen to move inwards during the first 5 Myr.

Canonical Case for Non-uniform α: Gas+Dust disk

Runs 7 and 8 (Figs. 14-19) show disk evolution simulations for varying α where dust has been included in the disk. We adopt a uniform grain size of $a_{gr} = 1\mu$m and a gas-to-dust (g/d) ratio of 1000. Our choice for a larger value of (g/d) than standard is motivated by the fact that it was comparatively difficult to obtain any significant disk evolution with the standard g/d of 100. While this choice of (g/d) could be assumed to be a slightly advanced stage in grain growth, we note that the standard g/d=100 usually assumed in protoplanetary disks is itself an assumption. We also assume a $G_0 = 1000$ as the typical FUV flux incident on the disk, similar to the previous sets of simulations. A stellar X-ray luminosity of 10^{29} ergs s^{-1} and an effective β_g of $10^{-8}\,\mathrm{cm}^3\,\mathrm{s}^{-1}$ are assumed, as discussed in Section 2.

It was required to impose a floor value on α to assist disk evolution in the inner

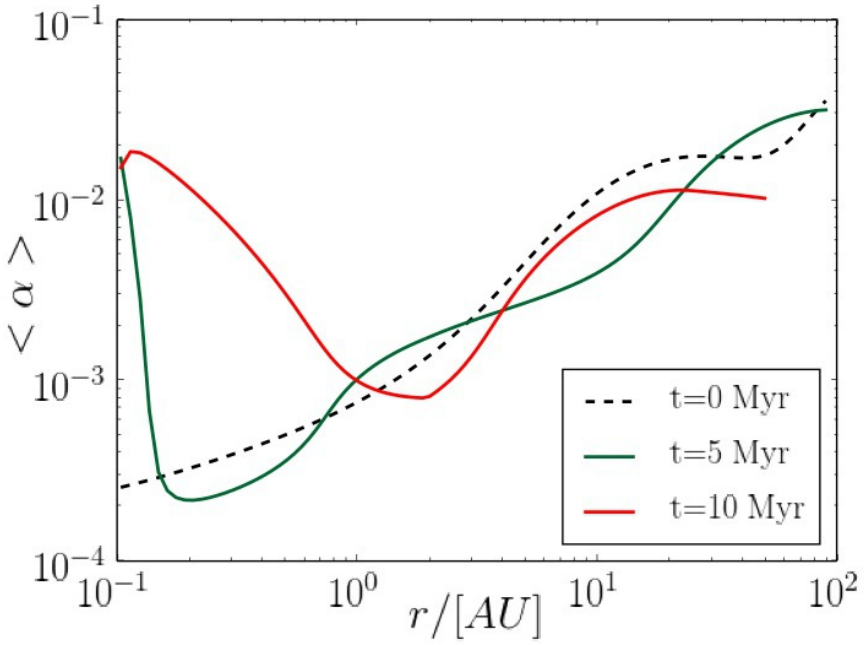

Figure 8: Vertically integrated and mass weighted $\langle\alpha\rangle$ as a function of r, at various times for the canonical computed α dust-free case, without photoevaporation ($G_0 = 1$). The curves are truncated at the disk radius r_d at each plotted time.

disk, as the addition of dust made the evolution of the disk interior very slow (Figs. 14 and 16). The inner disk due to its high density is weakly ionized. Stellar X-rays and cosmic radiation are able to penetrate the cloud only where it is optically thin. The presence of dust makes this already scarce availability of charges worse by absorbing them and hence maintaining a very small ionization fraction of ions and electrons in the disk interior. Rates of infall onto the star plummet to $\sim$ few $\times$ 10^{-10} $M_{\odot}{}^{-1}$ (Fig. 18). However, the outer disk being optically thin is sufficiently ionized by both cosmic radiation and oblique stellar X rays which drives rapid mass flow. Figs. 17 and 19 show this more clearly, as the presence of dust chokes inner disk evolution such that a significant fraction of mass in the disk is only redistributed towards the inner disk. This causes α to rise dramatically in a sharp transition from 10^{-4} to 0.1 in the 3 AU - 20 AU region; which moves inward with time (Fig. 16). As more and more

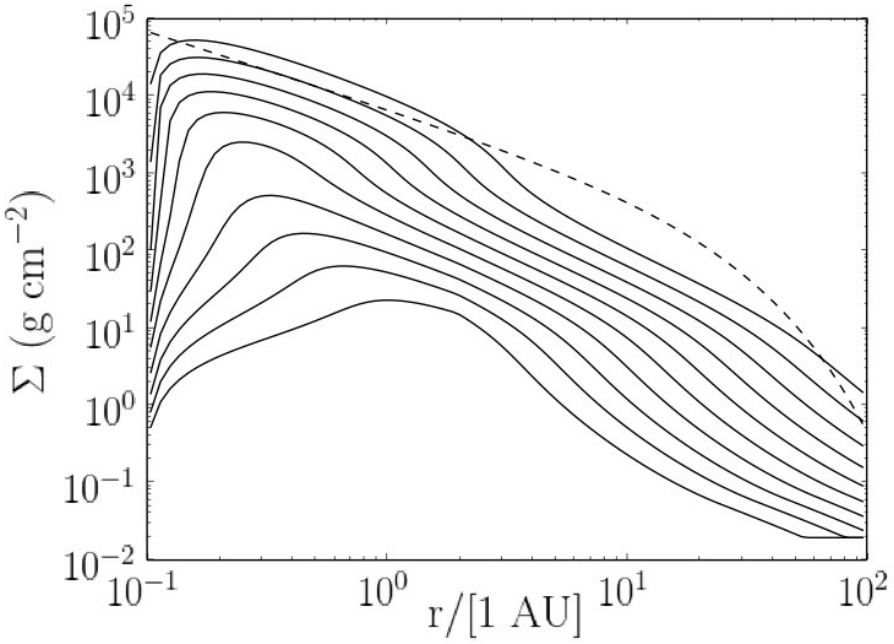

Figure 9: $\Sigma(r,t)$ for the canonical computed α case for the dust-free case without photoevaporation ($G_0 = 1$). Each curve shows the surface density profile at times 0 Myr (dashed), 1 Myr, 2 Myr, 3 Myr, .. , 10 Myr. Note the overall disk profile is maintained for several Myr.

mass falls onto the star, the inner disk becomes less dense enough to be sufficiently ionized. Movement of mass picks up and $\dot{M}_{\rm acc}$ go up by an order of magnitude in the inner disk. From Fig. 19, we see r_T move inward from around 7 AU at 1 Myr to 3 AU, as the disk radius r_D reduces to $\sim$ 50 AU. It is interesting to note how not only does the mass of the disk drop almost linearly with time, it keeps up this linearity with increase in $G_0 = 1000$ as well. From the above simulations, we see that unlike dust-free simulations, a dusty disk does not lose much mass with time (Fig. 19).

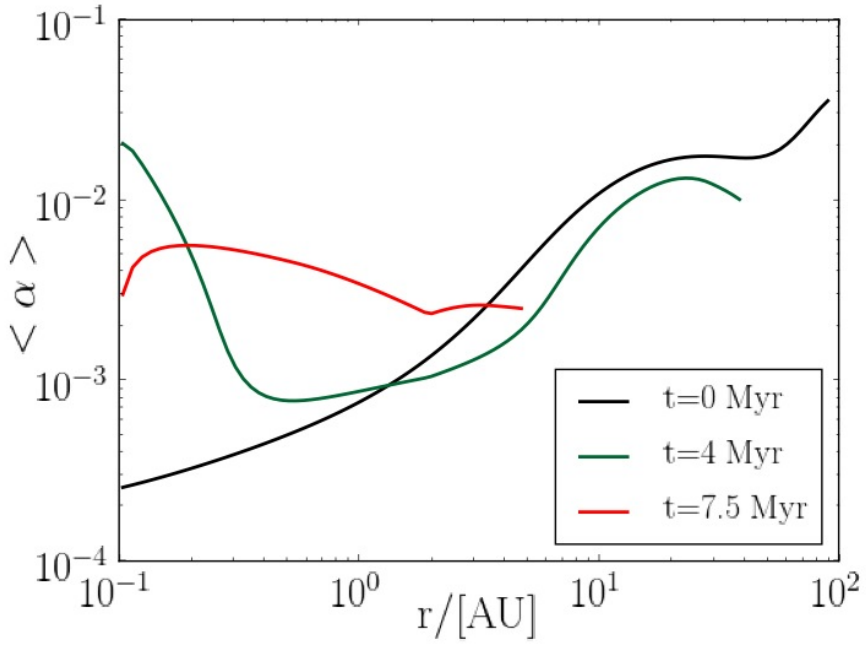

Figure 10: Vertically integrated and mass weighted $\langle\alpha\rangle$ as a function of r, at various times for the canonical computed α dust-free case with photoevaporation ($G_0 = 1000$). The curves are truncated at the disk radius r_d at each plotted time.

2.3.3 Effect of each parameter in a [gas+dust] disk with computed α

Effect of G_0

In runs 8, 9 and 10, we vary the flux of external FUV radiation illuminating the disk through $G_0 = 300$, 1000 and 3000. These results are plotted in Fig. 20 to show how various disk structure properties vary with time. Higher G_0 causes more mass loss in the outer disk. The high values of α between 0.001 to 0.1 due to high ionization fractions in the outer disk likely facilitates this rapid mass movement, and eases outward mass loss due to photoevaporation. As noted before, the linearly decreasing trend in the disk mass with time is kept up with an intermediate value of $G_0 = 300$, as well as $G_0 = 3000$ as well. Different values of G_0 typically show very steep initial slopes, flattening almost similarly with time. While higher G_0 truncates the disk to

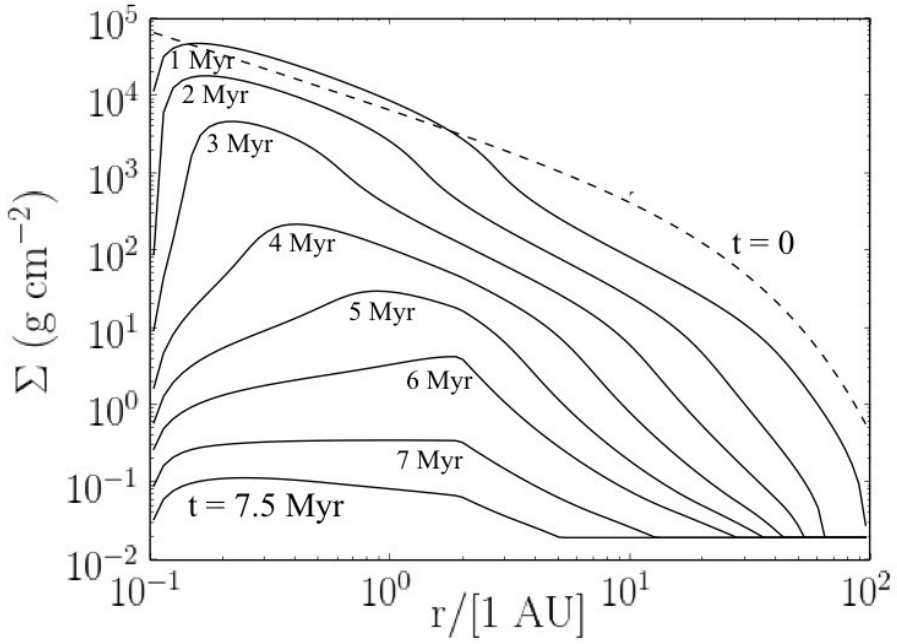

Figure 11: $\Sigma(r,t)$ for the canonical computed α case for the dust-free case with photoevaporation ($G_0 = 1000$). Each curve shows the surface density profile at times 0 Myr (dashed), 1 Myr, 2 Myr, .. , $t_{\rm final}$. $t_{\rm final} \sim 7.5$ Myr. Note that the disk rapidly shrinks to 5 AU within 7.5 Myr.

a smaller r_d, r_T does not show any such trend with increasing G_0. The r_T for G_0 of 1000 and 3000 are mainly similar throughout the simulation.

Effect of gas-to-dust (g/d) ratio

Runs 8, 11 and 12 show the effect of varying the gas-to-dust mass (g/d) ratio (Fig. 21). In these runs, we can see that the disk is effectively cleared within 10 Myr only when g/d = 10000. Higher g/d can be taken to be a proxy for grain growth. Therefore, it seems likely that rapid evolution of the inner disk is only possible with substantial grain growth. g/d=100 shows the other extreme case where the inner disk evolution is too slow that the mass in the outer disk is piled on top of the mass in the inner and middle disk creating an extremely steep slope. The outer disk edge r_d does not

change much with two orders of variation of (g/d) ratio till about halfway through the simulation. The transition radius r_T decreases from $\sim$ 15 AU after 1 Myr to $\sim$ 2 AU at 10 Myr.

Effect of β_g

Runs 8, 13 and 14 show the effect of varying the gas phase recombination coefficient β_g (Fig. 22) exploring the extremes of β_g between molecular-ion dominated chemistry ($\beta_g = 10^{-6}\,\mathrm{cm^3\,s^{-1}}$) and metal-atom dominated chemistry ($\beta_g = 10^{-11}\,\mathrm{cm^3\,s^{-1}}$). The highest value of β corresponding to recombination of molecular ion HCO^+ causes the disk to lose about half its mass compared to the other recombination rates. Slope varies wildly throughout r for the two lower values of β_g. Disk radius r_d and transition radius r_T do not seem to be very sensitive to gas recombination rates.

Effect of L_{xr}

Runs 8 and 15 vary the stellar X-ray luminosity by an order of magnitude, i.e. 10^{28} ergs s^{-1} (Fig. 23). We find that all disk properties (mass M_d, radius r_d, transition radius r_T and slope) that are tested are not sensitive to the change in X-ray luminosity.

Effect of Cosmic Ray Exclusion

In run 16 (Fig. 24), we removed cosmic radiation from our model to note the effect of the exclusion of cosmic rays on disk structure. While disk mass and outer radius does not seem to be sensitive to the presence or absence of cosmic radiation, the internal structure of the disk is still impacted by the absence of cosmic rays. Cosmic rays appear to be the primary source of ionization for the mid-regions of the disk (6-20 AU) that are not as optically thick as the disk interior. In the absence of cosmic rays, the disk develops very steep profiles over most of the simulation timescale (10 Myr),

as the middle regions of the disk are much less ionized than in the presence of cosmic rays. The outer flared disk is still ionized by X-rays and spreads to pile up on the relatively static middle disk, steepening the profile.

2.4 Conclusions

In this work, we have performed evolutionary simulations of protoplanetary disks subject to the influence of external photoevaporation (due to FUV radiation from a nearby massive star), and non-uniform viscosity due to the magnetorotational instability (MRI). For the latter, we have calculated the equilibrium ionization state at each radius r and height z of the disk with a simple gas-grain chemistry network. External photoevaporation is an efficient disk dispersal mechanism, and can dramatically alter disk evolution by steadily removing mass, and truncating the size of the disk. Rapid mass removal dictated by photoevaporation places lower limits on planet formation timescales due to disk dissipation. Half of all protostars are likely to be born in rich clusters containing at least one O star that would photoevaporate their protoplanetary disks (Lada & Lada (2003). There are also numerous lines of evidence that suggest that Sun's disk was photoevaporated in the past. Photoevaporation is therefore important to be included in disk models in order to understand the evolution of the solar nebula. It is also important to note that most disk models employ a uniform α, usually 0.01, as the coefficient of turbulent viscosity, which is not attributed to any particular physical mechanism. All considered physical processes would yield a non-uniform α through the radial extent of the disk. In this work, the widely-accepted magnetorotational instability (MRI) is taken to be the mechanism driving the angular momentum transport and viscosity in the disk. The operation of the MRI depends on the local ionization state of the disk and thus varies with r and z, causing α to also vary with r and z. Using the formulations of Bai & Stone (2011)

that include non-ideal MHD with ambipolar diffusion, we find that a varying α profile can drive mass movement dramatically differently in the disk and can therefore significantly affect disk structure.

2.4.1 Main results

Our simulations have explored the structure and evolution of a 0.1 $M_\odot$ disk around a 1 $M_\odot$ star over several Myr timescales, under the influence of a range of irradiating stellar birth environments and the inclusion of a prescription for non-uniform MRI-viscosity. The main results of our simulations incorporating all of the above effects are summarized below:

- We find that turbulent viscosity α derived from the MRI can vary over four orders of magnitude with r, i.e., from $< 10^{-5}$ in the inner disk to 10^{-1} in the outer disk. This variation is due to the difference in the ionization fraction throughout the disk. While the dense shadowed inner disk is largely neutral, the outer tenuous disk is highly ionized by both cosmic radiation, as well as X rays that reach the flared outer disk. This variation in α causes mass to move very slowly in the inner disk, but simultaneously drives rapid mass movement in the outer disk. Such a variation in mass transport creates an inherently steep profile in the early disk.

- Photoevaporation due to $G_0 = 1000$ is able to rapidly remove mass from the outer disk edge in timescales of $\sim$ few Myr, and truncate the disk outer edge, to $\sim$ 50 AU in 10 Myr in a dusty disk. In a disk with little or no dust, it rapidly dissipates the disk down to 5 AU within $\sim$ 7.5 Myr. Over and above the steep disk profile created by non-uniform α, photoevaporation steepens the slope in the outer disk (i.e., 5 - 30 AU) due to removal of mass from the other edge, but

by not as much as due to the radially varying α.

- An interesting result from our simulations is that in a photoevaporated disk, the transition radius r_T (i.e., the radius at which the direction of mass flow changes from inward into the star to outward) can move inward with time. This implies that external photoevaporation is able to move mass from the inner disk to the outer edge. This is unlike the case of a non-photoevaporated viscously spreading disk (e.g., LBP) where r_T moves outward with time.

- Higher FUV fluxes (e.g., $G_0 = 3000$) remove more mass from the disk, bringing the outer radius r_D as well as the transition radius r_T inward, and create steeper disk profiles in the outer disk. Lower FUV fluxes ($G_0 = 300$) have the opposite effect: they remove less mass from the disk and cause shallower disk profiles.

- Dust influences disk evolution by absorbing charges and drastically reducing the ion fraction in the dense disk interior. In our canonical case (g/d=1000 and $a_{\rm gr} = 1\mu$m), we find that the presence of dust lowers α, hindering inner disk evolution; infall onto the star plunges below $10^{-9}\,{\rm M}_\odot\,{\rm yr}^{-1}$. The effects of MRI-viscosity and external photoevaporation cause rapid dissipation of a dust-free disk within 7.5 Myr. In contrast, it is able to remove only about half of the disk mass in a dusty disk over 10 Myr. The presence of dust is thus able to create two different evolutionary pathways: a stalled evolution in the case of dusty disks, and rapid dispersal in the case of dust-free disks.

- It is important to note that we do not consider grain growth in our simulations (discussed later). However, employing a range of gas-to-dust ratio (g/d = 100, 1000, 10000) can be a proxy for grain growth. Our results show that grain growth must necessarily proceed efficiently until sufficient evolution of the inner

disk is allowed. Without efficient grain growth, the disk undergoes a stalled evolution where there is a large scale transport of mass from the outer higher-α disk to the lower-α interior.

- The value of $\alpha(r)$ can be affected by several factors, including how ionization processes ionize the disk across r as well as models of disk chemistry used in the simulations. An order-of-magnitude variation in $L_{\rm xr}$ does not affect the overall disk structure in a dusty disk. Cosmic ray exclusion, however, causes steep profiles in the mid-regions of the disk that are important for giant planet formation. Changing the disk chemistry also results in wildly varying slopes of the Σ profile with time.

2.4.2 Implications

Our results show that the disk evolves very differently from previous disk models such as the self-similar viscous evolution models (LBP; Hartmann et. al 1998) under the combined action of both non-uniform viscosity with dust and external photoevaporation, each of which contributes toward steepening of the disk profile. Here, we highlight some of the most important implications due to the variation of the structure and evolution of the non-uniform α-disk subject to photoevaporation.

Changes in the Disk Structure and Mass Transport

We find that the presence of dust dictates two distinct evolutionary tracks for non-uniform α disks subject to external photoevaporation. We describe each case separately as follows:

In the case without dust, the structure of the disk is significantly altered due to the difference in mass flow between the inner dense disk and the outer tenuous

disk. In a dust-free disk, α is an increasing function with r for several Myr, due to the differing ion fractions between the inner and outer disk, creating an initial steep surface density profile as seen in Fig. 10. α ranges over 2-3 orders of magnitude ($\sim$ few $\times\ 10^{-4}$ in the inner disk to $\sim 10^{-1}$ in the outer disk). This difference in magnitude is eventually reduced with time and the profile flattens out as the inner disk is cleared out by accretion onto the star, increasing the ion fraction in the interior and thus α. Determining the viscous timescale $t_{\rm visc}$ across the disk can lend a quantitative insight into the timescale of this mass transport process, for which the following expression is useful:

$$t_{\rm visc} = \frac{r^2}{\nu} \equiv \frac{(r/H)^2}{\alpha\Omega} \tag{2.27}$$

Assuming the disk is flaring slightly, using $\nu = \alpha\, H^2\, \Omega$ (from the parameterization of Shakura & Sunyaev (1973), as well as $c_s = H\,\Omega$), if α is a constant, then $t_{\rm visc} \propto r^{3/2}$. When we assume a non-uniform value of α, in a disk with little or no dust, we find α varies as $\alpha \propto r$ between 2 - 20 AU at $t = 0$. This leads to an initial value of $t_{\rm visc} \propto r^{0.5}$. Later at $t = 4$ Myr, as the α profile steepens to $\sim r^{1.4}$, $t_{\rm visc} \propto r^{0.1}$. The overall steady shape of the disk profile is maintained throughout the simulation as the rates of mass loss $\dot{M}_{PE}$ and $\dot{M}_{acc}$ match each other throughout the duration of 7.5 Myr.

In the case with dust, as seen in Fig. 16, the presence of dust exaggerates the already-increasing α profile as dust absorbs and removes charges from the inner disk. In a dusty disk, the α slope is steeper, i.e., $\alpha \propto r^{2.0}$ at $t = 0$ from 1-50 AU and later increases to $\sim r^3$ at $t = 5$ Myr within a 2-20 AU region. This leads to $t_{\rm visc} \propto r^{-0.5}$ at $t = 0$, increasing to $r^{-1.5}$ at 5 Myr. The $t_{\rm visc}$ effectively seems to decrease with radius through a large portion of the outer disk. Mass is therefore transported very rapidly from the outer disk into the inner disk (within a few AU). This is a robust result as this results from the initial steep profile that arises from the non-uniform α. This can also be seen in Fig. 18 where $\dot{M}_{\rm PE} > \dot{M}_{\rm acc}$. The disk initially loses more

mass to photoevaporation than accretion, and it takes several Myr for accretion rates to catch up to photoevaporative rates, steepening the already steep surface density profile in the outer disk. From the results of our simulations, we find that until grain growth is efficient, inner disk evolution is stalled and the disk develops a steep profile across the planet formation region (5 - 30 AU). If the disk evolves in this manner, while Jupiter may have sufficient Σ in its formation region to reach isolation mass, the other outer planets may be likely left with too little mass to grow, as the disk gas is likely to be dissipated out of the outer disk very quickly.

Comparison with the MMSN profile

Our results show that disks are more likely to evolve with steeper profiles than the MMSN profile (with slope $p = 1.5$). Desch (2007) had updated the MMSN profile with the positions of the giant planets in the compact configuration of the Nice Model (Tsiganis et al. 2005), and had found $p \sim 2.2$. Desch (2007) had attributed this steeper slope to be due to mass removal by external photoevaporation. In this study, we investigated the evolution of the protoplanetary disks subject to photoevaporation, and a non-uniform MRI viscosity. We find that while variable α steepens the disk dramatically, external photoevaporation also steepens it but by not as much. The presence of dust also significantly steepens disk structure, the extent of which is uncertain as grain growth has not been included in this study. It would be useful to compare our model disk profiles to MMEN surface density profiles derived from Kepler data, but these are pertinent only to the innermost 0.5 AU of the disk, where our models are potentially uncertain due to the assumed inner boundary condition. Nevertheless, we find in our models without dust, the inner disks (0.2 to 5 AU) evolve to a state similar to the MMEN profile of Chiang & Laughlin (2013) with Σ profile slope p $\sim$ 1.6 in the first 3 Myr (until the disk dissipates). In our models with dust,

the innermost regions (0.2 to 5 AU) have steeper slopes p $\sim$ 2.0 - 2.2, although not as steep as in their outer regions.

Planetary Growth Timescales

In order to determine how long it takes for planet cores to grow within the surface density profiles predicted for photoevaporated non-uniform α dusty disks, we use the planetary growth model employed by Desch (2007) [see equations 30-34 in Desch (2007)] that implements the growth rate equations of Ida & Makimo (1993). The eccentricity of the planetesimals is derived assuming an equilibrium between the effect of gas drag and gravitational stirring of the planet cores as given in Kokubo & Ida (2002), and the gas drag evaluated from the Reynolds number (Re) using the prescriptions from Weidenschilling (1977a). A uniform initial size of planetesimals is assumed to be 100m, similar to Desch (2007). Desch (2007) had considered a uniform non-varying surface density as well as a viscously evolving disk to calculate the growth timescales. We improve this model by taking a self-consistently decreasing solid surface density accompanying core growth with time.

Assuming that each core only accretes planetesimals from its own feeding region, we obtain the growth profiles as shown in Fig. 25 for our canonical photoevaporated dusty disk case.

From the growth profiles, we note that the cores of Jupiter and Saturn grow until 0.5 Myr, while Neptune and Uranus take up to 2 Myr to accrete all the planetesimals in their feeding regions. We also note that while photoevaporation does not affect the growth of Jupiter's core, which rapidly accretes $\sim$ 90 $M_\oplus$ in 0.5 Myr due to higher local Σ, higher FUV fluxes are able to significantly stunt the growth of Saturn's core. FUV fluxes corresponding to $G_0 > 1000$ may not allow Saturn to accrete sufficient solid mass matching the predicted present-day value of 9 - 22 $M_\oplus$ (Desch 2007). Neptune

and Uranus grow negligibly even without photoevaporation as they are not able to accrete mass quickly enough before the disk dissipates. More rapid growth timescales or migration of large planetesimals into the outer disk may be needed to explain their core growth. However, our models do not include grain growth, which could potentially make the Σ profile more shallower allowing for more mass transported to the feeding regions of the outer ice giants, potentially leading to more core growth.

Radial Volatile Transport

Lastly, we also argue that photoevaporation also dramatically affects radial transport of volatiles. Takeuchi & Lin (2002) have argued that if the sum of the slope p of the surface density profile and the slope q of the temperature profile (Equation 2.8) is $>$ 2, then the volatiles are transported radially outward in the nebula. In our work, we assume a typical temperature profile with $q = 0.5$, and we find steep surface density profiles with slope $p > 2$. Thus, in our disks, the sum of the slopes $p+q > 2$, supporting outward volatile transport. From our simulations, we predict that photoevaporation is able to remove volatiles (such as H_2O) efficiently through the disk outer edge even from as far in as the inner disk. This is a result from our simulations that in a photoevaporated disk, the transition radius r_T can move inward with time as opposed to a non-photoevaporated viscously spreading disk, where r_T increases with time (Hartmann et al. 1998) as $r_T \propto T^{0.5}$. This results in more and more mass being removed from the inner disk, the region of terrestrial planet formation. Indeed, r_T in some disks go as far inward as ~ 3 AU. Significant loss of volatiles from the inner disk material can severely affect the potential for future habitability of planets that form in the volatile-depleted inner disk.

2.4.3 Future Work

An important caveat of our models is that we do not yet include grain growth. In the absence of grain growth, dust efficiently stagnates inner disk evolution. Accretion is very slow and mass transported from the highly ionized outer disk just accumulates in the middle and inner disk. We predict that with grain growth, the inner disk will be able to accrete onto the star after grain growth proceeds efficiently in 1-2 Myr, and increase accretion rates such that disk evolution is quickened. This way, the steep profile erected by the initial stagnation of the disk will gradually flatten with time. Such a disk may then have enough mass and time for the growth of the four giant planets across 5-30 AU. However, it is also likely to be dissipated quickly with time (as seen in g/d=10000 case in Fig. 21, where a higher g/d can be considered as a more advanced stage of grain growth).

2.4.4 Summary

In this work, we have performed simulations of protoplanetary disk evolution where we have included the effects of i) external photoevaporation ii) MRI-derived non-uniform viscosity, and iii) a simple gas-grain chemical network to calculate ionization equilibrium state in the disk. From our simulations, we argue that it is important to consider both external photoevaporation and non-uniform viscosity in disk models as each contributes strongly in altering the disk profile in a unique manner. Models incorporating external photoevaporation and a realistic prescription of viscosity and angular momentum transport may bring us closer to the behavior and evolution of the physical processes that transpired in the solar nebula that shaped the structure of the Sun's protoplanetary disk and determined the composition of the terrestrial and the giant planets.

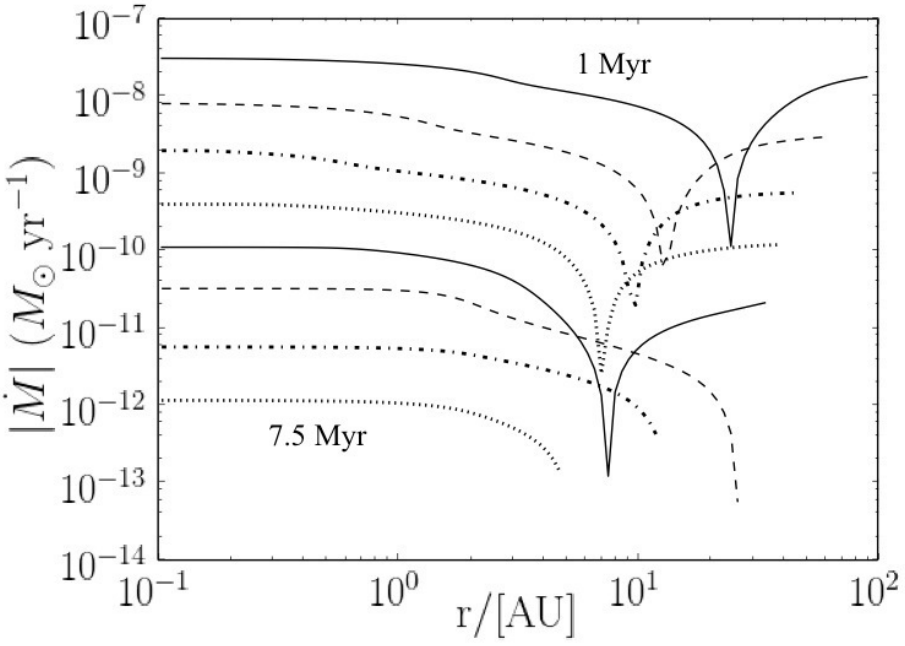

Figure 12: $\dot{M}$ profiles of the disk for each successive Myr: 1Myr, 2 Myr, .. , 10 Myr (solid, dashed, dot-dashed, dotted..) for the canonical computed dust-free α case with photoevaporation ($G_0 = 1000$). The dip in each curve denotes r_T, which is independently plotted in Fig 11.

Acknowledgements

This work was supported by grants from the NASA Astrobiology Institute, Nexus for Exoplanet System Science (NExSS) and Keck Institute of Space Studies. We thank Neil Turner for helpful discussions. The results reported herein benefitted from collaborations and/or information exchange within NASA's Nexus for Exoplanet System Science (NExSS) research coordination network sponsored by NASA's Science Mission Directorate.

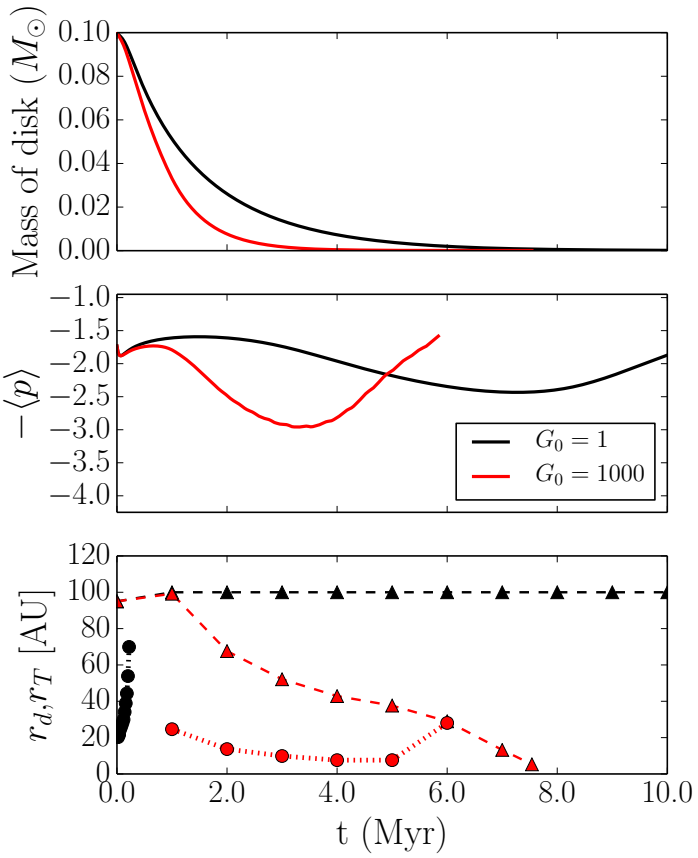

Figure 13: Change in the disk properties (disk mass M_d, slope $\langle p \rangle$ of $\Sigma(r)$, disk outer edge r_d and transition radius r_T) with time for the canonical varying α dust-free case with photoevaporation ($G_0 = 1000$; red). Black curves show the non-photoevaporated case ($G_0 = 1$ with other parameters unchanged) for comparison. Same as in Fig. 6. r_T for the non-photoevaporated case moves beyond 100 AU within 1 Myr.

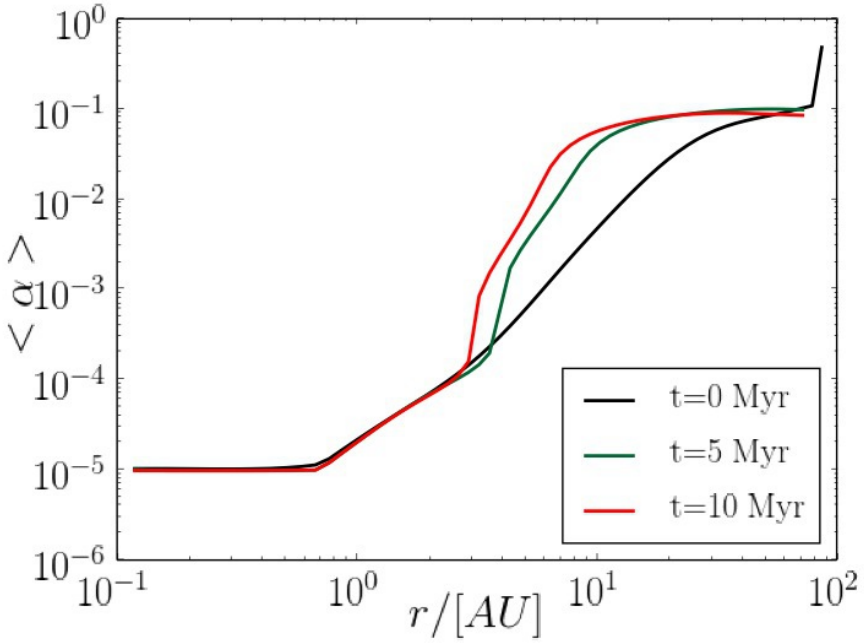

Figure 14: Vertically integrated and mass weighted $\langle \alpha \rangle$ as a function of r, at various times for the canonical computed α case with dust (without photoevaporation; $G_0 = 1$)

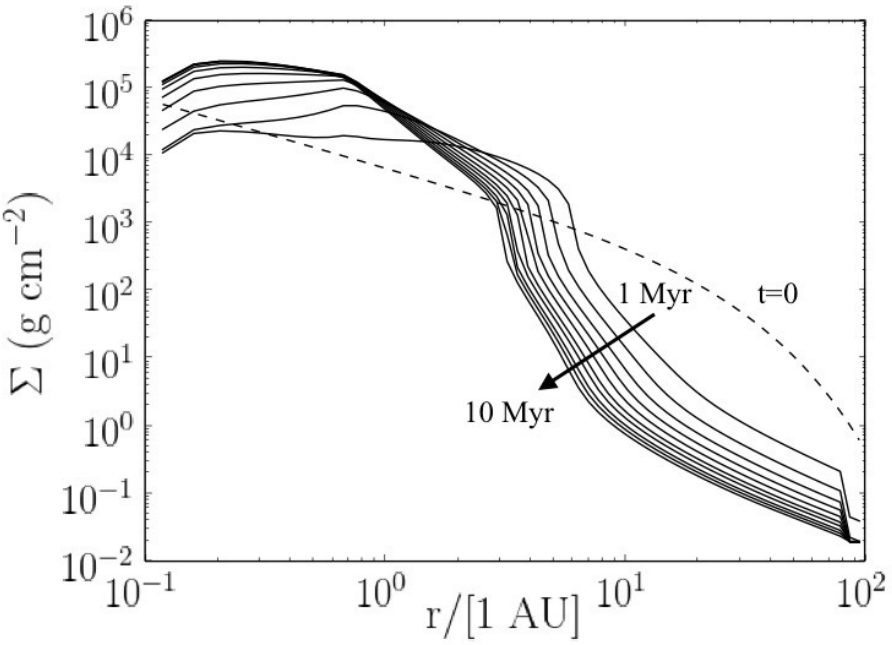

Figure 15: $\Sigma(r,t)$ for the canonical computed α case with dust for a non-photoevaporated disk ($G_0 = 1$). Each curve shows the surface density profile at times 0 Myr (dashed), 1 Myr, 2 Myr .., 10 Myr. Note that the dust stalls the inner disk evolution and there is a large-scale distribution of mass towards the inner and mid-disk.

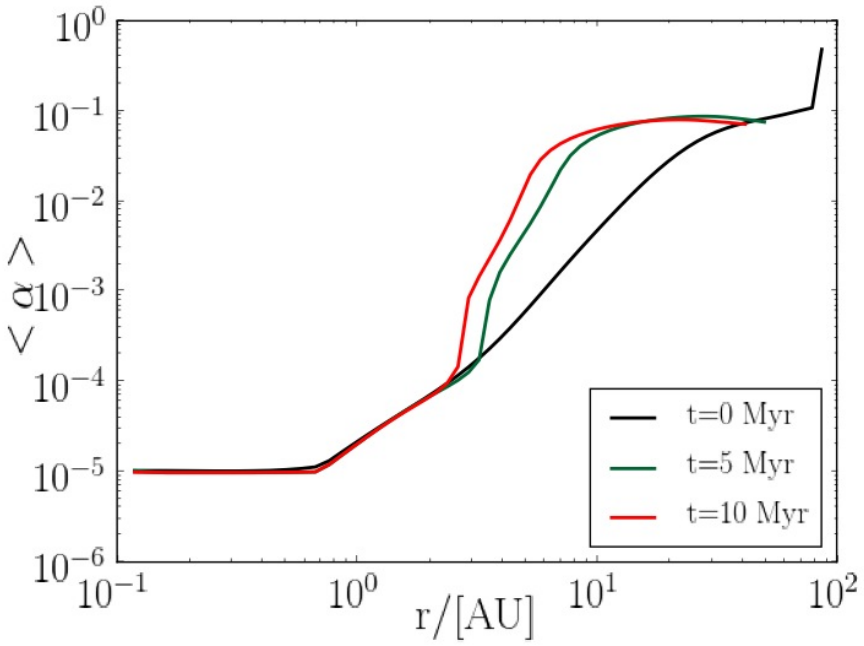

Figure 16: Vertically integrated and mass weighted $\langle \alpha \rangle$ as a function of r, at various times for the canonical computed α case with dust (with photoevaporation; $G_0 = 1000$).

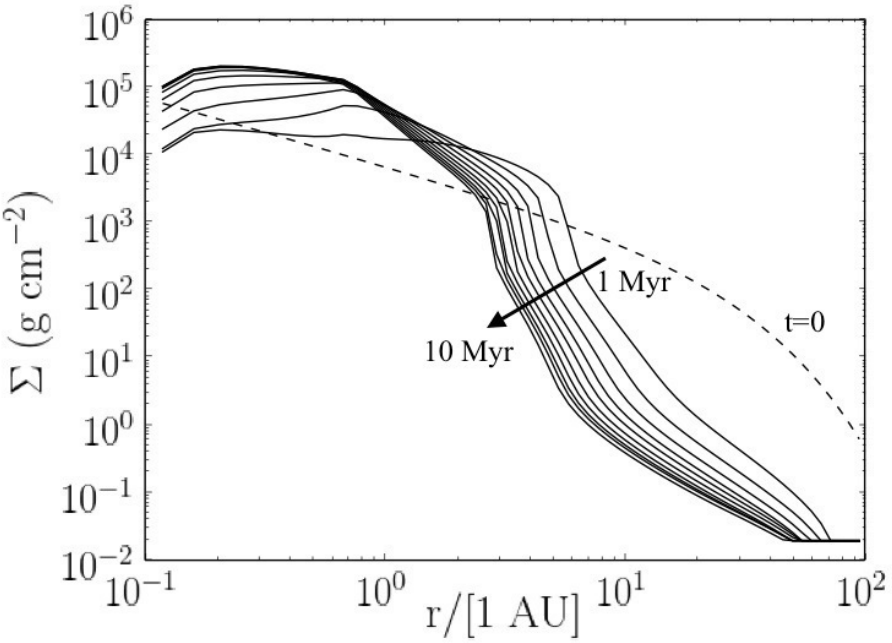

Figure 17: $\Sigma(r,t)$ for the canonical computed α case with dust for a photoevaporated disk ($G_0 = 1000$). Each curve shows the surface density profile at times 0 Myr (dashed), 1 Myr, 2 Myr, .. , 10 Myr. Note that the dust stalls the inner disk evolution and there is a large-scale distribution of mass towards the inner and mid-disk, and the disk is truncated to ~ 50 AU within 10 Myr.

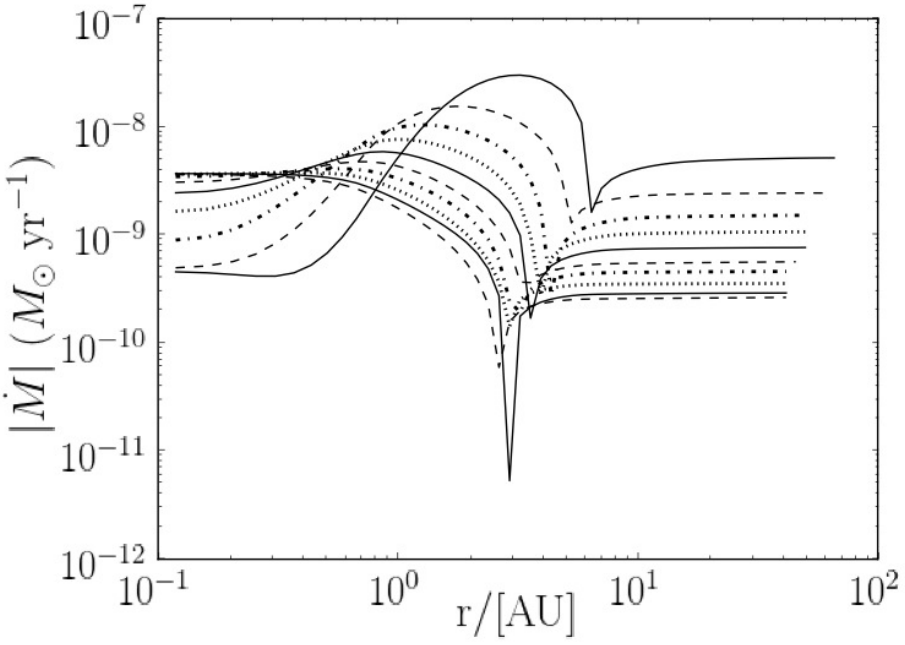

Figure 18: This plot shows the $\dot{M}$ profiles of the disk for each successive Myr: 1Myr, 2 Myr, .. , 10 Myr (solid, dashed, dot-dashed, dotted...) for the canonical computed α case with dust and photoevaporation ($G_0 = 1000$). Dips in each curve represent r_T, where mass flow in the disk changes direction from inward to outward. Note how r_T moves inward with time (independently plotted in Fig. 19).

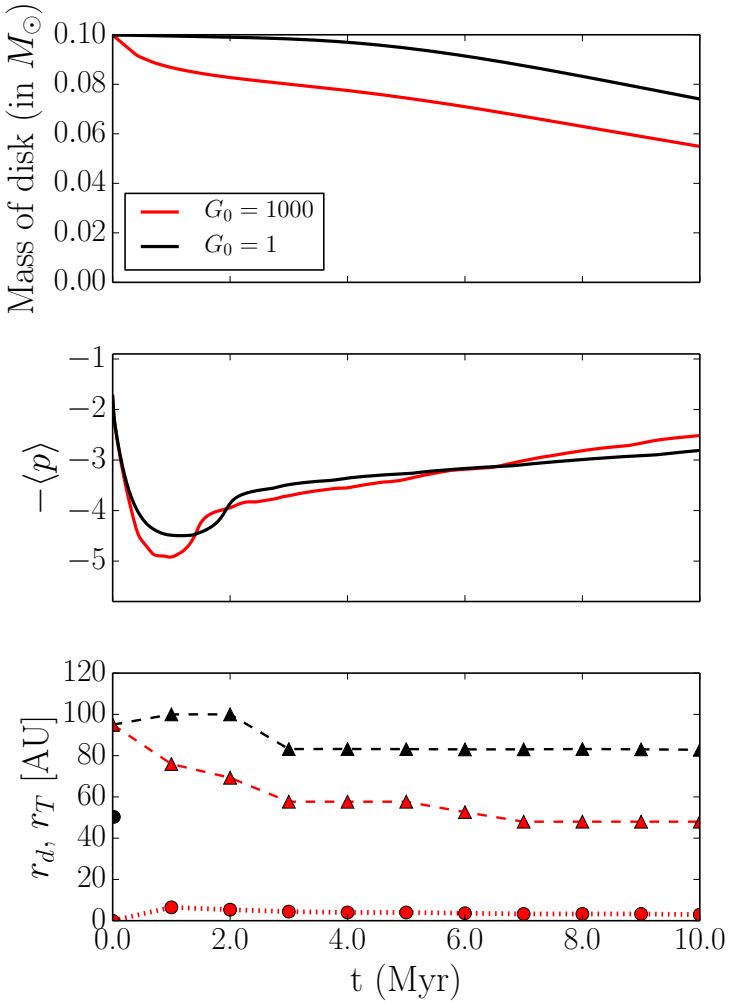

Figure 19: Change in the disk properties (disk mass M_d, slope $\langle p \rangle$ of $\Sigma(r)$, disk outer edge r_d and transition radius r_T) with time for the canonical varying α case with dust, and subjected to photoevaporation ($G_0 = 1000$; red). Black curves show the non-photoevaporated case ($G_0 = 1$ with other parameters unchanged) for comparison. Same as Figs. 6 and 13. r_T moves beyond 100 AU in $\ll 1$ Myr (i.e., in 20000 yr) for the non-photoevaporated case.

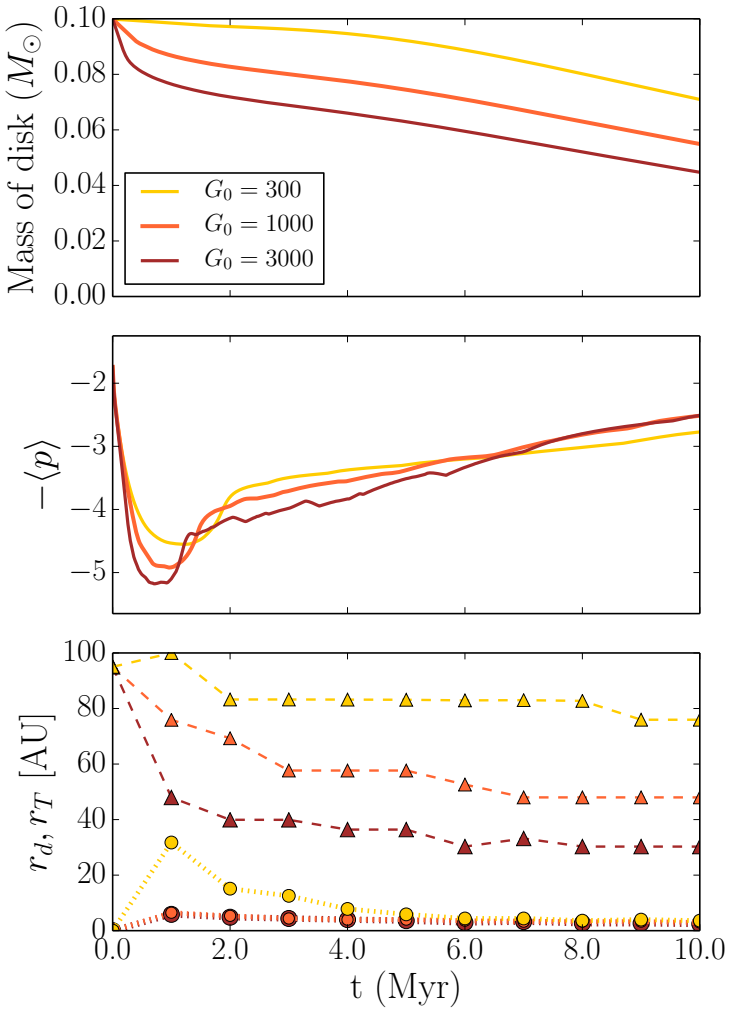

Figure 20: Effect of variation of G_0 on disk properties (disk mass M_d, slope $\langle p \rangle$ of $\Sigma(r)$, disk outer edge r_d and transition radius r_T) with time for the canonical computed α case with dust and subjected to different FUV fluxes (G_0 = [300, 1000, 3000]). Same as Fig. 7

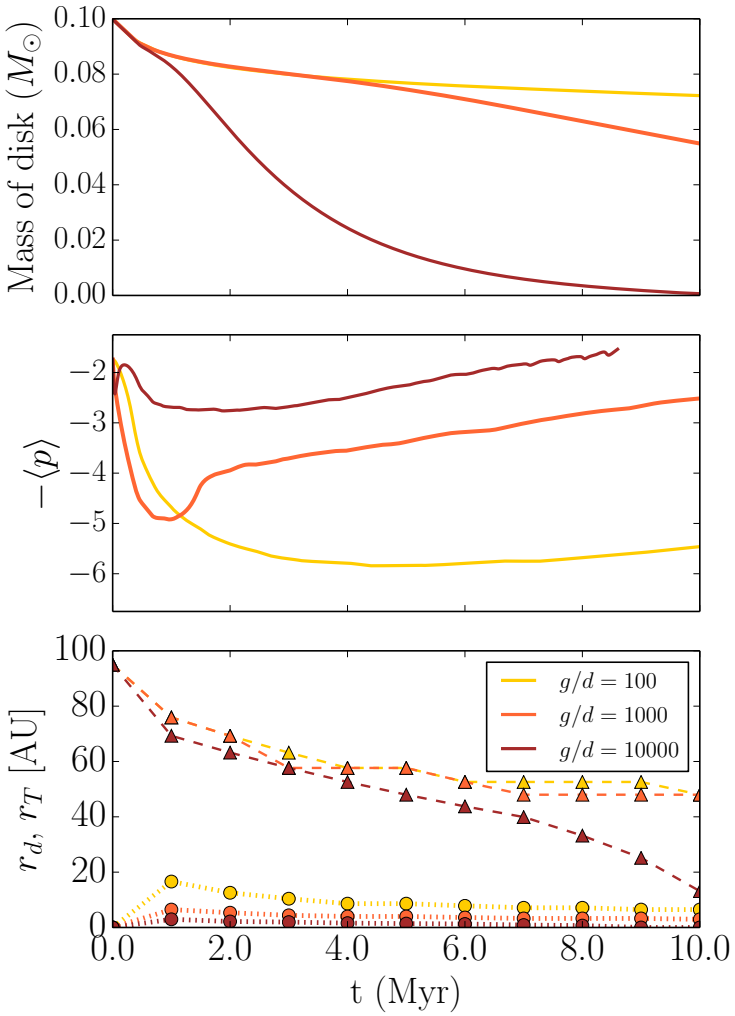

Figure 21: Effect of variation of gas-to-dust (g/d) ratio on disk properties (disk mass M_d, slope $\langle p \rangle$ of $\Sigma(r)$, disk outer edge r_d and transition radius r_T) with time for the canonical computed α case with dust and subjected to photoevaporation ($G_0 = 1000$). A range of (g/d) [100, 1000, 10000] was explored. Same as Fig. 7

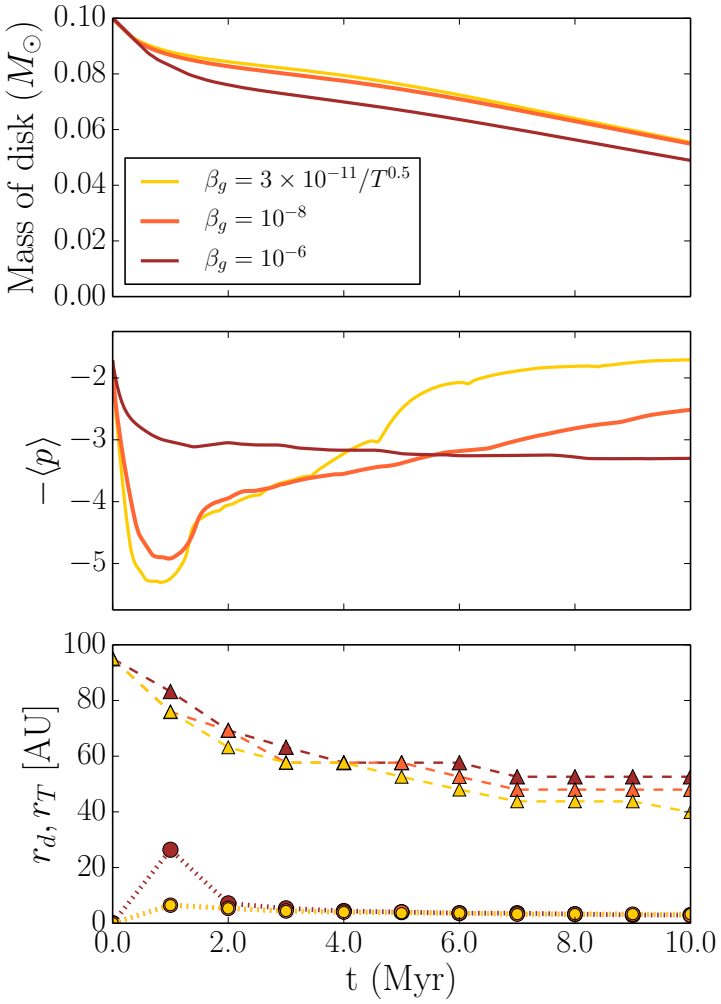

Figure 22: Effect of variation of the gas phase recombination coefficient β_g on disk properties (disk mass M_d, slope $\langle p \rangle$ of $\Sigma(r)$, disk outer edge r_d and transition radius r_T) with time for the canonical computed α case with dust and subjected to photo-evaporation ($G_0 = 1000$). A range of β_g ($10^{-6}\,\mathrm{cm^3\,s^{-1}}$ for molecular ion dominated chemistry, $10^{-11}\,\mathrm{cm^3\,s^{-1}}$ for metal ion dominated chemistry as well as an intermediate value $10^{-8}\,\mathrm{cm^3\,s^{-1}}$ accounting for chemistry that is driven by both species) was explored. Same as Fig. 7.

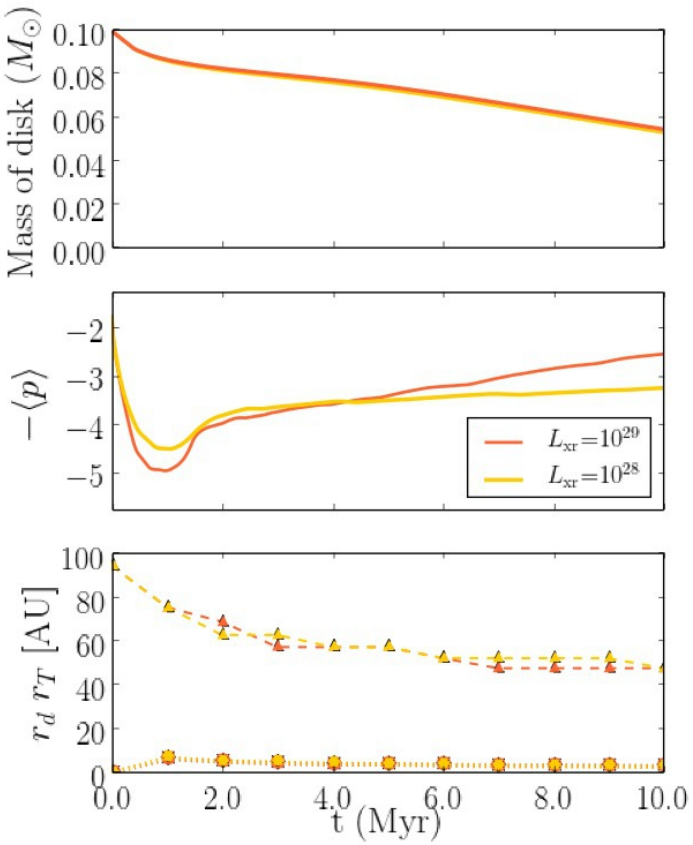

Figure 23: Effect of variation of L_{xr} on disk properties (disk mass M_d, slope $\langle p \rangle$ of $\Sigma(r)$, disk outer edge r_d and transition radius r_T) with time for the canonical computed α case with dust and subjected to photoevaporation ($G_0 = 1000$). L_{xr} of 10^{28} and 10^{29} ergs s^{-1} were explored. Same as Fig. 7

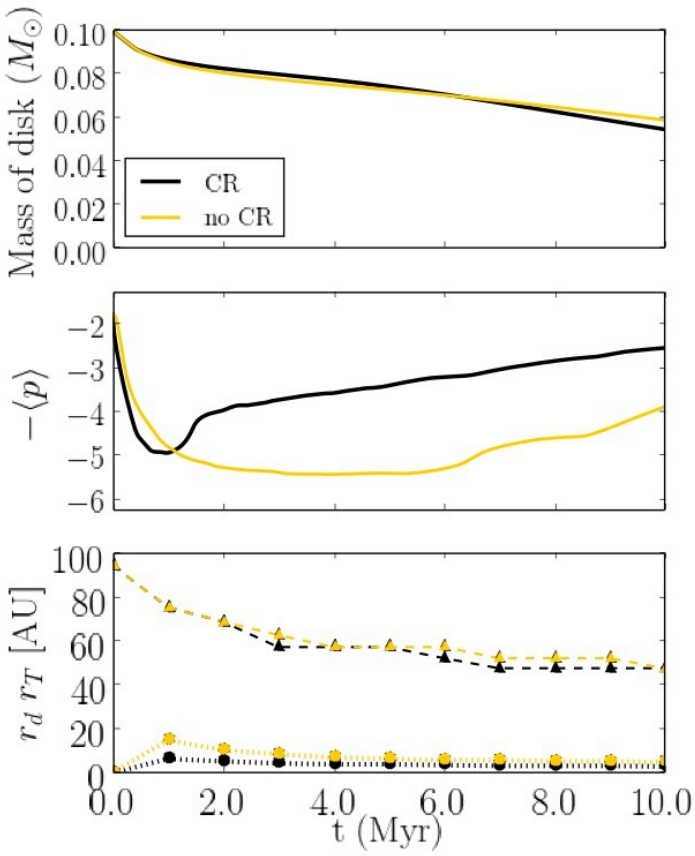

Figure 24: Effect of exclusion of cosmic rays (CR) on disk properties (disk mass M_d, slope $\langle p \rangle$ of $\Sigma(r)$, disk outer edge r_d and transition radius r_T) with time for the canonical computed α case with dust and subjected to photoevaporation ($G_0 = 1000$). Same as Fig. 7.

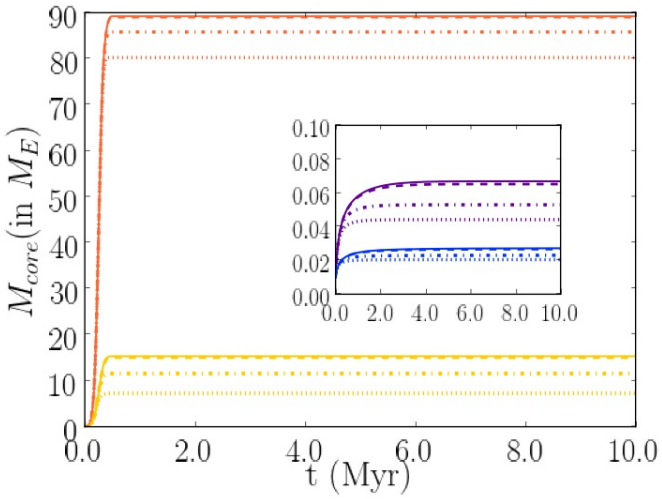

Figure 25: Effect of photoevaporation on the growth of core masses with time. The four planet cores are represented by color (orange: Jupiter, yellow: Saturn, violet: Neptune (inset), blue: Uranus (inset). Different photo evaporative FUV fluxes are represented by solid, dashed, dashed-dotted and dotted lines for G0 = 1, 300, 1000, 3000 respectively. The inset axes labels are the same as that of the plot axes.

Chapter 3

EFFECT OF DIFFERENT ANGULAR MOMENTUM TRANSPORT MECHANISMS ON THE DISTRIBUTION OF WATER IN PROTOPLANETARY DISKS

This chapter is a reproduction of the text of a document with the same title being prepared for publication to *The Astrophysical Journal*.

3.1 Introduction

A snow line is the boundary in a protoplanetary disk between the region near the star where a condensible volatile, especially water, is present as vapor, and far from the star where it is present as a solid. The location of a snow line depends on the pressure-temperature conditions in the disk (Hayashi 1981; Stevenson & Lunine 1988). Beyond the snowline, solid particles can drift inward by aerodynamic drag as they lose angular momentum moving against the pressure-supported gas (Weidenschilling 1977). Ice on such particles sublimates to vapor as they drift inward through the snow line. This vapor is able to diffuse relative to the gas, both inward and outward. Vapor diffusing outward across the snow line can condense as ice and be "cold-trapped" beyond the snow line (Stevenson & Lunine 1988). A bidirectional flow of water across the snow line is thus established. The location of the snow line in the disk is straightforwardly set by the pressure and temperature of the disk, and is typically where the midplane temperature is about 160 K to 180 K (Lodders 2003). In contrast, the distributions of water and volatiles across the snow line region—whether the abundance of water ice is enhanced or depleted beyond the snow line, or whether the water vapor abundance inside the snow line is enhanced or depleted—depend subtly on the relative rates of

different radial transport processes. The radial distribution of water in protoplanetary disks is likely the first step in determining the bulk volatile content that planetesimals accrete and can indicate potential regions of formation of habitable planets. The mechanics of radial transport affects not just the distribution of water, but other volatiles as well. The chemical inventories of planetesimals (asteroids) and planets forming in a disk will depend on the radial distributions of these species in the disk. Some major condensible species, e.g. CO, have their own snow lines (Öberg et al. 2011). Other volatiles, e.g., NH_3, are trace species, but are expected to condense with water (Dodson-Robinson et al. 2009). The chemical equilibria of these and other species are affected by the abundances of volatiles in the disk at different radii r (Cuzzi & Zahnle 2004; Najita et al. 2013). Modeling the distribution of all volatile species therefore depends on understanding how volatile distribution at the water snow line operates.

Besides affecting the distribution of chemical species in the disk, snow lines also can directly affect the growth of planets. Water ice also can enhance coagulation rates of icy particles over those of bare silicate particles because of ice's higher sticking coefficient (Gunlach & Blum 2015). An enhancement in solid mass density beyond the snow line is also possible due to the cold-trapping of vapor diffused across the snow line (Stevenson & Lunine 1988; Ros & Johansen 2013). This can directly enhance the coagulation rate as well, but may also increase the solids-to-gas ratio above the critical threshold for triggering planetesimal growth via the streaming instability (Johansen et al. 2007). The increase in solids-to-gas ratio also can lower the ionization of the gas beyond the snow line. If the disk is evolving by magnetorotational instability, this would lead to a local decrease in the angular momentum transport, and a local build up of gas. This in turn can lead to a localized pressure maximum in which particles can concentrate, further enhancing planet growth (Kretke & Lin 2008). These factors

may have led to rapid formation of Jupiter at the snow line in the solar nebula.

As depicted in Figure 26, the location of the snow line and the radial distribution of water and volatiles depend on the thermal structure of the disk and the relative rates of several transport processes, including advection and diffusion of vapor and particles, and radial drift of particles by aerodynamic drag (e.g., Cuzzi & Zahnle 2004; Ciesla & Cuzzi 2006). All of these processes are strongly affected by the angular momentum transport in the disk, parameterized by the dimensionless parameter α. Not only the strength of the turbulence (the magnitude of α), but the spatial structure of α (how it varies in the disk with r, the distance from the star) can affect these processes. The goal of this paper is to quantify how the strength and spatial structure of turbulent viscosity, parameterized by $\alpha(r)$, affect the radial distribution of water across a protoplanetary disk. This will improve first-principles models, allowing them to predict how much water an exoplanet may have accreted, based on other observable data.

3.1.1 Observations of the Water Snow Line Region

Observational constraints greatly assist these modeling efforts but by themselves do not allow firm predictions of exoplanet water contents. Constraints on the radial distribution of water in disks most commonly come from studies of the water content of solar system bodies, or from infrared or millimeter observations of water vapor.

Within the solar system, a clear gradient in water content is observed. Earth, at 1 AU, probably accreted ≈ 8 oceans' worth of water, for a mass fraction 0.2wt% (Wu et al. 2018). Mars may have accreted $\sim$ 1wt% water (Wanke and Dreibus 1994). S-type asteroids present largely inside 2.7 AU (Gradie & Tedesco 1982; De Meo and Carry 2014) are associated with ordinary chondrites which accreted with $\sim$ 1 wt% water (Hutchison et al. 1987; Alexander et al. 1989; Alexander et al. 2013), whereas

C-type asteroids beyond 2.7 AU are associated with carbonaceous chondrites with a few percent, up to 13wt% H_2O (as hydrated silicates; Alexander et al. 2013). The icy satellites of Jupiter and the other planets, as well as Kuiper Belt Objects, are roughly 50wt% ice (Brown 2012). Thus a snow line is inferred at roughly 2.7 AU, beyond which the water abundance of planetary materials increases sharply. However, it is not clear how much this distribution was affected by the presence of Jupiter (e.g., Morbidelli et al. 2016), or by the particular transport mechanisms acting in our protoplanetary disk that might not act in other disks.

Infrared observations of existing protoplanetary disks provide useful information about the abundance of warm water vapor inside the snow line, but the snow line itself is not resolved by such observations, as its close promixity (< 5 AU) to the central star means it subtends only tens of milliarcseconds at typical disk distances (Pontoppiddan et al. 2014; Notsu et al. 2016). Instead, high-resolution spectroscopy in combination with models is used to infer the distribution of water. An approximate snow line location has been estimated by inferring the temperature of H_2O vapor emission, using mid-infrared lines (Meijerink et al. 2009; Zhang et al. 2013). Meijerink et al. (2009) inferred that water vapor is abundant in the inner portions of disks, up to a few AU from the star, then rapidly decreases in abundances in the disk atmosphere beyond that. They argued that the vapor may have frozen out onto dust grains that sedimented toward the disk midplane. Zhang et al. (2013) performed the same analysis for TW Hya and found a dramatic drop in H_2O vapor abundance beyond 4 AU.

Millimeter observations, especially by the Atacama Large Millimeter Array (ALMA), can spatially resolve some features in disks that constrain snow lines. Zhang et al. (2015) inferred multiple snow lines due to different volatiles, in the gaps seen in HL Tau (ALMA Partnership, 2015); they argue that gaps in the substructure result from

enhanced pebble accretion at these condensation fronts. These conclusions are based on a chemical model with a number of implicit assumptions about disk chemistry, and in any case this study does not directly probe the water snow line. Notsu et al. (2016, 2017, 2018) have discovered a new method using high-dispersion spectroscopy to find the location of the water snow line, using specifically selected emission lines of H_2O vapor (with low Einstein A_{ul} values and high upper-level energies) that are likely to originate from the warm, innermost disk. This technique, they argue, is within ALMA's current capabilities.

Finally, serendipitous observations have constrained the instantaneous position of a snow line of an FU Orionis star in the midst of an outburst (Cieza et al. 2016). Because of the orders-of-magnitude increase in stellar luminosity during the outburst, the snow line was pushed out to 40 AU from the star, making it far enough to be spatially resolved.

The rapid improvement in observational techniques makes it likely that the location of the snow line will be constrained around many disks in the foreseeable future; but additional observations would be needed to constrain the abundance of water ice or water vapor on either side of the snow line. Substantial modeling is still required to build predictive models of exoplanet water content.

3.1.2 Models of the Water Snow Line Region

Many disk models have been developed to calculate the structures of disks, to determine the distance from the star at which the temperatures and pressures enable water vapor to condense onto small particles as ice (e.g., Ciesla & Cuzzi 2006; Garaud and Lin 2007; Dodson-Robinson et al. 2009; Min et al. 2011; Desch et al. 2018). These models differ in assumptions about certain key parameters affecting disk midplane temperatures, including the opacity of the disk material, κ (and its variation with

distance from the star, r, and the mass accretion rate $\dot{M}$ through the disk. Min et al. (2011), who performed full 3-D radiative transfer simulations of disks, summarized the effects of $\dot{M}$ and κ in Table 2 of their paper, and compared with the results of simulations in other works. In their canonical runs, the radius at which 50% of the H_2O exists as ice rather than vapor, $r_{\rm ice}$, varies from 0.7 AU for $\dot{M} = 10^{-6}\,M_\odot\,{\rm yr}^{-1}$, to 16.1 AU for $\dot{M} = 10^{-9}\,M_\odot\,{\rm yr}^{-1}$, at a fixed opacity. Alternatively, Min et al. (2011) found that for fixed accretion rate $\dot{M} = 10^{-8}\,M_\odot\,{\rm yr}^{-1}$, $r_{\rm ice}$ varies from 1.2 AU to 4.8 AU for κ across the range employed in different works (Min et al. 2011; Davis 2005a). Yet, while $r_{\rm ice}$ can vary considerably based on different inputs, it is relatively straightforward to calculate once those inputs are fixed.

In addition to fixing the location of the snow line, models try to determine the concentration of H_2O vapor (the molar ratio of H_2O gas to H_2), inside and just outside $r_{\rm ice}$, as well as the concentration of H_2O ice particles outside and just inside $r_{\rm ice}$. Higher ice-to-gas ratios beyond the snow line can encourage planetesimal growth (for example, the streaming instability is very sensitive to the solid-to-gas ratio; Youdin & Goodman 2005). Higher water vapor-to-gas ratios inside the snow line can provide a more oxidizing chemical environment. Whether vapor is enhanced relative to gas, or ice is enhanced relative to all solids, both depend on the relative rates of evaporation of ice and diffusion of vapor, the freezing of vapor onto solids and the diffusion of small solids, plus the drift of solid particles relative to the gas. Stevenson & Lunine (1988) first argued that over time the inner disk could become dehydrated as water vapor diffusing outward was cold-trapped beyond the snow line. They also argued that the surface density of solid material beyond the snow line would be enhanced by factors up to ~ 75, and could aid the growth of planetesimals and ultimately Jupiter at the snow line, presumably at around 5 AU. Cuzzi & Zahnle (2004) later performed semi-analytical calculations for volatile transport and argued that different inputs

could give rise to a variety of outcomes; besides the possibility outlined by Stevenson & Lunine (1988), there could be a time in the disk's evolution when the inner disk was enhanced in water vapor, if the flux of inward-drifting icy particles were higher than the outward flux of diffusing water vapor. The inner disk could then become depleted in water vapor at later times, as the inward flux of drifting particles decreased (among other things, they are accreted into larger planetesimals). These results were verified by the numerical simulations of Ciesla & Cuzzi (2006), who included the transport of vapor, dust, fast migrators, and immobile asteroids in the context of a disk evolution model. Some models also consider that icy solids may actually consist of multiple small silicate particles held together by ice, so that evaporation of the ice inside the snow line would lead to multiple, small grains dynamically coupled to the gas. Drift of large icy particles inward past the snow line would then result in an enhanced solids-to-gas ratio just inside the snow line, possibly triggering planet formation *inside* the snow line (Ida & Guillot 2016; Schoonenberg & Ormel 2017). All of these effects alter planet formation and chemistry near the snow line; and because the snow line moves inward over time as accretional heating decreases in the disk, ultimately a very large portion of the disk is influenced by these effects.

To model the distributions of water vapor and ice, and their effects on planet formation and chemistry, one must determine the relative rates of diffusion and drift and other transport processes. These, in turn, are strongly dependent on the turbulent viscosity, which regulates the diffusion and advection of vapor interior to the snow line, and diffusion and advection of solid particles outside the snow line. This can be seen by computing the timescale for volatile diffusion, $t_{\rm diff} \approx r^2/\mathcal{D} \approx r^2/\nu$, where r is the distance from the star, $\mathcal{D}$ is the diffusion coefficient, which is assumed to be $\mathcal{D} \approx \nu$, the coefficient of turbulent viscosity. The drift velocity of solids, which depends on the disk density is also is greatly affected by ν. Both diffusion and drift

depend on the sound speed c_s and therefore temperature, which depends on viscous heating and therefore also the turbulent viscosity ν. Moreover, as we argue below, it is not just the magnitude of ν that matters but also its spatial variation in the disk.

3.1.3 Turbulent Viscosity in Protoplanetary Disks

Turbulent viscosity affects just about every process in a protoplanetary disk. Mass accretion rates and timescales for viscous spreading depend on ν (Lynden-Bell & Pringle 1974; Hartmann et al. 1998). Viscous dissipation affects the temperature structure of the disk. Radial diffusion of vapor and particles depends on the degree of turbulence (Cuzzi & Zahnle 2004; Ciesla & Cuzzi 2006; Estrada et al. 2016; Desch et al. 2017). Turbulence affects the concentration of particles into larger particles (Cuzzi et al. 2003; Simon et al. 2018) and rates of planet growth by pebble accretion (Xu et al. 2017) and the final pebble isolation mass of the planet (Ataiee et al. 2018).

The coefficient of turbulent viscosity is typically parameterized using the alpha formulism of Shakura & Sunyaev (1973), in which $\nu = \alpha c_s H$, where c_s is the sound speed, $H = c_s/\Omega$ the scale height of the disk, and Ω is the Keplerian orbital frequency. Typically the dimensionless parameter α is assumed to be a constant value < 1 thoughout the disk, but it is unknown how well this assumption is justified because no physical mechanism for mass and angular momentum transport in protoplanetary disks has been definitively identified (Turner et al. 2014).

One possible constraint on α comes from the size distribution of chondrules, which appear to have been concentrated into chondrites by turbulence at levels of $\alpha \sim 10^{-4}$ (Cuzzi et al. 2001; Desch et al. 2018).

Observations of protoplanetary disks have place some constraints on α. Hartmann et al. (1998) considered the mass accretion rates onto T Tauri stars and the viscous spreading of their disks over times, concluding that $\alpha \sim 10^{-2}$ represented a typical

spatially and time-averaged value of α. Other studies reach similar conclusions: Hueso & Guillot (2005) found $\alpha = 10^{-3} - 10^{-1}$ for DM Tau and 4×10^{-4} to 10^{-2} for GM Aur; Andrews et al. (2009, 2010) found $\alpha \approx 5 \times 10^{-4}$ to 8×10^{-2} for disks in Ophiuchus. More recently, the Atacama Large Millimeter Array (ALMA) has been used to constrain the turbulent broadening of CO emission lines in the outer regions (> 30 AU) of resolved disks, finding $\alpha < 10^{-4} - 10^{-3}$ (Hughes et al. 2011; Guilloteau et al. 2012; Simon et al. 2015; Flaherty et al. 2015, 2017, 2018; Teague et al. 2016). These authors consider these values to be an upper limit, and low values of α are corroborated by other studies. Pinte et al. (2015) estimated $\alpha \sim 10^{-5}$ from the lack of smearing of concurrent dust rings and gaps in inclined disks. Observational surveys of disks in the Lupus star-forming region find disks too compact to have been viscously spreading (Ansdell et al. 2018). Rafikov (2017) argued that the lack of correlation between α (determined from mass accretion rates onto the central star) and other disk properties (e.g., disk mass, size, surface density, stellar mass, radius, or luminosity) means that turbulent viscosity cannot be the major driver of disk evolution, and therefore α must be low. In combination, these observations suggest $\alpha \approx 10^{-4} - 10^{-3}$ in the outer regions of protoplanetary disks. Evidently, the average values of α in protoplanetary disks are not well constrained observationally. It is therefore not yet possible to directly constrain the spatial variation of α in disks observationally as well. Models may be required to constrain α in disks.

Many disk models have considered magnetohydrodynamics (MHD) mechanisms as the cause of angular momentum transport, especially the magnetorotational instability (MRI) of Balbus & Hawley (1991). Under the assumption of ideal MHD, the MRI is expected to yield a uniform α with high value ($\alpha \sim 10^{-2}$) throughout the disk (Balbus et al. 1998 Rev Mod Phys). It has long been recognized, however, that protoplanetary disks are subject to non-ideal MHD effects, especially Ohmic dissipa-

tion, which will suppress the MRI at the disk midplane over a large range of distances from the star (Jin 1996; Gammie 1996). The result would be 'dead zones' between a few times 0.1 AU and about 10 AU, in which α is very low (perhaps 10^{-4} or less) Additional effects of ambipolar diffusion (Kunz & Balbus 2004; Desch 2004; Bai & Stone 2011; Simon et al. 2013a,b; Gressel et al. 2015) and the Hall effect (Wardle & Ng 1998; Bai 2014, 2015; Lesur et al. 2014; Simon et al. 2015) have been considered as well. Within 10 AU, ambipolar diffusion will suppress the MRI in the surface layers away from the disk midplane. The Hall effect depends on the orientation of the magnetic field relative to the disk rotation, and can lead to more or less angular momentum transport (Bai 2014; Lesur et al. 2014; Simon et al. 2015; see §2). In general, Hall effects suppress the MRI inside 10 AU except in regions of modest density in certain circumstances.

The recognition from models that the MRI is efficiently suppressed in large regions of protoplanetary disks, combined with observations of α in outer disks far lower than expected for MRI-active disks, has led to a resurgence of disk evolution models including purely hydrodynamic instabilities, or hydrodynamic instabilities in concert with magnetically driven winds. Hydrodynamic instabilities such as vertical shear instability, or VSI (Stoll & Kley 2014; Flock et al. 2017), convective overstability (Klahr & Hubbard 2014; Lyra 2014), and Zombie Vortex Instability (Marcus et al. 2013, 2015) typically yield $\alpha \sim 10^{-4}$ throughout the disk (Malygin et al. 2017; Lyra & Umurhan 2018). The variation of α across the disk would depend on the local cooling timescale, and probably would not be uniform across the disk. Magnetically driven winds are expected to act inside about 1 AU, augmenting α due to hydrodynamic turbulence (Suzuki et al. 2016).

Overall, theoretical models strongly suggest that α could vary across the disk. In our modeling of snow lines we therefore adopt three different profiles of $\alpha(r)$. We

consider a uniform α case, but also a case due to the MRI acting in a disk with a dead zone, and a case in which VSI is augmented by magnetic disk winds in the inner disk. These profiles of $\alpha(r)$ are discussed in detail in §2.2.

3.1.4 Overview

In this paper we investigate, for the first time, the effects of spatially varying α on the distribution of water and volatiles in protoplanetary disks. The relative rates of diffusion and particle drift depend on the magnitude of α, because the flux of water vapor transported by diffusion out beyond the snow line is proportional to α. But the flux of particles inward across the snow line depends on the density of gas, and tends to be higher for lower gas densities. Lower gas densities are associated with high α, which leads to mass rapidly accreting onto the star. Both the inward drift of icy particles and the outward diffusion of water vapor increase with α. The concentration of vapor inside the snow line and the concentration of icy solids beyond the snow line depend sensitively on the balance between these two rates. Therefore it may matter whether α is decreasing or increasing with r across the snow line. The different possible physical mehcanisms for angular momentum transport lead to different profiles for $\alpha(r)$ which, we hypothesize, could affect the distribution of water across the snow line.

We consider three distinct, physically motivated radial profiles of α (see Figure 27), and we investigate the effect of each on disk evolution and the radial distribution of water across the snow line—and ultimately throughout the disk. We examine how the distribution of water and volatiles depends not just on the overall value of α in a disk, but on the gradient of $\alpha(r)$ in a disk, especially across the snow line. The paper is organized as follows. In §2 we describe the details of our code for calculating disk evolution and volatile transport, and the assumptions underlying our snow line model.

In §3 we describe the results of a suite of disk simulations assuming different $\alpha(r)$ and a parameter study conducted to understand the effects of various assumptions about particle properties. In §4 we compare these numerical outcomes with theoretical and observational studies of disks, and with solar system data from meteorites. We conclude that different profiles of $\alpha(r)$ yield subtle but distinct radial distributions of water in protoplanetary disk.

In this work, we present the first effort that we are aware of, to investigate the effect of radially varying turbulence efficiency on the redistribution of volatiles through the snow line, and thereafter track redistribution of the water content in the framework of a full disk evolution model. Water is transported through the snow line in two forms: one, as diffusing vapor, and second, as ice deposited on the surfaces of drifting small solids (see Figure 26). The rates of transport of these different processes beginning at different sides of the condensation front would depend strongly on the turbulent α viscosity in that location. Our goal is therefore to understand how radially varying α would affect the transport and distribution of water in the solar nebula.

In this work, we will motivate three distinct radial profiles of α (see Figure 27) and investigate the effect of each on disk evolution and radial diffusion of volatiles and small solids, as well as the radial drift of these solids. These processes matter most at the snow line, and this eventually determines the volatile content of the entire radial extent of the disk. In this work, we attempt to bring together the advancements in the topics of turbulent transport as well as observations and modeling of disk volatiles by attempting to answer the following questions: 1) How is the water distribution different in highly viscous and less viscous disks? 2) How does a gradient in α reshape the redistribution of volatiles across the snow line? 3) What effect do profiles of different radially varying turbulent viscosity ultimately have on the global water distribution in the disk?

This paper is organized as follows: i) in §2, we will describe the details of our volatile transport code and lay out the assumptions of our snow line model; ii) in §3, we will describe the results of the suite of disk simulations that employ different $\alpha(r)$ and the parameter study conducted to understand the effects of assumed properties of volatiles and small solids; and finally, iii) in §4, we will discuss how our results fit into the context of disk evolution and volatile transport as presently understood from theoretical, observational studies of disks, and solar system meteoritic data.

3.2 Methods

3.2.1 Disk Model

Structure and Flow of the Bulk Gas

Our underlying disk model is described in detail in our previous paper (Kalyaan et al. 2015; hereafter Paper I). The 1(+1)D explicitly propagated finite-difference disk code features a protoplanetary disk of 100 AU in size, discretized into a logarithmic grid from 0.1 - 100 AU, and evolved using the canonical equations of Lynden-Bell & Pringle (1974) of an axisymmetric viscously evolving disk. In what follows we assume the disk is vertically well-mixed.

We consider a disk passively heated by starlight and actively heated by viscous dissipation, as described below. For passive heating, the temperature in the disk will vary with distance r from the star as $T(r) \propto r^{-q_0}$, with $q_0 = 3/7$ (Chiang & Goldreich 1997). The luminosity of the young Sun is considered to vary with time as per Baraffe et al. (2002), leading to a drop in temperatures over the first few Myr while the disk is present. In a passively heated disk, the temperature profile is

$$T_{\rm pass}(r) = 171.4 \left(\frac{t}{1\,{\rm Myr}}\right)^{-1/7} \left(\frac{r}{1\,{\rm AU}}\right)^{-3/7} {\rm K}. \tag{3.1}$$

We also calculate the heating from viscous accretion using the results of the detailed

3D radiative transfer simulations of Min et al. (2011):

$$T_{\rm visc}(r) = \left[\frac{27}{128}\,\frac{k}{\mu\sigma}\,\Sigma(r)^2\,\kappa\,\alpha(r)\,\Omega(r)\right]^{1/3}, \tag{3.2}$$

where k and σ are Boltzmann's constant and the Stefan-Boltzmann constant, $\mu = 2.33$ proton masses is the mean molecular weight, $\Sigma(r)$ is the surface density of gas, and $\Omega(r)$ is the Keplerian orbital frequency. We assume a uniform and temperature-independent opacity $\kappa = 5\,{\rm cm}^2\,{\rm g}^{-1}$, appropriate for a mix of metal and silicates (Semenov et al. 2003). Here the turbulence parameter $\alpha(r)$ is assumed to vary spatially according to the three cases described above. Note that it affects the temperature of the disk, in addition to affecting the gas and particle dynamics. To combine the effects of passive and active disk heating, we combine the two temperatures to get the total temperature, as follows:

$$T(r) = \left[T_{\rm visc}(r)^4 + T_{\rm pass}(r)^4\right]^{1/4}. \tag{3.3}$$

We neglect temeprature-dependent variations in κ at temperatures below the silicate vaporization temperature $\approx$ 1400 K. Above that temeprature the lack of opacity precludes a temperature gradient, so we assume a maximum midplane temperature of 1400 K.

Transport of Vapor

We consider water vapor to be a trace species in the bulk disk gas. We take the equations governing their evolution via advection and diffusion as follows (from Clarke & Pringle 1988, Gail 2001, Bockelee-Morvan et al. 2002; see Desch et al. 2017):

$$\frac{\partial \Sigma_{\rm vap}}{\partial t} = \frac{1}{2\pi r}\,\frac{\partial \dot{M}_{\rm vap}}{\partial r}, \tag{3.4}$$

where the mass flux of vapor is

$$\dot{M}_{\rm vap} = 2\pi r\,\Sigma\,\mathcal{D}_{\rm vap}\,\frac{\partial c}{\partial r}. \tag{3.5}$$

Here $\Sigma_{\rm vap}$ and Σ are the surface densities of vapor and bulk gas, $c = \Sigma_{\rm vap}/\Sigma$ is the concentration of the vapor, and $\mathcal{D}_{\rm vap}$ is the diffusivity of the vapor. This does not necessarily equal the turbulent viscosity of the gas, ν, but we take the ratio to be ${\rm Sc} = \nu/\mathcal{D}_{\rm vap} = 1$, where Sc is the Schmidt number. We use the donor cell method to convert mass flows from one grid zone to another. The outer boundary is reflecting. At the inner boundary, we calculate the mass flux using the zero-torque boundary condition, as described in Paper I; if it is outward, we multiply by the concentration c in the innermost zone to get the mass flux of vapor into the innermost zone.

Transport of Solids

Into this gaseous disk with vapor, we add small particles of 0.06 mm diameter, analogs to chondrules, which are round, millimeter-sized particles found in abundance in chondritic meteorites (Scott & Krot 2014; see their Table 1 for chondrule sizes). In addition to diffusion and advection, intermediate-sized solid particles also drift relative to the gas, usually inward, towards the star. This happens as a result of gas orbiting the star more slowly than the Keplerian orbital velocity $r\Omega$, by an amount $\eta\, r\Omega$, due to partial support by the pressure gradient force (usually outward). Typically $\eta \sim 10^{-3}$. Particles orbiting at the Keplerian velocity feel a headwind that robs them of angular momentum, causing them to spiral inward (e.g., Weidenschilling 1977). The rate at which particles drift inward depends on their Stokes number:

$$\mathrm{St} = \frac{\pi}{2}\,\frac{\rho_{\rm p} a_{\rm p}}{\Sigma}, \tag{3.6}$$

where $\rho_{\rm p}$ and $a_{\rm p}$ are the internal density and radius of particles. This can be recast in terms of the aerodynamic stopping time of particles, $t_{\rm stop}$:

$$\mathrm{St} = \frac{1}{\Omega t_{\rm stop}}. \tag{3.7}$$

In terms of the Stokes number, the drift velocity of particles with respect to the gas is

$$V_{\rm drift} = \frac{-{\rm St}^2\, V_{\rm g,r} - {\rm St}\, \eta\, r\Omega}{1 + {\rm St}^2}, \tag{3.8}$$

where $V_{\rm g,r}$ is the radial component of the gas velocity (Takeuchi & Lin 2002). This expression is valid in the Epstein regime, when $a_{\rm p} < \lambda$, where λ is the mean free path of gas molecules; this is typically a good assumption throughout much of a protoplanetary disk. At 1 AU, particles of radius $\sim$ 30 cm and St = 1 can drift inward on timescales as short as 50 years, but larger and smaller particles drift more slowly; chondrule-sized particles with radii 0.03 cm would typically take $10^5 - 10^6$ yr to drift inward (Weidenschilling 1977).

The diffusion rate of particles also depends on their Stokes numbers. Their diffusivity is

$$\mathcal{D}_{\rm p} = \frac{\mathcal{D}_{\rm gas}}{1 + {\rm St}^2}, \tag{3.9}$$

where we assume the diffusivity of the bulk gas, like the vapor, is equal to the turbulent viscosity, ν.

We apply the same boundary conditions on the flow of solids as we do on the flow of vapor.

Vaporization and Condensation

Because our motivation is to calculate the spatial variation in water-to-rock ratio, we track the following fluids independently: bulk disk gas; water vapor; ice-free or 'rocky' chondrules (made of silicates); 'icy' chondrules that carry the mass of ice on particles the size of chondrules; ice-free, 'rocky' asteroids (large silicate bodies too large to drift); and 'icy' asteroids that carry the mass of ice on large bodies. In reality, ice would coat the surfaces of rocky chondrules, slightly increasing their

radius; in practice we assume two populations of identical-size objects (chondrules or asteroids), one pure rock and the other pure ice. We initialize the disk with a uniform concentration of vapor $c = 10^{-4}$, a uniform abundance of rocky chondrules (with surface density $= 0.005 \times \Sigma$) and icy chondrules (also with surface density $= 0.005 \times \Sigma$), and no icy or rocky asteroids.

Ice in icy chondrules can convert to vapor if in a region warm enough. The rate at which this occurs depends on the local saturation water vapor pressure over ice, which is

$$P_{\rm eq}(T) = 0.1 \, \exp\left(28.868 - 6132.9/T\right) \, {\rm dyn\,cm^{-2}}, T > 169\,{\rm K} \tag{3.10}$$

from Marti & Mauersberger (1993), and

$$P_{\rm eq}(T) = 0.1 \, \exp\left(34.262 - 7044.0/T\right) \, {\rm dyn\,cm^{-2}}, T \leq 169\,{\rm K} \tag{3.11}$$

from Mauersberger & Krankowsky (2003). The equilibrium vapor pressure relates to the surface density of water vapor as

$$\Sigma_{\rm vap,eq} = (2\pi)^{1/2} \left(\frac{P_{\rm eq}}{c_{\rm H2O}^2} \right) H, \tag{3.12}$$

where $H = C/\Omega$ is the scale height of the disk, C the sound speed in the bulk gas, and $c_{\rm H2O}$ the sound speed in water vapor. If $\Sigma_{\rm vap,eq}$ exceeds the total amount of water in icy chondrules and gas at radius r, we assume that all of the water there is in vapor form; otherwise we assume $\Sigma_{\rm vap} = \Sigma_{\rm vap,eq}$ and assume the remaining water is in the form of water ice (in icy chondrules).

Particle Growth

To simulate the growth of particles into planetesimals, we assume a fraction of the chondrule population at each radius r is converted into asteroid bodies every timestep of the code. Specifically, asteroids are presumed to grow on a timescale $t_{\rm grow}$, so that

in a timestep dt the mass of chondrules is reduced by an amount $\Sigma_{\rm chon}(dt/t_{\rm grow})$, and the same mass is added to the mass of asteroids. We assume typically $t_{\rm grow} = 1$ Myr. We do not include detailed models of fragmentation or growth of these particles into larger bodies, rather assuming that a fraction of the mass grows per time interval into large bodies by growth mechanisms such as streaming instability or pebble accretion (Johanssen et al. 2008; Lambrechts & Johanssen 2014). We do not model the size of asteroids, since bodies of any size more than a few km would take $\gg 1$ Myr to radially drift (Weidenschilling 1977). We ignore migration of asteroids by other mechanisms (e.g., dynamical resonances or scatterings).

3.2.2 Turbulence Radial Profiles

We consider three different radial profiles for the turbulence parameter $\alpha(r)$ and examine the response of water vapor and ice to each profile. A major goal of this paper is to study the effect of these different profiles—not just the magnitude of α, but the variation of α with distance r from the star— on the distribution of water in the disk. The most consistent way to do this would be to adopt power law profiles $\alpha \propto r^{-a}$, with a carrying different slopes, but the value of α at the snow line remaining fixed. The problem with this approach is that the different values of α inside and outside the snow line also lead to different distributions of mass and $\Sigma(r)$ profiles. Because the temperature depends on accretional heating and therefore $\Sigma(r)$, the location of the snow line would also vary. A different approach would be to adopt the profiles of $\alpha(r)$ predicted from first principles by different theories. The problem with this approach is that first-principles approaches to deriving $\alpha(r)$ are not especially robust or predictive. They also would probably depend sensitively on inputs such as temperature, density, ionization levels, etc. Improvements in the models, or just differing input assumptions, are likely to lead to different $\alpha(r)$ profiles.

As a compromise, we consider three $\alpha(r)$ profiles that capture the flavor of different physical mechanisms. Case I considers a uniform value of α throughout the disk. Case II considers a disk subject to the MRI, with a dead zone and low α at intermediate radius, bracketed by larger α at other radii. Case III considers a disk subject to purely hydrodynamic instabilities yielding uniform α, augmented by enhances transport due to magnetic disk winds in the inner disk. Across the snow line region (typically at several AU), α is uniform in Case I, increasing with r in Case II, and decreasing with r in Case III. Below we present the three $\alpha(r)$ profiles used, and discussed their physical motivations and justifications.

Uniform α profile

The first profile we consider is the commonly considered case of a uniform value of α throughout the disk. The turbulent viscosity ν is then simply proportional to temperature and other calculable parameters: $\nu = \alpha CH$. Because the physical mechanism underlying angular momentum transport in protoplanetary disks has not been established, this remains a popular assumption. We therefore define "CASE I" as follows:

$$\alpha_{\rm I} = 3 \times 10^{-4} \quad (\text{all } r). \tag{3.13}$$

We also consider a range of globally uniform values α between 10^{-5} and 10^{-3}. This choice of α is motivated by the observations of protoplanetary disk evolution, but also by numerical simulations of hydrodynamic turbulence such as the VSI, and by the concentration of chondrules by turbulence (see §1.3). While continued simulations of VSI and other hydrodynamic instabilities may ultimately predict variations in α with position, at the current time a uniform α throughout the disk is not inconsistent with purely hydrodynamic turbulence.

MRI α profile

While the uniform α assumption is widely used and simple to implement, it is unlikely that a protoplanetary disk would have uniform α. This is certainly true if angular momentum transport is dominated by the MRI, as it only operates at full efficiency in regions that are sufficiently ionized. The cold, poorly-ionized midplane regions from inside 1 AU, out to beyond 10 AU ("dead zones") are unlikely to be very MRI-active; however, the regions close to the Sun may be MRI-active due to thermal ionization (Desch & Turner 2015), and the regions far from the Sun may be MRI-active due to cosmic-ray ionization. These effects alone introduce radial variations, as the innermost and outermost portions might have relatively high turbulence, which we arbtirarily take to be $\alpha \sim 10^{-3}$, but the dead zone regions would have lower α. In the dead zone regions, the low-density upper layers are likely to be ionized either to a uniform surface density $\Sigma_{\rm a} \sim 100\,{\rm g\,cm^{-2}}$ (Gammie 1996) or to radially-dependent surface densities $\Sigma_{\rm a} < 10\,{\rm g\,cm^{-2}}$ due to X-ray ionization (Lesniak & Desch 2012; Kalyaan et al. 2015). The vertically averaged value of α would be $\alpha_{\rm a}\Sigma_{\rm a}/\Sigma$, where $\alpha_{\rm a}$ is the value in the active layer. In general the variations in Σ and $\Sigma_{\rm a}$ with r are likely to lead to radial variations of $\alpha_{\rm a}$ within the active layer as well. Following Kalyaan et al. (2015) [Paper I], we consider a floor value $\alpha = 10^{-4}$ near 1 AU, rising with increasing r as a power-law profile to $\alpha = 10^{-3}$ at 30 AU, and rising with decreasing r as a power-law profile to $\alpha = 10^{-3}$ inside 0.3 AU.

The second α profile we consider ("CASE II"), motivated by studies of the mag-

netorotational instability (MRI), therefore is given by

$$\alpha_{\rm II}(r) = \begin{cases} 1 \times 10^{-3}, & r \leq 0.3\,{\rm AU} \\ 1 \times 10^{-4}\ (r/0.3\,{\rm AU})^{-2.718}, & 0.3\,{\rm AU} < r \leq 0.7\,{\rm AU} \\ 1 \times 10^{-4}, & 0.7\,{\rm AU} < r \leq 1.5\,{\rm AU} \\ 1 \times 10^{-4}\ (r/1.5\,{\rm AU})^{+0.769}, & 1.5\,{\rm AU} < r \leq 30\,{\rm AU} \\ 1 \times 10^{-3}, & 30\,{\rm AU} < r \end{cases} \tag{3.14}$$

We note that this profile is consistent with $\alpha \approx 3 \times 10^{-4}$ in on averaged sense. It equals 3×10^{-4} at 6.2 AU. At 3 AU, $\alpha = 1.7 \times 10^{-4}$.

Recent studies of the MRI in disks calls into question many of the assumptions that went into generating this profile. Flaherty et al. (2015, 2017) present evidence that $\alpha < 10^{-3}$ in the outer portions of disks, consistent with what we've assumed, but lower than the MRI is typically thought to produce. On the other hand, Bai (2015) has presented numerical simulations including non-ideal Hall effects that yield $\alpha \sim 10^{-4}$ at 5 AU if the rotation of the disk is aligned with the magnetic field, or $\alpha \sim 10^{-6}$ if anti-aligned. Despite these uncertainties, we feel our case II profile captures a key attribute of the MRI, which is that it should be less active in dead zone regions, with α increasing in magnitude with increasing r beyond the dead zone.

Hybrid α profile

At the current time, models invoking hydrodynamic instabilities such as VSI, would predict a low level of turbulence acting throughout this disk, with $\alpha \sim 10^{-4}$; these models are not developed to the point that radial variations can be strongly argued for. A disk evolving purely by non-magnetic, hydrodynamic instabilities such as the VSI is probably represented well by a uniform α disk as in our Case I profile. Disks evolving by magnetic instabilities such as the MRI are probably characterized by our Case II profile. The third example we consider is a disk that is evolving primarily by

hydrodynamic instabilities such as VSI, but augmented by magnetically controlled angular momentum transport, not through the MRI but through disk winds.

For example, Simon et al. (2018) explain the low levels of turbulence measured by Flaherty et al. (2015, 2017) in the outer portions of some disks, by invoking attenuation of cosmic rays by strong winds. These winds, in turn, would be generated by magnetocentrifugal outflows relying on large-scale magnetic fields. Suzuki et al. (2016) have recently performed global numerial simulations of disk winds, considering the global energy budget of a protoplanetary disk. Suzuki et al. (2016) find that the disk winds launched by the outflows would induce a torque in the disk characterized by $\alpha_{\phi,z} \sim 10^{-4}$. This is not the same as the traditional α parameter, which relates directly to the $\alpha_{r,\phi}$ component of the Reynolds or Maxwell stresses, but it plays a similar role in that the disk wind would drive angular momentum transport, lead to heating (by ambipolar diffusion) and the Reynolds stress could help particles diffuse. Other simulations find a role for the MRI in the upper layers of the disk in driving the disk winds. Simulations by Bai et al. (2015) find $\alpha \sim 10^{-6} - 10^{-4}$ at 5 - 15 AU, depending on whether the magnetic field is aligned or anti-aligned with the disk's rotation.

These results suggest a hybrid model in which the disk overall is characterized by low levels of $\alpha \sim 10^{-5}$ throughout, except in the inner disk, where $\alpha > 10^{-4}$ may obtain due to magnetic disk winds, possibly in concert with the MRI. Such a profile was recently considered by Desch et al. (2018) in their disk evolution model to explain the abundances of CAIs (calcium-rich, aluminum-rich inclusions) and refractory elements in different meteorite types. This model demands a low level of $\alpha \sim 10^{-5}$ in the outer disk (> 10 AU) to prevent mixing of gas with the inner disk, which is depleted in refractory elements; higher values of α would not allow CI chondrites to chemically match the solar photosphere. The model also demands a higher value of α

in the inner disk (< 1 AU), up to 5×10^{-4}, so that CAIs will be efficiently transported outward in the disk; lower values of α would not lead to efficient transport of CAIs to the carbonaceous chondrite-forming region, but higher values of α would drain the inner disk of material before ordinary and enstatite chondrites could form.

Based in part on the success of the Desch et al. (2018) model, and in part on the physical plausibility of VSI augmented by disk winds, the third α profile we consider ("CASE III") is given by

$$\alpha_{\rm III}(r) = \begin{cases} 1 \times 10^{-3}, & r \leq 1\,{\rm AU} \\ 1 \times 10^{-3}\ (r/1\,{\rm AU})^{-1}, & 1\,{\rm AU} < r \leq 10\,{\rm AU} \\ 1 \times 10^{-4}, & 10\,{\rm AU} < r \end{cases} \tag{3.15}$$

We note that like the case II profile, the typical value of α in the case III profile is $\approx 3 \times 10^{-4}$, in an average sense, and equals that value at 3 AU.

3.3 Results

In this work, we carry out a suite of simulations of an evolving disk with volatile transport under different prescriptions of turbulence. We explore a range of globally uniform α values as well as radially varying α profiles that are motivated by different mechanisms of angular momentum transport. The results of these simulations are complex, since α affects mass flows, temperatures, and particle diffusion simultaneously and in different ways. Therefore we also perform a set of simulations in which we only change one parameter at a time, to tease out important trends while keeping the other parameters constant. First, we discuss our canonical uniform-α disk in detail. We then vary some parameters (namely, size of the drifting particle, diffusivity of vapor and small solid particles, opacity κ of the disk gas, and the timescale of growth of asteroids) that regulate the behaviors of either particles, vapor or the general disk. After that, we explore volatile transport in disks with different global uniform α and

with radially varying α profiles.

3.3.1 Canonical Uniform-α case

We first present in Figure 28 the results of our canonical case of the uniform α disk, with $\alpha = 3 \times 10^{-4}$ at all radii r. Water content in the disk is depicted in three different forms. Figure 28a shows the radial distribution of the total H_2O abundance of water in both ice and vapor, i.e., sum of $\Sigma_{\rm vap}$ and the surface density of ice in solids (chondrules + asteroids), relative to the gas surface density Σ, at all r and at times ranging from t = 20 kyr to 5 Myr. The location of the snow line is evident as the radius near 2 AU at which this quantity changes abruptly at every timestep. The gray shaded region shows radii always inside the snow line, at which H_2O is present only as vapor throughout the course of our simulation, up to 5 Myr. The darker blue region shows radii always beyond the snow line, for which H_2O is present only as ice, from $t = 20$ kyr to 5 Myr. The light blue region between them denotes regions that start with H_2O as vapor, but later see H_2O only as solid ice as the snow line moves inward as accretional heating diminishes. Figure 28b shows the fraction of the mass in small particles that is ice, at different radii r and times t. Far out in the disk, the particles assume cosmic abundances and are assumed to be 50% ice and 50% rock. Inside the snow line, no ice exists in small particles. Just beyond the snow line, water can be cold-trapped on small particles, which see an enhancement in the ice fraction above cosmic abundances. These small particles are subject to rapid radial drift and are also the precursor materials for asteroidal bodies that grow directly from them, e.g., by streaming instability. Asteroidal material at a given location is assumed to capture at any time in the disk a fraction of the rocky chondrule mass and the icy chondrule mass at each location. These asteroids are assumed not to radially migrate after that. Figure 28c shows the fraction of asteroidal material at various radii r and

times that is ice. Note that the radial scale is linear, not logarithmic as in Figures 28a and 28b. At early times, asteroid material has cosmic abundances of water (50% ice fraction) outside the snow line at about 5 AU, and no ice inside that. As the snow line moves inward, more asteroidal material between 3 and 5 AU can acquire water ice.

Figure 28 illustrates several processes shaping the distribution of volatiles across the snow line and throughout the disk. The concentration of vapor in the inner disk decreases with time as it either diffuses onto the star, or is back-diffused through the snow line to be deposited as ice on solids. Chondrules diffuse across the snow line as well, either diffusing inward as icy chondrules or outward as rocky chondrules. Ice tends to vaporize, and water vapor tends to condense, over a narrow radial range. Diffusion of chondrules does not change the chondrule abundance, as the outward and inward diffusive fluxes of chondrules are equal; it also does not directly affect the water, as only dry chondrules can diffuse outward, and icy chondrules drifting or diffusing inward tend to lose their ice over a very narrow range of radii, $\Delta r \approx 0.01 - 0.02$ AU. The dominant process affecting the distribution of water at the snow line is the diffusion of water vapor outward past the snow line, which then freezes and accumulates over time just beyond the snow line. This increases the water-ice fraction in chondrules from an initial assumed 50wt% to a peak abundance of 80wt% just beyond 2.0 AU at 5 Myr (Figure 28b). This translates into an increase in the water-ice fraction of asteroids at the radii that are at various times beyond the snow line (Figure 28c). As the snow line moves inward and chondrules and the ice distribution move inward, the asteroids that form in their wake remain in place.

To facilitate comparisons to this canonical case, in Figure 29 we present the timescales of different transport mechanisms in the disk, defined as $2\pi r\,\Sigma/(\partial \dot{M}/\partial r)$, where Σ and $\dot{M}$ refer to the relevant fluid (chondrules, or H_2O, etc.). Throughout

much of the disk, the diffusion of chondrules and vapor are equally rapid and the most rapid processes in the disk, with typical timescales $\sim 10^5$ yr. Chondrule drift is almost as rapid, with associated timescales $\sim 3 \times 10^5$ yr.

3.3.2 Parameter Study of a Uniform-α Disk

We perform a parameter study, taking key parameters in our canonical disk model and varying them one by one, to assess their influence on the water distribution across the disk. The canonical disk assumes $\alpha = 3 \times 10^{-4}$, and results are compared to this case. We performed simulations for a range of chondrule sizes, Schmidt number, timescale for growth of asteroids, and opacity of disk material. The results of this parameter study are in presented in Figures 30, 31, 32, 33 and 34, and are discussed in detail below.

Effect of varying chondrule size

In this study, the chondrule radius was varied from 0.01 cm, to 0.03 cm (our canonical case), to 0.06 cm, to explore the changes in water distribution due to different chondrule sizes. Increasing the chondrule radius has a dramatic effect on the water distribution, as seen in Figure 30. With increasing chondrule size, the ice fraction of chondrules just beyond the snow line increases greatly; at 5 Myr it is 60wt% for $a = 0.01$ cm, 80wt% for $a = 0.03$ cm, and nearly 100wt% for $a = 0.06$ cm. We attribute this to a change in the relative rates of diffusion and drift. The diffusion rate of particles can vary with particle size through the Stokes number (Equation 3.9), but in the limit St $\ll 1$, appropriate for chondrules, the diffusivity does not appreciably vary with particle size. The drift rate, on the other hand, is proportional to St and therefore particle size. Larger chondrules diffuse as quickly as small chondrules, but large chondrules drift more rapidly; for the large chondrules the drift

rates approach the diffusion rates. Whatever water vapor diffuses outward across the snow line is more rapidly brought back across the snow line into the inner disk; but, simultaneously, drift from the outermost portions of the disk is more rapid, and more water overall is brought to the snow line. This has the additional effect of limiting the depletion of water vapor from the inner disk inside the snow line. While the inner disk content steadily is more depleted over time in the case with $a = 0.01$ cm, the case with $a = 0.03$ cm has roughly constant water vapor in the inner disk for about 0.5 Myr, implying the inner disk is temporarily 'flooded' with H_2O. For the case with $a = 0.06$ cm, the vapor abundance is enhanced for 1 Myr before rapidly depleting. Because α is the same in all three cases, the snow line is at the same location for all three cases.

Effect of varying particle diffusivity

To more closely examine the importance of changing the diffusivity vs. drift of particles, we explored a range of Schmidt number, from Sc = 0.3, to 1 (our canonical case), to 3. The particle diffusivity is $\mathcal{D}_{\rm p} = \nu/{\rm Sc}$, so higher Schmidt number yields lower particle diffusivity, but does not affect the drift rate or evolution of the disk. Results are plotted in Figure 31. The cases with Sc = 3 have the lowest diffusivity and therefore the highest relative rate of particle drift to particle diffusion. As in the case with $a = 0.06$ cm, which also had a high relative rate of drift to particle diffusion, this leads to a higher ice fraction of chondrules beyond the snow line. Comparing the different Schmidt number cases, those with the highest Sc are marked by the narrowest radial extent of enhanced chondrule ice fraction, and those with the lowest Sc have the broadest radial extent of high water fraction. This is understood in terms of icy chondrules diffusing further 'upstream' beyond the snow line, widening the distribution, when Sc is low and their diffusivity high. The water vapor abundance in

the inner disk is also slightly lower for low Schmidt number, as chondrules can diffuse back across the snow line more rapidly, and can more effectively capture water vapor beyond the snow line.

Effect of varying asteroid growth timescale

We explored the effect of varying the timescale $t_{\rm grow}$ over which chondrules are converted into larger, asteroid-sized bodies. Asteroids are assumed to grow my converting a fraction of the mass (both silicate and ice) present at a given radius into large bodies that from that point on are immovable. Beside our canonical case of $t_{\rm grow} = 1$ Myr, we consider $t_{\rm grow} = 0.3$ Myr, basically assuming that planetesimals form three times faster than in our canonical case. The results are plotted in Figure 32. Comparing the $t_{\rm growth} = 0.3$ Myr case to our canonical case, chondrules are more efficiently converted into asteroids before they can drift or diffuse. This significantly reduces $\Sigma_{\rm chon}$, both inside and outside the snow line. A dip in the water vapor abundance just inside the snow line (Figure 32a) reveals that inward transport of ice (through diffusion and also drift) is not fast enough to replenish water vapor, which continues to diffuse outward across the snow line. At the same time, chondrules do not remove ice from beyond the snow line as rapidly. This results in an enhanced ice-to-rock ratio beyond the snow line. These effects transport water outward so effectively, the snow line is mover slightly outward.

Effect of varying the opacity

We explored the effect of varying the opacity of the gas (due to dust), from $\kappa = 4\,{\rm cm^2\,g^{-1}}$, to $\kappa = 5\,{\rm cm^2\,g^{-1}}$ (our canonical case), to $\kappa = 6\,{\rm cm^2\,g^{-1}}$, to $\kappa = 8\,{\rm cm^2\,g^{-1}}$. Increased opacity leads to higher disk temperatures in actively accreting disks. Far from the star, the disk temperature conforms to the passively heated disk limit,

but the snow line location is usually located where accretion has increased the disk temperature above the passively heated disk case. Therefore higher opacities can increase disk temperatures and move the snow line outward. Figure 33 plots the effects on the radial distribution of water, which turn out to be minimal. The location of the snow line hardly moves. As Equation 3.2 demonstrates, the temperature in the disk varies as $\kappa^{1/3}$. As the temperatures around the snow line tend to fall as r^{-1}, the location of the snow line tends to vary as $r_{\rm snow} \propto \kappa^{-1/3}$. Across the entire range of opacities we considered, the location of the snow line varies by only 25%, from about 2 AU to 2.5 AU.

Increases in global disk temperatures slightly increase the turbulent viscosity, since $\nu = \alpha CH = \alpha(kT/\bar{m})/\Omega$. This does not change the viscosity of gas or diffusivity of particles at the snow line, which is at more-or-less fixed temperature $\approx$ 160 K. The diffusion and drift of vapor and particles across the snow line would not differ from the canonical case. But global increases in temperature and ν would decrease the disk evolution timescale $\propto r^2/\nu$, making the disk evolve slightly faster ($\approx$ 25%). At any instant in time this would lead to greater ice-to-rock ratios of chondrules beyond the snow line. Overall the radial distribution of water ice is little changed.

Summary

The cases considered above show the effects of varying chondrule size and Schmidt number, as well as asteroid growth timescale and opacity. Disk opacity is found to have little effect on the radial distribution of water, and especially the final water content of asteroids. One of the most important parameters affecting the distribution of water is the timescale on which chondrules are converted into asteroids. For shorter timescales $t$growth, chondrules are more depleted from beyond the snow line and can carry less water inward across the snow line by drift. This enhances the water-to-

rock ratio. The other two parameters are of moderate importance, and highlight the subtle interplay between drift and diffusion of vapor and particles. We plot in Figure 34 the timescales of chondrule drift and diffusion and vapor diffusion in these different model disks. As previously seen, the cases where particle drift timescales are shorter than the chondrule diffusion and vapor diffusion timescales in the 1-10 AU region are the cases that lead to the highest water-to-rock ratios beyond the snow line. This is somewhat unexpected, as faster-drifting chondrules might be expected to carry ice out of this region, into the inner disk, faster than water vapor could diffuse back across the snow line. We attribute the enhancement in water-to-rock ratio to an overall increase in the water being brought to the snow line region from far out in the disk by drifting chondrules.

3.3.3 Effect of changing the global, uniform α

Having examined the roles of different physical processes in the disk, we next explore the effect of varying the uniform value of α across the disk, considering cases ranging from $\alpha = 3 \times 10^{-5}$, to $\alpha = 1 \times 10^{-4}$, to $\alpha = 3 \times 10^{-4}$ (our canonical case), to $\alpha = 3 \times 10^{-3}$. The results are plotted in Figure 35. With increasing values of α, the inner disk within the snow line is increasingly depleted in water vapor. At 5 Myr, the water abundance declines from 4.5×10^{-3} for $\alpha = 3 \times 10^{-5}$, to $\ll 10^{-4}$ for $\alpha = 1 \times 10^{-3}$. As α is increased, water vapor back-diffuses outward across the snow line more quickly, but water ice on particles also diffuses inward more quickly. Increasing α also would increase the inward velocity of gas, $V_{g,r}$, but from Equation 3.9, as long as St $\ll 1$, the drift speed of chondrules is little affected by changes in α. Therefore increasing α increases the relative importance of particle diffusion to drift. This conclusion is supported by Figure 36, which shows that drift is more rapid at low values of α, but for high values of α diffusion is more rapid than drift. At higher α,

icy chondrules beyond the snow line are better able to diffuse outward, giving them more opportunity to be incorporated into asteroidal material. For all values of α, there is a zone beyond the snow line in which the ice-to-rock fraction is increased. As α increases, the width of that zone increases, but the peak ice-to-rock concentration decreases. This trend is somewhat echoed in the plots of asteroid water-ice fraction plots (third column of Figure 35). Higher values of α yield a broader range of radii over which asteroid water fractions increase from 0wt% to 50wt%. Smaller values of α allow for slightly higher water-ice fractions, but the effect is muted. In summary, higher values of α yield higher accumulations of ice beyond the snow line, but do not yield the highest peak abundances of water ice beyond the snow line, as the water content beyond the snow line is distributed over a broader radial region.

3.3.4 Water distribution with an MRI α profile

Case I examines the distribution of water in a disk with uniform $\alpha = 3 \times 10^{-4}$. Case II, presented in Figure 37, shows the distribution of water in a disk subject to turbulent viscosity like that driven by the MRI. An immediate result is that the ice-to-rock fraction of chondrules beyond the snow line is much higher than in Case I, with an ice fraction of 0.97. The difference in α at the snow line is not large, less than a factor of 2. Larger differences in α than this did not lead to such large differences in water content (§3.3). We attribute the increased water-ice fraction to several factors. One is the surface density, $\Sigma(r)$, which we plot in Figure 38. The effect on the temperature is seen in Figure 14, and the timescales for diffusion and drift are plotted in Figure 40. As seen in Figure 38, by as early as 0.5 Myr, the surface density at 2 AU is almost a factor of 4 larger in Case II than in Case I. This is due to α being lower in this region than surrounding regions in Case II, causing mass to pile up in this same region where the snow line is located. The lower values

of α in this region also lead to vapor and chondrules diffusing less rapidly there, but more rapidly in the surrounding regions. At the same time, the higher densities lead to lower Stokes numbers, which leads to smaller drift speeds. All of these factors combine to bring water ice or vapor to the snow line region, but to inhibit its escape from the snow line region.

3.3.5 Water distribution with the hybrid α profile

Case III, presented in Figure 41, shows the distribution of water in a disk subject to turbulent viscosity like that driven by VSI plus disk winds in the inner disk. An important difference between this case and the others is that the surface density $\Sigma(r)$ is flat and significantly lower than the other cases, with $\Sigma(r) \approx 500\,\mathrm{g\,cm^{-2}}$ throughout the snow line region by 0.5 Myr (Figure 38). The higher values of α in the inner disk keep temperatures in the inner disk hotter than in Cases I and II, and allows the inner disk to evolve and lose mass more rapidly. Compared to the other cases, initially the temperatures are higher in the inner disk due to the higher α, but then as surface densities decrease, the temperatures drop more precipitously and the snow line moves in rapidly. Between 0.02 and 5 Myr the snow line moves in from 5 AU to 1 AU as temperatures drop (Figure 39) Rapid inward drift of the snow line keeps the peak abundance at about the same level throughout the simulation from 1 - 5 AU. This results in a large "transition" region in the asteroid water-ice fraction (Figure 39c) between the water ice solid material beyond 5 AU to water-depleted inner disk within the snow line. The vapor content is seen to deplete to around the same levels in the inner disk as the uniform α case.

3.3.6 Convergence tests

We also performed convergence tests to ensure that our simulations returned similar results with increase in our grid resolution. We performed the same simulation with 200, 300 and 400 zones, and found that with higher resolution, the peak water-to-rock ratio beyond the snow line dropped by less than 4%, and that none of our results or conclusions is significantly changed. We find no other significant variation due to increase in resolution (Figure 42).

3.4 Discussion

3.4.1 Sensitivity Analysis

In our parameter study of uniform-α cases, we considered the effects of several parameters on the distribution of water ice in the disk and in planetesimals that would eventually form planets. These included chondrule size, Schmidt number, the growth timescale of asteroids, the opacity, and the value of α. Our sensitivity analysis allowed us to identify which of these factors had the biggest impact on the distribution of water ice, both in chondrules and in the planetesimals formed from them.

Parameters affecting water distribution in the disk

We find that for variations across the likely range of each input, the size of particles, i.e., chondrule radius a, had the largest effect on the water-ice fraction in chondrules (Figure 30). In our canonical case with $a = 0.03$ cm, the water ice fraction in asteroids just beyond the snow line at 5 Myr slightly exceeded 80%. For smaller particles, $a = 0.01$ cm, the fraction barely exceeded 60%, while for slightly larger particles, $a = 0.06$ cm, the ice fraction approached 100%. Changing the size of small particles onto which water vapor can condense as ice, by factors of just 2 to 3, led

to very large changes in the ice-to-rock ratio on chondrules. The cases with larger chondrules also saw the water-ice fraction reach elevated levels at far greater radii beyond the snow line,

The next most important parameter is the growth timescale of asteroids $t_{\rm grow}$ (Figure 32). For our canonical case with $t_{\rm grow} = 1$ Myr, the water-ice fraction is $\approx 80\%$ beyond the snow line at 5 AU. For a faster conversion rate of chondrules into planetesimals, $t_{\rm grow} = 0.3$ Myr, the water-ice fraction approaches 100%. Far fewer chondrules are available for the water ice to adhere to, leading to higher water-ice fractions. The width of the water-ice region beyond the snow line is slightly larger as well.

Variations in the value of α were important but not as prominent as the changes in the above parameters (Figure 35). The water-ice fraction beyond the snow line at 5 Myr is $\approx 80\%$ in our canonical case with $\alpha = 3 \times 10^{-4}$. For lower values of $\alpha = 3 \times 10^{-5}$ this fraction approaches 90%, while for larger values of $\alpha = 1 \times 10^{-3}$ it is 75%.

Variations in the diffusivity of small particles, via the Schmidt number Sc, led to notable but smaller changes in the water-ice fraction in chondrules (Figure 31). Beyond the snow line at 5 AU, the water-ice fraction is $\approx 80\%$ in our canonical case with Sc = 1, dropping slightly to 75% for Sc = 0.3, and rising to 90% for Sc = 3. The width of the enhanced water-ice region is more strongly affected by the particle diffusivity, reaching to much greater radii for greater diffusivity (lower Sc).

Surprisingly, changes in the value of the opacity, κ, had the smallest effect on the distribution of water ice in the disk. The cases with $\kappa = 4\,{\rm cm^2\,g^{-1}}$ and $\kappa = 8\,{\rm cm^2\,g^{-1}}$ showed almost no difference in peak water-ice content or distribution of water ice beyond the snow line, compared to our canonical case with $\kappa = 5\,{\rm cm^2\,g^{-1}}$. Opacity sets the temperature in the disk and the location of the snow line, but it is not a large

effect. From Equation 3.2, the temperature in actively accreting disks is $T \propto \kappa^{1/3}$, and from Figure 40 temperature also is dropping roughly as $T \propto r^{-1}$ in the snow line region, meaning that the location of the snow line varies roughly as $\kappa^{1/3}$, being only tens of percent closer in or farther out across this range of opacity. More importantly, the distribution of ice and vapor is little affected by these changes.

We conclude that "planetary" parameters like the radius of small particles (chondrules) or the rate at which they are converted into planetesimals, dominate the distribution of water ice in the disk, and not such "disk" parameters like α or opacity κ.

Parameters affecting distribution of water ice in planetesimals

The distribution of water ice in a disk translates into water content of planets only by affecting the water content of asteroidal planetesimals, which are the building blocks of planets. Planetesimals, we assume, grow continuously over the lifetime of the disk, converting small chondrules into large asteroids with an e-folding time of $t_{\rm grow}$. Because asteroids grow over a long timescale, instantaneous distributions of water ice in the disk are averaged out. Most of the cases considered above lead to similar distributions of water ice in planetesimals. Peak water-ice contents rarely exceed 50%, sometimes approaching 60%. Beyond the snow line, almost all planetesimals in all cases have $\approx 50\%$ ice. The quantity that is strongly affected is the radial distribution of asteroids with intermediate water ice content $< 50\%$.

In our canonical case, that distribution at Myr extends from about 2.5 AU, where water ice contents are barely above 0%, to about 5 AU, where they approach 50%. Most parameters have little effect on this distribution: this same pattern is observed across the range we consider for chondrule size a, Schmidt number Sc, asteroid growth timescale $t_{\rm grow}$, and opacity κ (Figures 30, 31, 32, and 33).

The radial distribution of asteroid water-ice content seems most affected by α (Figure 35). The largest values of $\alpha \sim 10^{-3}$ allow the disk to evolve more rapidly; asteroids less reflect a snapshot of the disk and more reflect an average over time. The peak water ice concentrations do not exveed 50% anywhere. For the smallest values of $\alpha = 3 \times 10^{-5}$, the asteroids beyond the snow line can reach 60% ice, with a drop-off beyond that. To a lesser extent, the asteroid growth timescale matters, with $t_{\rm growth} = 0.3$ Myr yielding asteroids beyond the snow line with $> 55\%$ water ice. The existence of a local maximum in the asteroid water ice content appears sensitive to the timescale of planetesimal formation ($t_{\rm growth}$) relative to the disk evolution timescale ($\sim r^2/\nu \propto \alpha^{-1}$). Faster asteroid growth and/or slower disk evolution allows a local maximum.

We conclude that water ice content of planetary materials is affected equally by "disk" parameters (α) and "planetary" parameters ($t_{\rm growth}$).

The sensitivity of the water ice distribution in the protoplanetary disk to various input parameters can be understood largely in terms of the relative rates of diffusion and drift. As seen in Figures 29, 34, and 41, in general diffusive transport of vapor and chondrules is faster than drift of chondrules, by almost an order of magnitude throughout much of the disk in most of the presented simulations. In the common situation where drift is much slower than diffusion, the water ice content just beyond the snow line is close to the cosmic abundance of water ice, with a water-ice fraction of 50%. But as the rate of drift in is comparable to, or faster than, the rate of diffusion, then the water-ice fraction in solids beyond the snow line can be become quite large.

3.4.2 Physical processes affecting water distribution

The radial distribution of water ice in chondrules beyond the snow line can be understood in part as a relative rate of particle drift vs. diffusion of particles and

vapor.

For example, Figure 35 shows that the peak water-ice fraction is higher at 5 Myr ($\approx 90\%$) for the case with $\alpha = 3 \times 10^{-5}$ than it is ($\approx 75\%$) at 5 Myr in the disk with $\alpha = 1 \times 10^{-3}$. This is not due to temporal differences: these water-ice enhancements occur late in disk evolution, so if anything the disk with higher α should develop the same water-ice enhancements at earlier times. (The evolution timescale scales as $r^2/\nu \propto \alpha^{-1}$)

It is also not due to a relatively higher general rates of diffusion. Disks with large α should cause water vapor to diffuse outward past the snow line faster, leading to greater enhancements; or, including the inward diffusion of icy chondrules through the snow line, one might expect the two effects to cancel each other out, leading to no differences. Figure 36 demonstrates that the diffusion timescales of vapor and particles at the snow line vary from ~ 2 Myr for $\alpha = 3 \times 10^{-5}$, to ~ 0.02 Myr for $\alpha = 1 \times 10^{-3}$, without a significant change in the water-ice fraction beyond the snow line.

A change in just the diffusion rate of particles but not vapor leads to somewhat larger changes. Figure 34 demonstrates that as the diffusion rate of particles alone is varied by an order of magnitude, as Sc is varied from 0.3 to 3, the water-ice fraction does change, but only from about 75% to 90%. With increased Sc, particle diffusivity decreases, meaning that icy chondrules diffuse inward more slowly, leading to a lower loss of icy from the region beyond the snow line. Particle diffusion is not the dominant loss mechanism, however.

Rather, the dominant effect appears to be particle drift, and factors affecting drift rates appear to be the main determinant of the water-ice distribution. Figure 34 shows that as chondrule radii are increased from 0.01 cm to 0.06 cm, there is very little change in the diffusion timescale. This is because $\mathcal{D} = \nu\,(1+\mathrm{St}^2)^{-1}$, and $\mathrm{St} \ll 1$

for chondrules of all these sizes. The drift rate changes considerably, though, as the drift velocity is proportional to St and therefore a/Σ. The large chondrules drift 6 times faster than the small chondrules, and the drift timescales reflect this. Larger drift rates might be expected to more quickly drain icy chondrules out of the region beyond the snow line, lowering the water-ice fraction there, opposite to the observed trend ; but a more important factor is the influx of ice to this region from farther locales in the disk. The drift velocity of particles is $V_{\rm drift} \propto {\rm St}\eta V_{\rm K} \propto \eta V_{\rm K}(a/\Sigma)$. The mass flux of particles is therefore $\Sigma V_{\rm drift} \propto \eta V_{\rm K} a$. The influx of icy particles into the region beyond the snow line therefore is 6 times larger for the 0.06 cm radius chondrules than for the 0.01-cm radius chondrules. This ice ultimately vaporizes inside the snow line, but as long as as significant fraction is returned to beyond the snow line, the water-ice fraction there will ultimately be higher.

A re-examination of Figures 35 and 36 suggests that the cause of the increased water-ice fraction in cases with low α is primarily due to differences in drift rate. Because disks with low α evolve more slowly, they maintain high surface densities for longer. Higher Σ leads to slower drift rates. Indeed, the cases with low α have the longest drift timescales, and and the cases with highest α have the shortest drift timescales. The short drift timescales lead to more overall water ice beyond the snow line for the high-α cases, as seen in the first column of Figure 35. The high α additionally has the effect of broadening and lessening the peak water-ice fraction.

These overall trends help explain why factors like the disk opacity have little effect on the water-ice content. Changes in opacity have a relatively minor effect on the temperature, which is proportional to $\kappa^{1/3}$. Factor of 2 increases in κ have a minor effect on the disk viscosity, increasing it only by a factor of 1.26. This would affect the diffusion of both particles and vapor, which would not directly change the distribution of ice much. The surface density at any time would be slightly decreased

by the higher viscosity, leading to higher drift of particles that slightly increases the water-ice fraction. But because the effects are indirect, the change in the water-ice fraction is small.

Ultimately, the water-ice content of small solids beyond the snow line is set by subtle interplays between viscosity, diffusion, and drift, with factors affecting drift playing the most important role.

3.4.3 Effects of changing $\alpha(r)$

With these insights, we can begin to understand the water distributions in our three different $\alpha(r)$ profiles. Changing $\alpha(r)$ in the disk, either by varying a globally uniform value, or by adopting a radially varying $\alpha(r)$ profile, changes the distribution of ice by altering the diffusion rates of particles and vapor, and by changing the drift rates of particles.

Figure 41 shows that Case III, with the hybrid $\alpha(r)$ profile due to hydrodynamic instabilities and and magnetic disk winds, and Case I, have the highest overall amounts of water beyond the snow line, with water fractions reaching 4 times the overall disk mass fraction of 5×10^{-3}. Case II has water abundances approaching these levels, 3 times the background levels, but over a narrower range of radii. These trends are mostly attributable

Figure 37 shows that Case II, with the $\alpha(r)$ profile resembling that due to the MRI, has the highest local concentrations of water-ice beyond the snow line. Some regions show water-ice fractions of solids $> 95\%$, in contrast to the peak water-ice fractions $\approx 60\%$ in Case III. Case I with uniform α has intermediate peak values at 5 Myr of $\approx 80\%$. Since all three cases have similar overall water contents, we attribute these effects largely to the different values of α at the snow line, which tends to smear out and decrease the peak distributions. At 5 Myr, the value of α at the snow line

is only 1.7×10^{-4} in Case II, allowing for sharp distributions. At the snow line at 5 Myr, $\alpha = 3 \times 10^{-4}$ in Case I, and is as large as 8×10^{-4} in Case III.

The different cases yield different positions of the snow line over time. In Case I, the snow line starts at about 4.5 AU and moves in to about 2 AU by 5 Myr. In Case II, the snow line starts at about 5 AU and moves in to 3 AU, and for Case III it moves in from 5 AU to about 1.2 AU by 5 Myr. Case III shows the snow line moving in the most because the higher values of α at small radii deplete the inner disk of gas the fastest, leading to decreased accretional heating.

An important side effect of the snow line moving in so much more in Case III is that it leads to a greater diversity of asteroid water-ice fractions in the inner disk. In Case III, asteroids forming at 2.5 AU between 0.5 Myr and 5 Myr might have anywhere from 0% to 50% ice, with similar ranges seen for asteroids forming anywhere between 2 and 4 AU. In contrast, in Case II, asteroid water content only varies in a relatively narrower range of radii, from 3 to 4 AU. Case I, with uniform α, is somewhat intermediate between these cases, with asteroids showing variable water content between 2.5 and 3.5 AU. These results in particular suggest ways to use the water distributions of asteroids to probe the $\alpha(r)$ profile of the solar nebula.

3.4.4 Observational Tests

Astronomical Observations of Disks

Our work highlights the connections between different $\alpha(r)$ profiles and the distribution of water vapor in the inner disk or water-ice on chondrules or in asteroids in the outer disk. It is not currently possible to directly measure $\alpha(r)$ in protoplanetary disks, although some observations may constrain this parameter. High-resolution imaging of disk regions by Pinte et al. (2016) show that the sharpness of the gaps

and rings in the outer portions of many protoplanetary disks requires low $\alpha < 10^{-4}$ more compatible with Cases I or III, but not with Case II. Higher resolution imaging potentially could similarly constrain α in the inner disk in the future, but this would be an observational challenge. Novel tests with sophisticated chemical models to detect heating from viscous accretion, such as detecting molecular emission in the cooler (90-400 K) layers of the disk, as put forth by Najita & Adamkovics (2017), or detect distinct chemical imprints that betray either a spatial variation in turbulence or a difference between low- and high-viscosity disks may also constrain $\alpha(r)$.

It would advantageous to use observations of water vapor in the inner portions of disks to constrain α there. Differences in water vapor abundance take time to develop, but by 5 Myr, in our Case I uniform-α disk, with $\alpha = 3 \times 10^{-4}$ in the inner disk, the water vapor mass fraction is 1×10^{-4}. For case II, $\alpha = 1 \times 10^{-3}$ in the inner disk and the water vapor mass fraction is 4×10^{-4}. And in Case III, $\alpha = 1 \times 10^{-3}$ throughout a broader region in the inner disk, and the water vapor abundance is 2×10^{-4}. The relationship between α and water vapor abundance is therefore complicated, but forward models with $\alpha(r)$ as an input should be able to test models against observations. A particular feature of our Case II disk that might be observable is the dip in water abundance by a factor of almost 2 just inside the snow line, between 2 and 3 AU.

Solar System Observations

Our results suggest it may be possible to use the spatial distribution of asteroid water content to constrain the $\alpha(r)$ profile of the solar nebula disk. The water content of asteroids is discernible using spectroscopy and comparison to meteorites.

Gradie & Tedesco (1982) determined that different classes of asteroids are predominantly present in specific locations of the asteroid belt; S-type asteroids dominate

in mass and number in the inner belt inside about 2.7 AU, while C-type asteroids dominate in mass and number in the outer belt beyond about 2.7 AU (see Fig. 3 of DeMeo & Carry 2014; the largest asteroids correspond to all the mass above the horizontal dotted line at $\sim 1 \times 10^{18}$ kg).

S-type asteroids show little evidence of hydration features in their spectra, and are spectrally associated with ordinary chondrites, which are generally water-poor, with only $0.1 - 1$ wt% water (Hutchison et al. 1987; Alexander et al. 1989, 2013). C-type asteroids do show hydration bands in their spectra, and are associated with water-rich carbonaceous chondrites, with up to $\sim$ 10wt% (structurally bound) water (Alexander et al. 2013). Additionally, E-type asteroids at 2.0 AU are spectrally associated with enstatite chondrites, which accreted essentially no water (Jacquet et al. 2016). Rarer R chondrites appear to have been water-rich and formed perhaps at 2.6 AU (Desch et al. 2018). At the time the asteroids in the inner disk formed, at $\approx 2 - 3$ Myr (Desch et al. 2018), the snow line must not have extended inward of 2.0 AU; and the asteroids formed between 2 AU and 3 AU or more around this time appear to have sampled a variety of water-ice fractions.

An important caveat in using this data to match onto the disk is that the distribution of asteroids potentially has been substantially altered by gravitational scattering. DeMeo & Carry (2014) were able to extend the study of Gradie & Tedesco (1982) to include the wealth of information attained since then for the smaller asteroids down to 5 km in size, finding that while a sharp radial gradient exists for the distributions of the largest asteroids' spectral types (consistent with the conclusions of Gradie & Tedesco 1982), the smallest asteroids of different classes have been significantly radially mixed. Disk gas-planet and planet-planet interactions and planetary migration, as described in dynamical models of Grand Tack (Walsh et al. 2011), and the Nice models (Gomes et al. 2005; Morbidelli et al. 2005; Tsiganis et al. 2005) and other

models (Izidoro & Raymond 2017) may have led to significant shuffling of the smaller bodies of the asteroid belt. Despite this finding and the need for scattering of C-type asteroids to mix with the main belt, Desch et al. (2018) have argued that radial mixing may be relatively limited to at most 1-2 AU.

Comparing these findings about the asteroid belt to our various disk models, Case II seems least consistent with our asteroid belt. Its snow line does not move inward of 3.5 AU by 3 Myr, and the range of radii over which the asteroid water-ice fractions vary is narrow, < 1 AU. Case II is also marked by a region in which the water-ice fraction of asteroids exceeds the canonical ratio. Case I is broadly consistent with the asteroid belt, with the snow line at about 2.5 AU at 3 Myr, and a broad range of radii over which the asteroid water-ice fractions vary. The gradient of water-ice fractions would be monotonically increasing with distance so that no asteroids would have ice fractions $> 50\%$, for $\alpha > 10^{-3}$. Finally, Case III appears most consistent with the asteroid belt, with the snow line at 2.0 AU at 3 Myr, and a monotonically increasing water-ice fraction in the inner disk.

None of these cases includes the effects of Jupiter opening a gap in the disk, which Morbidelli et al. (2016) have shown to be potentially very important in setting the water content of the inner disk. Nevertheless, our analysis shows how one might use the distribution of asteroids and water content to infer $\alpha(r)$. Future work is encouraged, but so far disk evolution by MRI does not appear consistent with the constraints from our asteroid belt.

3.5 Summary and Conclusions

3.5.1 Summary

The distribution of water and other volatiles in planets depends on how these volatiles are transported through the protoplanetary disk, as diffusing and advected vapor, and as diffusing, advected and drifting icy particles. The partitioning of a volatile between vapor and ice depends on the temperature, and the "snow line" in a disk, demarcating ice-rich and vapor-rich regions, is sensitive to the degree of accretional heating in a disk. The transport of particles and diffusion of vapor and particles depends on the strength of turbulence transporting angular momentum. These processes ultimately depend on the magnitude and spatial variation of α, the turbulence parameter.

We have investigated the effects of different $\alpha(r)$ profiles on the distribution of water in protoplanetary disks. We have considered three $\alpha(r)$ profiles in particular. Our Case I assumes a uniform value of α throughout the disk; our canonical case considers $\alpha = 3 \times 10^{-4}$, but we also have explored higher and lower values. In Case II we investigate a profile of $\alpha(r)$ motivated by simulations of how the MRI would operate in protoplanetary disks, with higher values of α close to the star, where temperatures are hot, and far from the star, where low densities permit high ionization fractions, but low at intermediate radii, where the disk is dominated by MRI "dead zones". This $\alpha(r)$ profile varies between 10^{-4} and 10^{-3}, and is on average close to 3×10^{-4}. This profile is an approximation of the results of Kalyaan et al. (2015). In Case III, we adopt an $\alpha(r)$ profile similar to that of Desch et al. (2018) constructed to explain a variety of meteoritic data. This profile is marked by low $\alpha = 1 \times 10^{-4}$ throughout the disk, but rising at intermediate radii to a an elevated value $\alpha = 1 \times 10^{-3}$ in the inner disk. As in Case II, this profile varies between 10^{-4}

and 10^{-3} and is on average close to $\alpha = 3 \times 10^{-4}$. This profile is consistent with hydrodynamic instabilities like vertical shear instability acting throughout the disk, augmented by magnetic disk winds in the inner disk.

With these $\alpha(r)$ profiles as inputs, we conducted 1-D disk simulations including the transport of vapor and small particles by advection and diffusion, plus transport of chondrule-sized (1 mm) particles by advection, diffusion, and radial drift due to aerodynamic drag. We included the condensation of vapor to ice on chondrule surfaces and the sublimation of ice to vapor. We also accounted for growth of planetesimals from the population of chondrules or icy chondrules, predicting the ice fractions of these asteroidal bodies formed at each distance from the star.

3.5.2 Main Conclusions

We find the following important results:

1. In our simulations, we have assumed the presence of chondrule-sized particles, for which diffusive sizes are quicker tha drift. Nevertheless, it is the variation in rates of drift that contribute to sharp changes in chondrule ice abundance beyond the snow line. The rates of drift determine how much ice mass is carried into the inner nebula, and vapor diffusion efficiently moves outward half of all the ice that diffuses inward, leading to peak water-rock ratios for chondrules just beyond the snow line. If chondrule diffusion is efficient beyond the snow line, these icy chondrules are less likely to drift back towards the snow line. Over time, this water ice gets locked into asteroids that do not drift or migrate.

2. For uniform α disks, we find that the choice of α is important. Less viscid disks show a higher peak abundances of water in asteroids right beyond the snow line, with a narrow peak width. This translates to shaper volatile gradients

in asteroids that could form at different distances. Slight enhancements and depletions in the radial abundance profile are maintained for a longer duration in less viscous disks, which may provide unique localized environments for interesting chemistry. Vapor abundance in the inner disk stays relatively high over time. On the other hand, disks with higher α lead to efficient depletion of water vapor in the inner disk over few Myr timescales. Due to enhanced diffusivity of chondrules beyond the snow line, a shallower peak abundance results, but with a broad peak width. The snow line sweeps a greater distance with time. This may be able to yield a population of asteroids that is diverse in its water content, depending on where and when they formed in the disk, which is likely not the case in less viscous disks. Whatever may be the global value of α however, while the early location of the snow line is dependent on α, the final location (at 5 Myr) seems not to be as dependent on the value of α.

3. Ultimately, for uniform α disks, the order of importance of the various factors determining the magnitude of the peak ice fraction in chondrules beyond the snow line is as follows: $a_{\rm chon} > t_{\rm growth} > \alpha > Sc > \kappa$, i.e., planetary properties are more important than disk properties. The order of importance of factors affecting the peak ice fraction in asteroids beyond the snow line is as follows: $\alpha > t_{\rm growth} >$ everything else. In other words, both disk and planetary parameters are both almost as important as the other.

4. For radially varying α disks, the most important effect is the significant deviation of the underlying gaseous disk structure over a smooth uniform α disk. $\alpha(r)$ also changes the thermal structure of the nebula. These effects are consequential in yielding different radial distribution of volatiles across the disk. In the case of the MRI-α disk, much of the bulk gas (along with the vapor and

chondrules) collects at around 1 AU. Moreover, the snow line does not move much inwards with time. Both of these processes have the effect of yielding large ice-rock ratios of chondrules beyond the snow line. For the hybrid α disk, the higher α in the inner disk lead to high accretion rates, quick depletion of the disk mass, and therefore drastic drop in the temperature of the inner disk. This leads to significant movement of the water snow line. This rapid movement of the snow line does not allow for abundances of ice to reach locally as high values as in the MRI-α case. Unlike the MRI-α case however, it is this disk that can lead to diverse population of asteroids with differing water content.

5. We prefer α profile of CASE III for the solar nebula as it is uniquely consistent with several works in the literature (see §2.2 for a detailed discussion). In this case, we predict from our results the potential locations of formation of chondrites. We speculate that enstatite chondrites formed < 2 AU, ordinary chondrites formed in the 2-4 AU region (after a few Myr) and carbonaceous chondrites formed beyond 5 AU, if they formed earlier during nebular evolution, or beyond 3-4 AU, if they formed later.

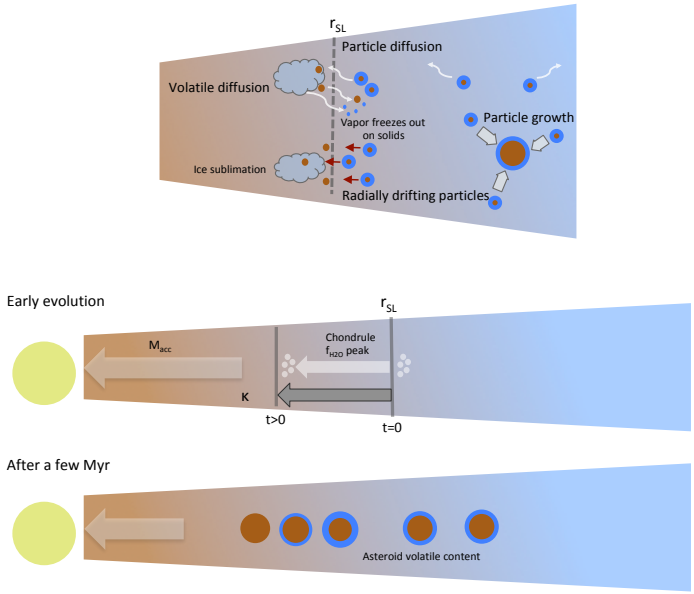

Figure 26: Schematic figures (a, b, c) that show the various processes of radial transport of volatiles across the snow line, and the implications of the redistribution of volatiles over disk evolution. a) A schematic that shows the various radial transport processes that move volatiles bidirectionally through the snow line. All these processes can be sequentially contextualized as follows: 1) particles from the outer disk face a headwind from the pressure-supported gas and therefore spiral inwards; 2) small icy particles well-coupled to the gas also diffuse inwards 2) ice on these particles sublimate on reaching warmer regions of the inner disk; 3) some of this vapor diffuses back through the snow line to refreeze onto solids; 4) ice-bereft particles also diffuse back through, and may gain some of their icy mantles; 5) icy chondrules continue to diffuse both inwards back through the snow line as well as into the outer disk; 6) with time, the particles grow and/or are accreted into asteroids. b) In the early stages of disk evolution, viscous dissipation contributes significantly to the thermal structure of the nebula. Mass accretion rates are initially high. Eventually they drop down and so does the temperature of the inner disk, causing the snow line to move inwards with time. A peak in the ice abundance of chondrules forms just beyond the snowline; as the snow line moves inward, this peak follows with time. c) With time, the collective signature of the redistribution of volatiles through the above processes manifest as the bulk abundance of water available in different bodies at different heliocentric distances. See text for detailed discussion.

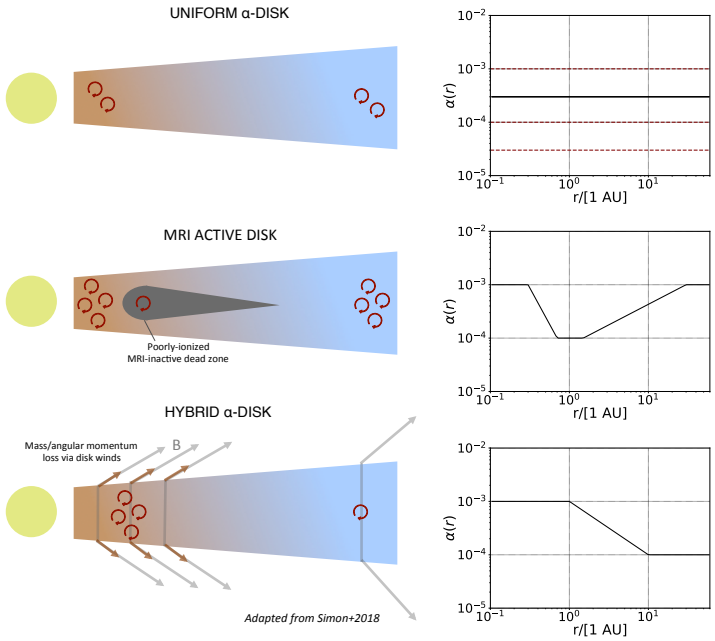

Figure 27: The three α profiles considered in this work depicted with possible physical scenarios that would produce such a radial profile: a) the Uniform α profile, that is constant across radius; the range of constant α values explored in this study is also depicted as red-dashed lines; ii) MRI-α profile, with an active innermost disk and a radially increasing α towards the outer disk; and iii) Hybrid α profile, a turbulent inner disk with radially decreasing α towards the outer disk. See §2.2 for detailed discussion.

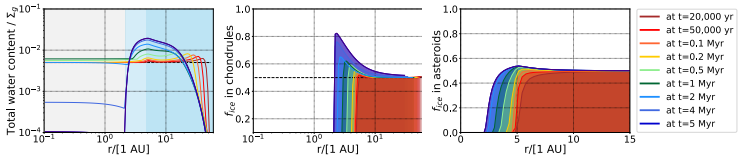

Figure 28: Plots show the results of our canonical uniform α case, i.e, CASE I. Here, α is considered to be 3×10^{-4} at all r. (a) shows total water content/Σ_g with r, where total water = $\Sigma_{\rm vap} + \Sigma_{\rm chon} + \Sigma_{\rm ast}$; (b) shows radial variation in the water-rock ratio in chondrules; (c) shows radial variation in the water-rock ratio in asteroids that grow from chondrules.

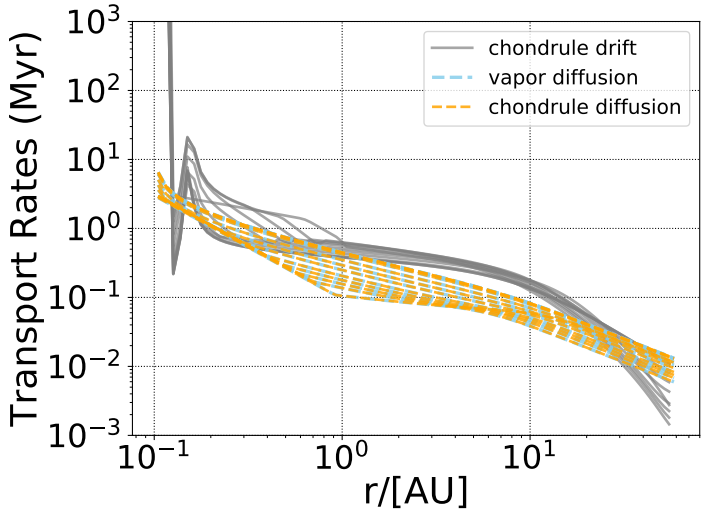

Figure 29: Plot shows the timescales of the various radial transport processes of volatiles for the uniform α case as depicted in Figures 3.3. The gold dotted lines show the radial variation in chondrule diffusion rates at the simulation times plotted in all other plots (20,000 yr - 5 Myr); the blue dotted lines (overlapped by the gold) show the radial variation in vapor diffusion rates; and grey lines show the radial variation in drift rates of chondrules. All transport rates computed for a 1 AU region. We note that on approaching the snow line, drift rates of icy chondrules becomes irrelevant as they are sublimated to vapor, and beyond the snow line, vapor is immediately converted into ice on chondrules, rendering diffusion rates of vapor here invalid. It is nevertheless shown here for completion and because these rates are still valid for silicate chondrules.

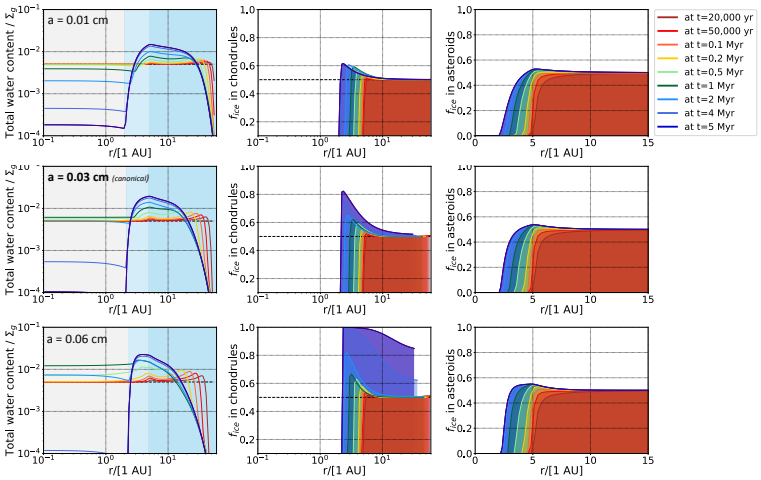

Figure 30: Plots show results of variation of parameter chondrule size a in an uniform α disk. Increasing chondrule size leads to higher chondrule ice-rock ratios beyond the snow line; an indirect effect of more rapidly drifting particles bringing in more water to the inner nebula which is then back-diffused through the snow line to refreeze as ice. Figures and colors same as previous plots.

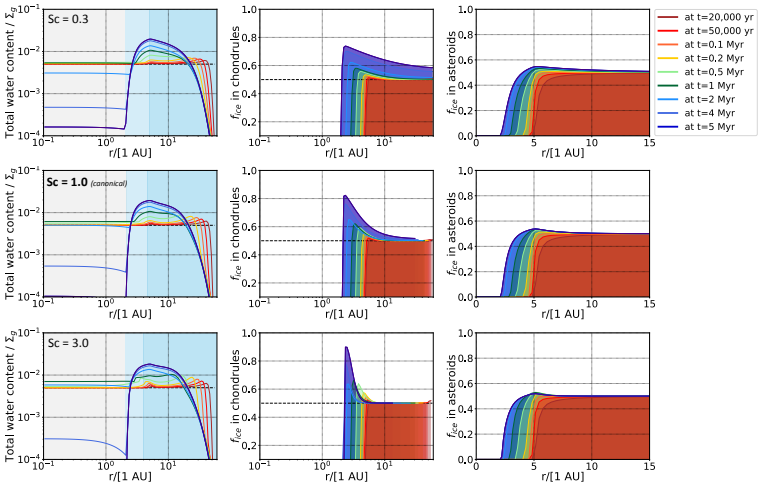

Figure 31: Plots show results of variation of parameter Schmidt number (Sc) in an uniform α disk. Higher Sc (lower diffusivity) leads to higher peak abundance of ice in chondrules beyond the snow line, with a narrow width. Lower Sc leads to lower peak abundance but with a broader width, dependent on the diffusion of icy chondrules in the outer nebula. Figures and colors same as previous plots.

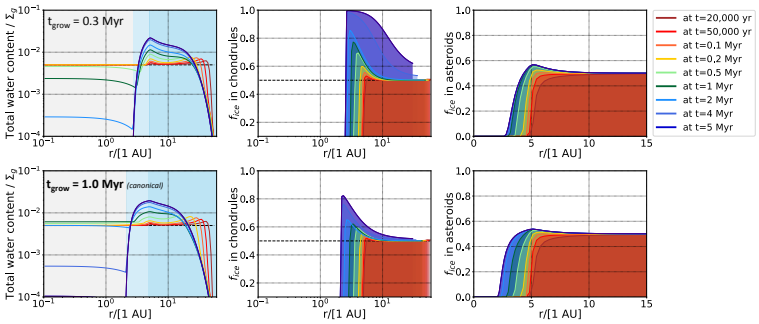

Figure 32: Plots show results of variation of parameter growth timescale of asteroids $t_{\rm grow}$ in an uniform α disk. More rapid growth of asteroids depletes the pool of chondrules for diffusion through the snow line. Figures and colors same as previous plots.

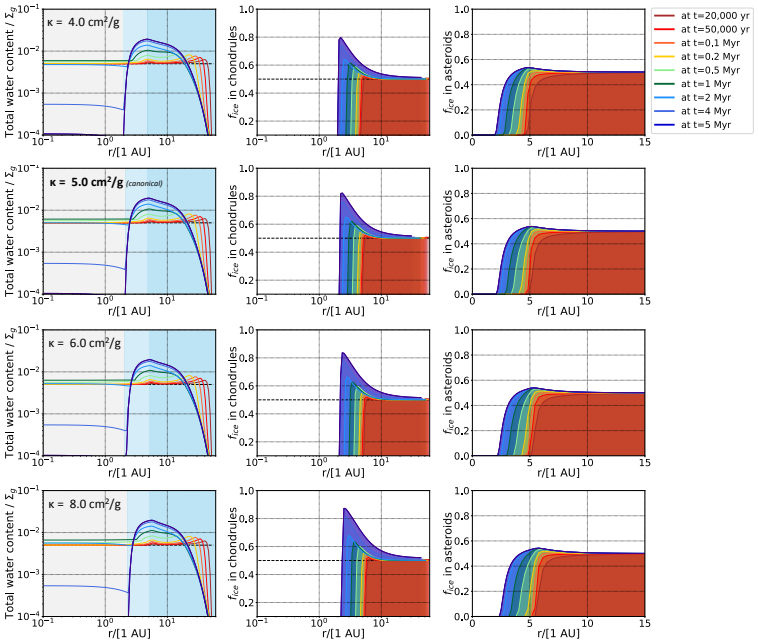

Figure 33: Plots show results of variation of parameter κ in an uniform α disk. Higher κ leads to a warmer disk, that enhances both diffusion and drift rates to a similar extent. Diffusion is still predominant; therefore higher κ therefore leads to a slight increase in peak chondrule ice abundance beyond the snow line. Figures and colors same as previous plots.

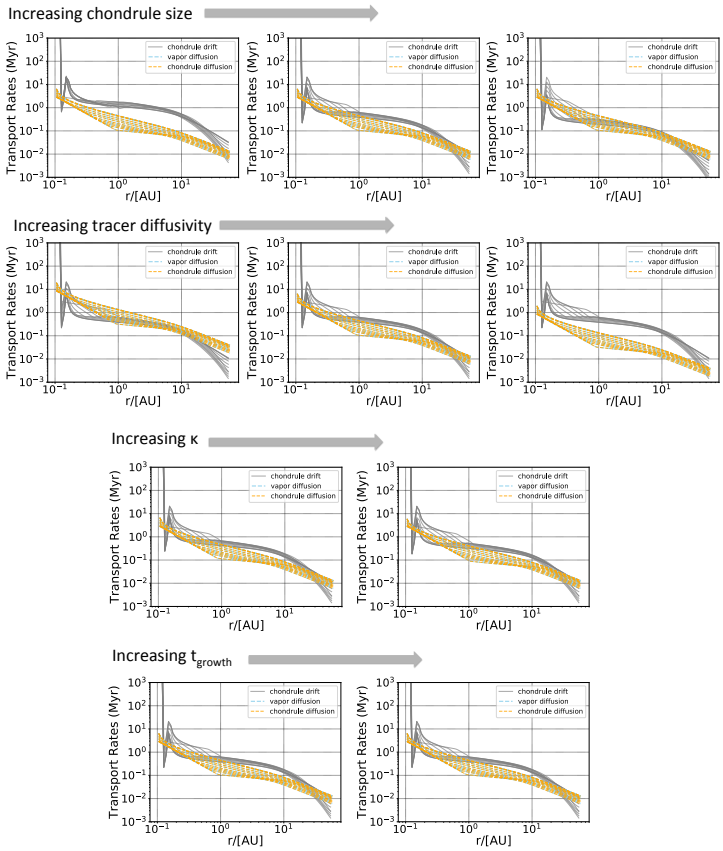

Figure 34: Plots show relative timescales of the different radial transport processes for all the simulations performed in our parameter study, that include varying i) size of the chondrule; ii) diffusivity of water vapor; iii) timescale for growth of chondrules to asteroids; and finally iv) opacity of the disk material. While opacity has little effect on water distribution, $a_{\rm chon}$ and $t_{\rm growth}$ matter most, significantly affecting the abundance of water ice beyond the snow line.

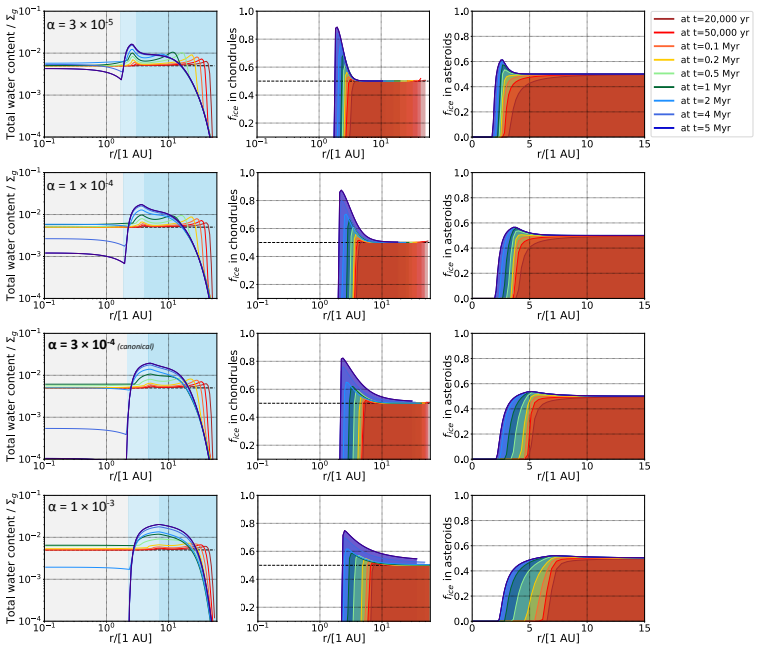

Figure 35: Plots show the results of the different uniform α cases that employ a range of the globally uniform α as indicated. (a) shows total water content/Σ_g with r, where total water $= \Sigma_{\rm vap} + \Sigma_{\rm chon} + \Sigma_{\rm ast}$; (b) shows radial variation in the water-rock ratio in chondrules; (c) shows radial variation in the water-rock ratio in asteroids that grow from chondrules. Figures and colors same as previous plots.

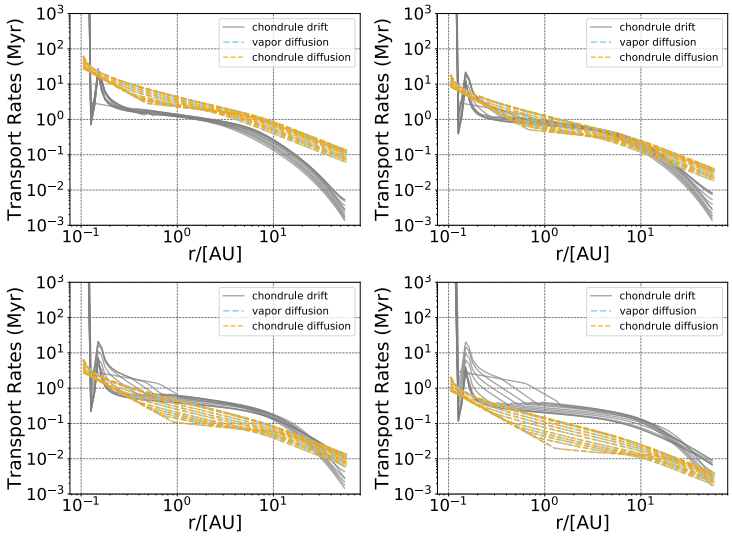

Figure 36: Plots show the timescales of the various radial transport processes of volatiles for different uniform α cases (including the canonical case of uniform α). Colors and lines same as Figure 4. Note that diffusion becomes quicker than drift and therefore is more important as α is increased from $3 \times 10^{-5}(upperleftplot)$ to 1×10^{-3} (bottom right plot).

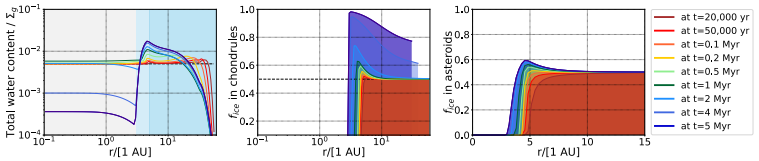

Figure 37: Plots show results of the MRI-α profile, i.e., CASE II. (a) shows total water content/Σ_g with r, where total water = $\Sigma_{\rm vap} + \Sigma_{\rm chon} + \Sigma_{\rm ast}$); (b) shows radial variation in the water-rock ratio in chondrules; (c) shows radial variation in the water-rock ratio in asteroids that grow from these chondrules. See Figures 3.14 and 3.15 for corresponding surface density and temperature radial profile plots. Colors and lines same as in Figure 4.

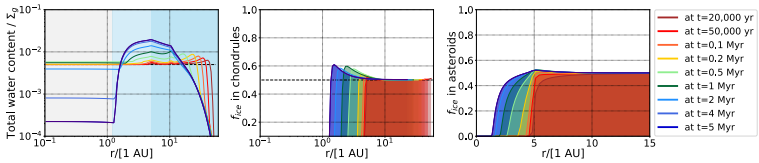

Figure 38: Plots show the evolution of the surface density profiles $\Sigma(r)$ for the three disk evolution models considered in this work: a) the Uniform α profile, b) MRI-α profile, and c) Hybrid α profile. Note the structure of the disk driven by the MRI, with much of the mass concentrated at ~ 1 AU region, as well as the structure of the hybrid α disk with largely constant Σ up to 10 AU. Different colors represent different times: 0 (dashed), 20kyr (red), 50kyr (orange), 100kyr(yellow), 200kyr (light green), 500kyr (green), 1Myr (light blue), 2Myr (blue), 4Myr (dark blue), and 5Myr (violet).

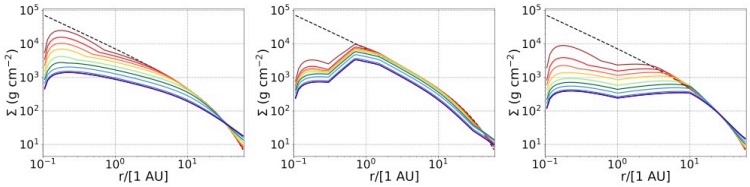

Figure 39: Plots show the evolution of the radial temperature profiles $T(r)$ for the three cases: a) the Uniform α profile, b) MRI-α profile, and c) Hybrid α profile. Different colors represent different times: 0 (dashed), 20kyr (red), 50kyr (orange), 100kyr(yellow), 200kyr (light green), 500kyr (green), 1Myr (light blue), 2Myr (blue), 4Myr (dark blue), and 5Myr (violet).

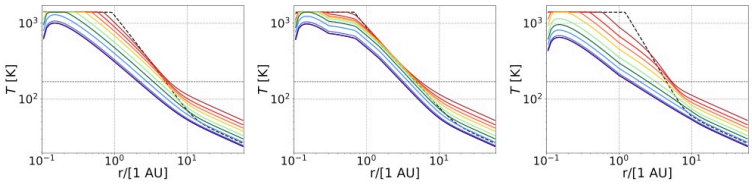

Figure 40: Plots show the timescales of the various radial transport processes for volatiles for the 3 $\alpha(r)$ profiles considered in this work; i) the Uniform α profile, ii) MRI-α profile, and iii) Hybrid α profile. Colors same as in Figure 3.

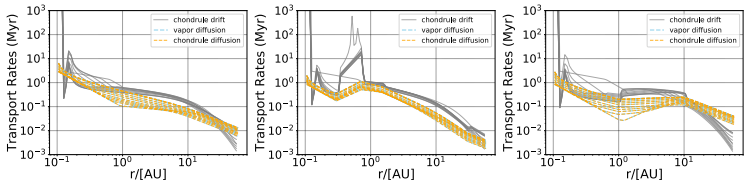

Figure 41: Results of the hybrid-α profile, i.e., CASE III. (a) shows total water content/Σ_g (total water = $\Sigma_{\rm vap} + \Sigma_{\rm chon} + \Sigma_{\rm ast}$) with r; (b) shows radial variation in the water-rock ratio in chondrules; (c) shows radial variation in the water-rock ratio in asteroids. See Figures 39 and 40 for corresponding surface density and temperature radial profile plots. Colors and lines same as in Figure 4.

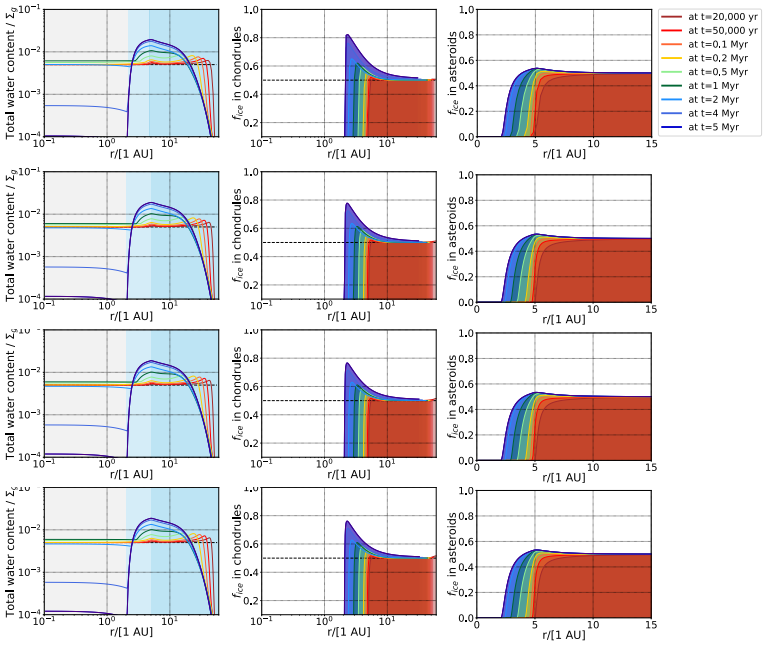

Figure 42: Plots show the results of our convergence study. Resolution increases from left to right with number of radial zones increasing as 100, 200, 300 and 400 radial zones

Chapter 4

FORMATION OF THE LARGEST PLANETS IN DISKS AROUND DIFFERENT STARS

4.1 Introduction

Jupiter is the largest planet in our Solar System. Likely this is because the gas giant formed before any other planets in the disk, and therefore was able to accrete mass for a longer time. Its massive atmosphere and low density (1.33 g cm^{-3}) suggest that Jupiter's core was present in the gaseous disk and accreted enormous quantities of nebular gas in runaway accretion before the disk dissipated after 2 - 3 Myr (Pollack et al. 1996). The rapid accretion of material onto a giant planet yields high rates of accretion that are comparable to disk accretion rates onto the star (10^{-8} $M_\odot$ yr^{-1}; Kley 1999; Mashida et al. 2010). A gap can thus easily be formed by a massive planet undergoing runaway gas accretion. This is consistent with the numerous observations of transitional and pre-transitional disks (i.e., disks with cavities or gaps) around other stars observed by ALMA (Van der Marel et al. 2015, 2017). Such structure is seen in disks as young as 1 Myr (eg. HL Tau; ALMA Partnership 2015). While it is difficult to infer accurately when Jupiter may have formed in the solar nebula, Kruijer et al. (2017) argued that meteoritic studies showed the separation of two isotopic reservoirs in the solar nebula by $\sim$1 Myr. They further argued that this may be due to Jupiter forming a gap in the gas disk, cleaving the nebula into two distinct regions unable to homogeneously mix. This provides an intriguing constraint for the timing of Jupiter's formation in our own solar system, consistent with current observations of protoplanetary disks.

The formation of a disk gap by Jupiter, especially if created earlier in nebular evolution, is likely to have significantly affected transport of material in the disk. Recent research studies (e.g. Morbidelli et al. 2016) suggest that gaps carved by the formation of massive planets beyond the water snow line would inhibit the continuous inward drift of icy pebbles reaching this region. This arises due to a change in the pressure gradient in the outer edge of the gap, halting particles from drifting inward. This may cause planets that form inward of Jupiter and the snow line region to be depleted in water compared to those that formed outside of it. This 'filtering' of particles across the gap is also contingent on their sizes; while larger particles are trapped in the pressure bump beyond the gap, very small μm-sized particles carrying a very small quantity of water may still pass through (Paardekooper & Mellama 2007).

It has been long believed that Jupiter may have formed at the water snow line in the solar nebula. Stevenson & Lunine (1988) and Ros & Johansen (2013) argued that the icy solids beyond the snow line acted like a cold-trap; water vapor in the inner warm nebula diffused outward to freeze out on solids and stayed there. Furthermore, solids with icy surfaces are able to more efficiently coagulate due to their enhanced sticking coefficients (Gundlach & Blum 2016). Additionally, the enhanced solid density at this location may trigger the onset of streaming instability here, resulting in rapid growth ($\sim$ cm-m sizes to $\sim$ dm-km sizes at different radii in the disk; Johansen et al. 2007). Such sizes can provide seed material for the onset of pebble accretion (Bitsch et al. 2015) that may eventually lead to objects the sizes of planetary cores ($\sim$ 100 km).

Once such a core produced by pebble accretion is massive enough, the proto-planetary core is able to accrete gas around it, such that it changes the surrounding pressure gradient and eventually forms a gap in the gaseous disk. Pebbles that are

moderately coupled to the bulk gas of the disk drift towards a negative pressure gradient (Weidenschilling 1977). This causes the drifting pebbles to drift away from the gap and towards the gaseous disk interior and exterior to the gap, halting pebble accretion when the mass of the core reaches the "pebble isolation mass".

In this study, we attempt to understand where the largest planets in disks around different stars may be formed. It is likely that the timing and location of formation of Jupiter had a significant impact on the volatile content of the terrestrial planets. Recent studies estimate that the bulk Earth (crust + mantle + core) may only consist of up to 0.1% water by weight (Mottl et al. 2007; Wu et al. 2018). This is contrary to the results of many sophisticated protoplanetary disk models, which predict that Earth should have accreted a lot of ice, as temperatures similar to the water sublimation temperature ($\sim$ 160 K) should be attained at $\sim$ 1 AU or closer sufficiently early ($\sim$1 Myr) in the evolution of the nebula (Sasselov & Lecar 2000; Garaud & Lin 2007; Lesniak & Desch 2012). The exoplanetary system around an M-dwarf TRAPPIST-1 offers a different vantage point. Using mass-radius-composition models, it is predicted that TRAPPIST-1 planets f and g probably contain as much as 50% water by weight while TRAPPIST b and c contain $\leq$ 15 % by weight (Unterborn et al. 2018). This stark contrast between the water-rich TRAPPIST-1 planets and the water-poor terrestrial planets may be attributable to the types of stars hosting these systems. In this study we strive to understand where and when a Jupiter-like planet may have formed a gap in disks around M, G and A stars. Around M stars, such a planet capable of opening a gap may only be super-Earth sized; or a planet could be much larger than Jupiter around A stars.

In this study, we compute the timing of gap formation $t_{\rm gap}$ at the water snow line in disks around different stars. We also compute how $t_{\rm gap}$ evolves with time. These allow us to calculate the most likely place for a planet to open a gap in a

protoplanetary disk. This study will inform future numerical simulations that will consider the transport of water in disks with planet-induced gaps around different stars.

This rest of the chapter is organized as follows: §4.2 discusses our analytical treatment and numerical computation in detail for disks heated by irradiation only, viscous dissipation only, or both. §4.3 presents the main conclusions of our study.

4.2 Analytic Treatment for Timing of Gap Formation at the Water Snow line

In this paper, we present an analytic treatment that determines the radial efficiency of formation of a protoplanet core via pebble accretion in disks around different stars. In the following analytic treatment, we assume that the core of the protoplanet first forms at the water snow line and investigate the dependence of timing of gap formation on stellar and disk properties. We note that Ida et al. (2016) presented an exhaustive analytical treatment of the radial efficiency of pebble accretion in the disk, considering numerous important parameters. On the contrary, we consider only a few parameters but expand the scope of the treatment to include the dependence of the radial efficiency of pebble accretion to disks around different stars. In the cases of disks heated by only irradiation or only viscous accretion, we show the analytic scaling relations at the water snow line. In the case of disks heated by both sources of heating, we show the results of our numerical calculations for all r.

4.2.1 CASE I: Disk heated by Irradiation

For the passively heated disk, we assume the following temperature profile from Chiang & Goldreich (1997) as used in Desch et al. (2018) and Unterborn et al. (2017):

$$T(r) = 162.66 \left(\frac{L_*}{L_\odot}\right)^{2/7} \left(\frac{M_*}{M_\odot}\right)^{-1/7} \left(\frac{r}{\mathrm{AU}}\right)^{-3/7} \mathrm{K} \tag{4.1}$$

The above radial disk temperature profile is scaled for a disk around a typical G-dwarf star with mass $M_* = 1\ M_\odot$ and luminosity $L_* = 1\ L_\odot$. We assume that water sublimates at $\sim 160\,\mathrm{K}$ in the assumed typical pressures of the solar nebula ($\sim 10^{-4}$ bar; Lodders 2003), and thus derive r_{snow} by setting the left hand side of the above equation to 160 K and solving for r. This yields

$$r_{\mathrm{snow}} = 0.983\left(\frac{L_*}{L_\odot}\right)^{2/3}\left(\frac{M_*}{M_\odot}\right)^{-1/3}\ \mathrm{AU}. \tag{4.2}$$

For the following analytical treatment, we will hereafter solve each quantity at $r = r_{\mathrm{snow}}$.

We use the standard expression for Keplerian orbital frequency Ω, but scale it to stellar properties as stated above, solving at r_{snow}:

$$\Omega = \left(\frac{GM_\odot}{r^3}\right)^{1/2} = (GM_\odot)^{1/2}\mathrm{AU}^{-3/2}\left(\frac{\mathrm{M_*}}{\mathrm{M_\odot}}\right)^{1/2}\left(\frac{\mathrm{r}}{\mathrm{AU}}\right)^{-3/2}\ \mathrm{s}^{-1}.$$

Simplifying the above yields the following expression:

$$\Omega = 2.0445\times 10^{-7}\left(\frac{M_*}{M_\odot}\right)\left(\frac{L_*}{L_\odot}\right)^{-1}\ \mathrm{s}^{-1}. \tag{4.3}$$

We now derive the disk surface density profile Σ (Equation 4.1) at a radius r as follows beginning with the standard power law Σ profile:

$$\Sigma = \Sigma_0\left(\frac{r}{r_0}\right)^p.$$

This is a power law that is scaled as $\Sigma = \Sigma_0$ at a radius r_0. We integrate all the mass in the disk at each annulus, between r_{in} to r_{out} as follows:

$$\begin{aligned}
M_{\mathrm{disk}} =& \int_{r_{\mathrm{in}}}^{r_{\mathrm{out}}} 2\pi r\Sigma_0\left(\frac{r}{r_0}\right)^p dr \\
M_{\mathrm{disk}} =& 2\pi\Sigma_0 r_0\int_{r_{\mathrm{in}}}^{r_{\mathrm{out}}}\left(\frac{r}{r_0}\right)\left(\frac{r}{r_0}\right)^p dr \\
M_{\mathrm{disk}} =& 2\pi\Sigma_0 r_0^2\int_{r_{\mathrm{in}}/r_0}^{r_{\mathrm{out}}/r_0} X^{p+1}dX, \quad \text{where } \mathrm{X} = \mathrm{r}/\mathrm{r_0} \\
M_{\mathrm{disk}} =& \frac{2\pi\Sigma_0 r_0^2}{p+2}\left[\left(\frac{r_{\mathrm{out}}}{r_0}\right)^{p+2} - \left(\frac{r_{\mathrm{in}}}{r_0}\right)^{p+2}\right]
\end{aligned}$$

In the numerical calculations for the disk heated by both passive irradiation and viscous accretion, we use different values of $\mathrm{M_{disk}}$ to denote different stages of disk clearing at different times. For now, we assume that initially, $M_{\rm disk} = 0.1 \times \mathrm{M_*}$ and that half of the disk mass is accreted onto the star when the gap was likely formed, motivated by disk observations:

$$\Sigma_0 = \frac{(p+2)(0.05)M_\odot}{2\pi r_0^2}\left[\left(\frac{r_{\rm out}}{r_0}\right)^{p+2} - \left(\frac{r_{\rm in}}{r_0}\right)^{p+2}\right]^{-1} \ \mathrm{g\,cm^{-2}}$$

If we use the canonical disk profile with $p = -1$, then this expression simplifies to the following result:

$$\Sigma_0 = \frac{0.05M_\odot}{2\pi r_0}\left(\frac{1}{r_{\rm out} - r_{\rm in}}\right) \ \mathrm{g\,cm^{-2}} \tag{4.4}$$

We now assume that the growth of the core by pebble accretion proceeds at the rate given in Bitsch et al. (2015):

$$\dot{M}_{\rm peb} = 2r_H^2\,\Omega\,\tau^{2/3}\Sigma_p \tag{4.5}$$

Here, τ is the Stokes number and $\Sigma_{\rm p}$ is the pebble surface density. The hill radius r_H here refers to the radius of the gravitational sphere of influence of the protoplanet that has attained mass equivalent to the *pebble isolation mass*, i.e., mass of the growing core at which point pebble accretion halts. This threshold implies that the protoplanet has grown massive enough to be able to alter the surrounding pressure gradient in the gas disk. Since small particles tend to drift toward a negative pressure gradient in a disk (Weidenschilling 1977; Birnstiel et al. 2010), pebble streams move away from the core rather than towards it, therefore halting growth of the core.

We now go on to derive each term required for the above expression as follows. The first is the hill radius r_H of the growing core. for which we must first know the disk aspect ratio H/r and the mass of the growing core. For H/r, we can obtain the

desired expression as follows:

$$\frac{H}{r} = \frac{c_s}{\Omega}\frac{1}{r}$$
$$\frac{H}{r} = \left(\frac{kT}{\mu}\right)^{1/2}\left(\frac{r^3}{GM}\right)^{1/2}$$
$$\frac{H}{r} = \left(\frac{k}{\mu G}\right)^{1/2} T^{1/2} r^{3/2} M^{-1/2}$$

We then substitute $T(r)$ for temperature from Equation 4.1 and $r_{\rm snow}$ for r from Equation 4.2 into the above equation to get H/r in terms of stellar mass and luminosity.

$$\left.\frac{H}{r}\right|_{r=r_{\rm snow}} = \frac{k(160)(0.983)\mathrm{AU}}{\mu\, G M_\odot}^{1/2}\left(\frac{L_*}{L_\odot}\right)^{1/3}\left(\frac{M_*}{M_\odot}\right)^{-2/3}$$

$$\left.\frac{H}{r}\right|_{r=r_{\rm snow}} = 0.025\left(\frac{L_*}{L_\odot}\right)^{1/3}\left(\frac{M_*}{M_\odot}\right)^{-2/3} \tag{4.6}$$

We then calculate pebble isolation mass using the prescription from Lambrechts et al. (2014) as given below:

$$M_{\rm p} = M_*\left(\frac{H}{r}\right)^3.$$

We substitute H/r from Equation 4.8, divide by $M_\odot$ for scaling the expression to solar mass as the above expressions are scaled (and multiply by $M_\odot$, as well as divide by $M_\oplus$) to obtain the following expression in Earth masses:

$$M_{\rm p}|_{r=r_{\rm snow}} = \frac{M_\odot}{M_\oplus}(0.0251)^3\left(\frac{M_*}{M_\odot}\right)\left[\left(\frac{L_*}{L_\odot}\right)^{1/3}\left(\frac{M_*}{M_\odot}\right)^{-2/3}\right]^3 \; M_\oplus$$

$$M_{\rm p}|_{r=r_{\rm snow}} = 5.2\left(\frac{L_*}{L_\odot}\right)\left(\frac{M_*}{M_\odot}\right)^{-1} \; M_\oplus \tag{4.7}$$

We can then calculate the Hill radius of the core, by assuming the mass of the core is equivalent to the pebble isolation mass, simultaneously scaling the expression

to solar, as follows:

$$r_H = r \left(\frac{M_{\rm peb}}{3M_*}\right)^{1/3}$$
$$r_H = \left(\frac{1}{3}\right)^{1/3} \mathrm{AU}\ \mathrm{M}_\oplus^{1/3}\, \mathrm{M}_\odot^{-1/3}\, \mathrm{r} \left(\frac{\mathrm{M_p}}{3\,\mathrm{M}_*}\right)^{1/3}.$$

This simplifies to

$$r_H|_{r=r_{\rm snow}} = 0.017 \left(\frac{L_*}{L_\odot}\right)\left(\frac{M_*}{M_\odot}\right)^{-1}\ \mathrm{AU}. \tag{4.8}$$

Finally, we calculate the $\tau^{2/3}\ \Sigma_p$, where τ is the Stokes number of the particles, and Σ_p is the pebble surface density:

$$\tau^{2/3}\big|_{r=r_{\rm snow}}\ \Sigma_p = \left(\frac{\pi}{2}\frac{a\,\rho_s}{\Sigma}\right)^{2/3} f\,\Sigma_g$$

The pebbles are assumed to be in the Epstein regime (where the size of the particles are smaller than the mean free path at r. Pebble surface density is inherently a complex quantity to determine. We therefore assume a simplified spatially uniform value of $f = 0.001$, where f is the ratio of pebble-gas mass at each r. The above expression is scaled as before, simplified and reproduced here:

$$\tau^{2/3}\ \Sigma_p = 0.1474 \left(\frac{\rho_s}{3\,\mathrm{g/cm^3}}\right)^{2/3}\left(\frac{a}{\mathrm{cm}}\right)^{2/3}\left(\frac{f}{0.001}\right)\left(\frac{M_*}{M_\odot}\right)^{4/9}\left(\frac{L_*}{L_\odot}\right)^{-2/9}\left(\frac{r_{\rm out}}{\mathrm{AU}}\right)^{-1/3} \tag{4.9}$$

Having derived each term, we put all the above scaling relations together in $\dot{M}_{\rm peb}$ prescription as in Equation 4.7 as follows:

$$\begin{aligned}\dot{M_{\rm peb}}\Big|_{r=r_{\rm snow}} = 2 &\left[0.017\left(\frac{L_*}{L_\odot}\right)\left(\frac{M_*}{M_\odot}\right)^{-1}\right]^2 \times \\ &\left[2.0445\times10^{-7}\left(\frac{M_*}{M_\odot}\right)\left(\frac{L_*}{L_\odot}\right)^{-1}\right]\times \\ &\left[0.1474\left(\frac{\rho_s}{3\,\mathrm{g/cm^3}}\right)^{2/3}\left(\frac{a}{\mathrm{cm}}\right)^{2/3}\left(\frac{f}{0.001}\right)\left(\frac{M_*}{M_\odot}\right)^{4/9}\left(\frac{L_*}{L_\odot}\right)^{-2/9}\left(\frac{r_{\rm out}}{\mathrm{AU}}\right)^{-1/3}\right].\end{aligned}$$

Simplifying the above equation yields the following scaling relation:

$$\dot{M}_{\rm peb}\Big|_{r=r_{\rm snow}} = 2.065\times10^{-5}\left(\frac{L_*}{L_\odot}\right)^{\frac{7}{9}}\left(\frac{M_*}{M_\odot}\right)^{-\frac{5}{9}}\left(\frac{\rho_s}{3\,{\rm g\,cm^{-3}}}\right)^{\frac{2}{3}}\left(\frac{a}{\rm cm}\right)^{\frac{2}{3}}\left(\frac{f}{0.001}\right)\left(\frac{r_{\rm out}}{\rm AU}\right)^{-\frac{1}{3}}\ {\rm M_\oplus yr^{-1}} \tag{4.10}$$

Finally, we derive the timing of gap formation at the snow line by dividing pebble isolation mass $M_{\rm peb}$ by $\dot{M}_{\rm peb}$ from Equations 4.9 and 4.12:

$$\begin{aligned} t_{\rm gap}|_{r=r_{\rm snow}} =& \frac{M_p}{\dot{M}_{\rm peb}} \\ =& \frac{5.2\left(\frac{L_*}{L_s}\right)\left(\frac{M_*}{M_s}\right)^{-1}\ M_\oplus}{2.065\times10^{-5}\left(\frac{L_*}{L_s}\right)^{7/9}\left(\frac{M_*}{M_s}\right)^{-5/9}\left(\frac{\rho_s}{3\,{\rm g\,cm^{-3}}}\right)^{2/3}\left(\frac{a}{\rm cm}\right)^{2/3}\left(\frac{f}{0.001}\right)\left(\frac{r_{\rm out}}{\rm AU}\right)^{-1/3}\ {\rm M_\oplus\,yr^{-1}}} \end{aligned}$$

Simplifying leads us to the final expression for $t_{\rm gap}$, at the location of the snow line.

$$t_{\rm gap}|_{r=r_{\rm snow}} = 0.252\left(\frac{L_*}{L_s}\right)^{\frac{2}{9}}\left(\frac{M_*}{M_s}\right)^{-\frac{4}{9}}\left(\frac{\rho_s}{3\,{\rm g\,cm^{-3}}}\right)^{-\frac{2}{3}}\left(\frac{a}{\rm cm}\right)^{-\frac{2}{3}}\left(\frac{r_{\rm out}}{\rm AU}\right)^{-\frac{1}{3}}\left(\frac{f}{0.001}\right)^{-1}\ {\rm Myr} \tag{4.11}$$

4.2.2 CASE II: Disk heated by Accretion

We now repeat a similar treatment for the case of a disk heated by only viscous dissipation. As viscous heat is an internal property of the disk, $T(r)$ does not depend on L_* and M_* as before. We use the radial temperature profile from the 3D-radiative transfer axisymmetric disk simulations of Min et al. (2011):

$$T(r) = \left(\frac{27}{128}\right)\frac{\Sigma(r)^2\kappa\,\alpha\,k\,\Omega}{\mu\,\sigma_{\rm sb}}\ \ {\rm K.} \tag{4.12}$$

Here, κ is the opacity of the disk material, k is the boltzmann constant, $\sigma_{\rm sb}$ is the Stefan-Boltzmann constant, and α is the turbulent viscosity from the standard parameterization of Shakura & Sunyaev (1973). We assume a value of uniform $\alpha = 10^{-4}$ throughout r, and use Σ as in Equation 4.4 and Ω from Equation 4.3, then scale

M_* to $M_\odot$, to obtain:

$$T = 6438.2 \left(\frac{\kappa}{5}\right)^{1/3} \left(\frac{M_*}{M_\odot}\right)^{5/6} \left(\frac{r}{\mathrm{AU}}\right)^{-7/6} \left(\frac{r_{\mathrm{out}}}{\mathrm{AU}}\right)^{-2/3} \ \mathrm{K} \tag{4.13}$$

As before, we set $T = 160$ K for the snow line and solve for r to obtain:

$$r_{\mathrm{snow}} = 23.74 \left(\frac{M_*}{M_\odot}\right)^{5/7} \left(\frac{r_{\mathrm{out}}}{\mathrm{AU}}\right)^{-4/7} \left(\frac{\kappa}{5}\right)^{2/7} \ \mathrm{AU} \tag{4.14}$$

Ω is calculated by substituting r with r_{snow} from Equation 4.16:

$$\Omega|_{r=r_{\mathrm{snow}}} = 1.723 \times 10^{-9} \left(\frac{M_*}{M_\odot}\right)^{-4/7} \left(\frac{r_{\mathrm{out}}}{\mathrm{AU}}\right)^{6/7} \left(\frac{\kappa}{5}\right)^{-3/7} \ \mathrm{s}^{-1} \tag{4.15}$$

Proceeding as before, we find H/r:

$$\left.\frac{H}{r}\right|_{r=r_{\mathrm{snow}}} = 0.1232 \left(\frac{M_*}{M_\odot}\right)^{-1/7} \left(\frac{r_{\mathrm{out}}}{\mathrm{AU}}\right)^{-2/7} \left(\frac{\kappa}{5}\right)^{1/7}, \tag{4.16}$$

as well as M_{p}:

$$M_{\mathrm{p}}|_{r=r_{\mathrm{snow}}} = 622.3 \left(\frac{M_*}{M_\odot}\right)^{4/7} \left(\frac{r_{\mathrm{out}}}{\mathrm{AU}}\right)^{-6/7} \left(\frac{\kappa}{5}\right)^{3/7} \ M_\oplus. \tag{4.17}$$

Having solved for M_{p}, we now obtain for expression for r_{H} in AU:

$$r_{\mathrm{H}}|_{r=r_{\mathrm{snow}}} = 2.027 \left(\frac{M_*}{M_\odot}\right)^{4/7} \left(\frac{r_{\mathrm{out}}}{\mathrm{AU}}\right)^{-6/7} \left(\frac{\kappa}{5}\right)^{3/7} \ \mathrm{AU}. \tag{4.18}$$

We assume that $\Sigma(r)$ follows as Equation 4.4 with $p = 1$ to obtain:

$$\tau^{2/3}\Sigma_p\big|_{r=r_{\mathrm{snow}}} = 0.0511 \left(\frac{f}{0.001}\right) \left(\frac{M_*}{M_\odot}\right)^{2/21} \left(\frac{r_{\mathrm{out}}}{\mathrm{AU}}\right)^{-1/7} \left(\frac{\kappa}{5}\right)^{-2/21} \left(\frac{\rho_s}{3\,\mathrm{g\,cm^{-3}}}\right)^{2/3} \left(\frac{a}{\mathrm{cm}}\right)^{2/3} \mathrm{g\,cm^{-2}} \tag{4.19}$$

Finally, with all the individual terms expressed as the required scaling relations in Equations 4.15, 4.20 and 4.21, we find the following equation for $\dot{M}_{\mathrm{peb}}$ scaled by our assumed canonical values of physical quantities as follows:

$$\dot{M}_{\mathrm{peb}}\Big|_{r=r_{\mathrm{snow}}} = 8.52 \times 10^{-4} \left(\frac{M_*}{M_\odot}\right)^{2/3} \left(\frac{r_{\mathrm{out}}}{\mathrm{AU}}\right)^{-1} \left(\frac{\kappa}{5}\right)^{1/3} \left(\frac{\rho_s}{3\,\mathrm{g\,cm^{-3}}}\right)^{2/3} \left(\frac{a}{\mathrm{cm}}\right)^{2/3} \left(\frac{f}{0.001}\right) \mathrm{M_\oplus/yr} \tag{4.20}$$

As $t_{\rm gap} = M_p/\dot{M}_{\rm peb}$, this yields the following expression for timing of gap formation in an accretionally heated disk:

$$t_{\rm gap}|_{r=r_{\rm snow}} = 0.73 \left(\frac{M_*}{M_\odot}\right)^{-2/21} \left(\frac{r_{\rm out}}{\rm AU}\right)^{1/7} \left(\frac{\kappa}{5}\right)^{2/21} \left(\frac{f}{0.001}\right)^{-1} \left(\frac{\rho_s}{3\,{\rm g\,cm^{-3}}}\right)^{-2/3} \left(\frac{a}{\rm cm}\right)^{-2/3} {\rm Myr} \tag{4.21}$$

4.2.3 CASE III: Disk heated by Irradiation and Accretion

In addition to calculating the pebble isolation mass and time of gap formation at the snow line in disks in the passively irradiated and actively accreting limits, we also calculate these quantities as a function of arbitrary r in disks that are heated by either mechanism, or by both mechanisms. For the combined heating case, we sum each of these heating contributions in quadrature as follows:

$$T(r) = \left(T_{\rm acc}^4 + T_{\rm pass}^4\right)^{1/4} \ {\rm K}. \tag{4.22}$$

The results of these numerical calculations are presented in Figure 43. Each panel of Figure 43 shows a different quantity. The calculation is performed at a specific instance in the disk's evolution, when the surface density has decreased by a factor of 2 from the initial profile. Figure 43a shows the midplane temperature $T(r)$ as a function of distance from the star, r; the temperature drops off quickly with distance in the regions where viscous accretion dominates, then falls off less rapidly in regions where the disk is passively heated by stellar irradiation. The radius of transition between the viscous heating and passively heated cases we call $r_{\rm vp}$. Figure 43b shows the aspect ratio of the disk, H/r, as a function of r. Beyond about 2 AU, where the disk is passively heated, the disk is flaring and H/r increases with r; but interior to this radius, the rapid decrease in temperature with r means the disk aspect ratio decreases with r. This means the aspect ratio is at a minimum at an intermediate distance. Figure 43c shows the local pebble isolation mass $M_{\rm p}$ as a function of r.

Because $M_{\rm p}$ scales as the cube of the disk aspect ratio, the pebble isolation mass also is at a minimum at an intermediate radius, near $r_{\rm vp} \approx 3$ AU. This minimum in pebble isolation mass only occurs in systems like Case III, that have a transition between active accretion and passive heating. Figure 43d shows the Hill radius associated with a planet that has achieved the pebble isolation mass, as a function of r. The Hill radius scales approximately as r, modified by the factor $M_{\rm p}^{1/3}$. Figure 43e shows the pebble accretion rate as a function of r. Remarkably, in our actively accreting disk case, this quantity does not vary with r, but it rises steeply with distance in the passively heated disk. Finally, figure 43f shows the time it takes for a planet to achieve the local pebble isolation mass, by accreting at the pebble accretion rate, as a function of r. This is equivalent to the time it takes to reverse the pressure gradient in the disk and reverse the inward drift of pebbles, which is more or less the time taken to open a gap in the disk. This quantity reaches a minimum at the same transition radius $r_{\rm vp} \approx 3$ AU. Importantly, and coincidentally, the transition radius $r_{\rm vp}$ happens to occur at the same radius where ice sublimates, given by the vertical blue dotted line in each panel.

Figure 44 shows the radial variation of the local pebble isolation mass, and the time taken to achieve it at the pebble accretion rate, as a function of r, at three stages in the disk's evolution: when the mass has been depleted from the original amount by 20%, 50%, and 80%. The median time for G dwarf disks to stop accreting onto their stars is ≈ 3 Myr (Haish et al. 2001), so these disk masses are proxies for evolution times scales of $\ll 1$ Myr, ~ 3 Myr, and much later than 3 Myr. Despite the fact that the mass accretion rates are uniform inside the transition radius $r_{\rm vp}$, the time needed to form a planet large enough to open a gap is larger closer to the star, because the disk aspect ratio and mass needed to open a gap are larger, due to accretion heating. The minimum time to open a pebble gap is found at radii that move inward over

time, from about 4 AU, to 2 AU, to 1 AU. The minimum time to open a pebble gap tends to be shorter in a more massive disk: it is about 1.3 Myr when the disk is only 20% depleted, 1.4 Myr when the disk is 50% depleted, and about 1.8 Myr when the disk is 80% depleted. A disk only 20% depleted from its original mass is probably too young to have opened up a gap, but a 50% depleted disk would not. Therefore we conclude that the first planet to grow by pebble accretion and achieve pebble isolation mass would do so at about 2 AU, at a time close to 1.5 Myr, when the disk is more than 20%, and closer to 50%, depleted. The pebble isolation mass would be $\approx 12\,M_{\oplus}$. This would be roughly when and where the core of Jupiter would have formed in our solar system.

After this first (pebble) gap-opening planet forms, it may deprive the disk interior to it of a flow of pebbles. The growth rates of other planetary embryos interior to the first one at ≈ 2 AU are insensitive to r, so they would have reached the same mass in the same amount of time. Thereafter, they may have ceased growing, as the first, large planet cut off the flow of pebbles. If so, they would have also stalled at about $12\,M_{\oplus}$, but without opening a gap. It is highly likely that they would have undergone rapid, inward type I migration, but may have been unable to halt their migration by growing larger.

At any rate, the first large planet is likely to have formed near the radius $r_{\rm vp}$, where $T(r)$ transitions from the viscous heating temperature profile to the irradiation profile. Setting $T(r)$ derived from each profile equal to each other from Equations 4.1 and 4.15, we obtain the following expression by assuming a disk of radial size 60 AU:

$$420.08\left(\frac{\kappa}{5\,\mathrm{cm^2\,g^{-1}}}\right)^{1/3}\left(\frac{M_*}{M_\odot}\right)^{5/6}\left(\frac{r}{AU}\right)^{-7/6} = 162.66\left(\frac{L_*}{L_\odot}\right)^{2/7}\left(\frac{M_*}{M_\odot}\right)^{-1/7}\left(\frac{r}{\mathrm{AU}}\right)^{-3/7}$$

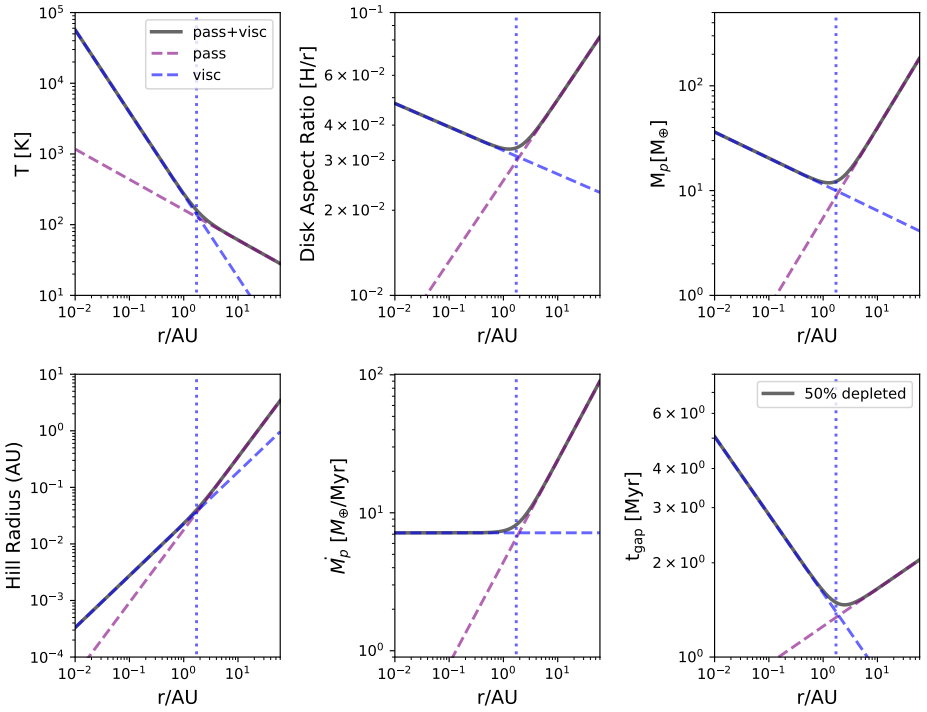

Figure 43: Quantities relevant to growth of planetary embryos by pebble accretion in a disk around a G dwarf, heated by both irradiation and viscous dissipation, with $\Sigma(r)$ varying as r^{-p} with slope $p = 1$. The subpanels are: temperature versus distance from star, r; aspect ratio of the disk, H/r; the local pebble isolation mass; the Hill radius associated with a planet with the local pebble isolation mass; the local rate of accretion of pebbles by a planet; and the time taken for a planet to achieve the pebble isolation mass and open a gap (in the pebbles) in the disk.

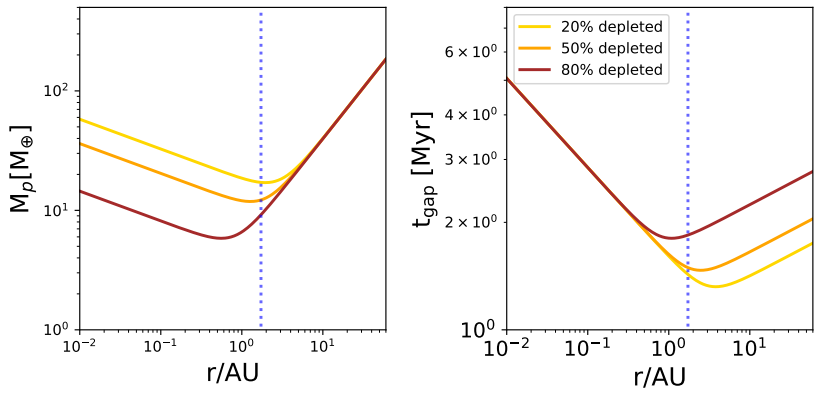

Figure 44: Pebble accretion rate (*left*) and time to open a gap (*right*) in disks around a G dwarf, at different times in their evolution such that 20%, 50%, or 80% of the initial mass has been lost. At different times and disk masses, the location of $r_{\rm vp}$ and the minimum in $t_{\rm gap}$ lie at different radii, but close to the snow line location (drawn as the vertical blue dotted line for the case where the disk is 50% depleted.

Rearranging the terms and simplifying the above expression yields:

$$r_{\rm vp} = 3.616 \left(\frac{L_*}{L_\odot}\right)^{-12/31} \left(\frac{M_*}{M_\odot}\right)^{41/31} \left(\frac{\kappa}{5\,{\rm cm^2\,g^{-1}}}\right)^{14/31} {\rm AU}. \tag{4.23}$$

To find the temperature at which this transition occurs, we substitute this expression for r in Equation 4.1 to obtain

$$T_{\rm vp} = 162.66 \left(\frac{L_*}{L_\odot}\right)^{2/7} \left(\frac{M_*}{M_\odot}\right)^{-1/7} \left[3.616 \left(\frac{L_*}{L_\odot}\right)^{-12/31} \left(\frac{M_*}{M_\odot}\right)^{41/31} \left(\frac{k}{5}\right)^{14/31}\right]^{-3/7},$$

which yields the simplified scaling relation:

$$T_{\rm vp} = 93.77 \left(\frac{L_*}{L_\odot}\right)^{14/31} \left(\frac{M_*}{M_\odot}\right)^{-22/31} \left(\frac{\kappa}{5\,{\rm cm^2\,g^{-1}}}\right)^{-6/31} {\rm K}. \tag{4.24}$$

We see that this transition temperature, $T_{\rm vp}$, is not dissimilar from the sublimation temperature of water ice, ≈ 160 K, although $T_{\rm vp}$ does show a significance dependence on the stellar properties of luminosity and mass. Planet formation by pebble accretion is likely to first occur at this radius, but not necessarily directly as a cause of ice sublimation. The presence of ice may nevertheless increase the pebble accretion rate and decrease $t_{\rm gap}$ beyond the snow line.

4.2.4 Disks around other stars

We now investigate where the minimum in $t_{\rm gap}$ is located in disks around different stars. We repeat the above numerical calculations and present similar plots for disks around M and A stars, with different $M_{\rm disk}$ corresponding to different stages of disk evolution. The stellar masses and luminosities are given in Table 2. In this table, the calculated values for $r_{\rm vp}$, $\rm M_{peb}$ and $\rm t_{gap}$ at the $\rm r_{vp}$.

Some remarkably long-lived M dwarf disks exist, including a 45 Myr old disk (Silverberg et al. 2018). Considering M dwarf disks evolve more slowly than G dwarf disks, the disk may be closer to only 20% depleted after a few Myr. From Figures 45

Stellar Type	M_* [$M_\odot$]	L_* [$L_\odot$]	$r_{vp}[AU]$	M_{peb} [$M_\oplus$]	$t_{gap,min}$ [Myr]	Figures
M Dwarf	0.08	0.1	0.5	3.0	2	Figure 43, 44
G Dwarf	1.0	1.0	2.0	12.0	1.5	Figure 45, 46
A Star	2.0	10.0	2.0	20.0	1.5	Figure 47, 48

Table 2: Table shows our assumed stellar parameters for M, G and A stars and calculated values of M_{peb} at radius r_{vp} and at time t_{gap} corresponding to minima in Figures 43, 45 and 47 for 50 % disk depletion.

and 46, it is then seen that the first planet to form by pebble accretion and achieve pebble isolation mass is likely to do so at about 0.3 AU, when the disk is between 20% and 50% depleted. The pebble isolation mass is necessarily small, about 3 or 4 $M_\oplus$, similar to the masses of the planets in the Trappist-1 system (typically $< 2M_\oplus$; Gillon et al. 2016). Our predicted results for M stars match closely the mass and location of the newly discovered planet orbiting Barnard's Star, $> 3.3M_\oplus$ at 0.4 AU (Ribas et al. 2018). Because these planets would be $< 10M_\oplus$, they might lack sufficient mass to initiate runaway gas accretion (Pollack et al. 1996), and would therefore not become Jupiter-mass planets, although they may retain thick H_2/He atmospheres.

For A stars, we assume similar but somewhat shorter disk lifetimes, so that the relevant timescales are at a few Myr, when the disk is roughly 50% depleted. From Figures 47 and 48, it is seen that the first planet to form by pebble accretion and achieve pebble isolation mass is likely to do so at about 2 AU, at about 1.5 Myr. The pebble isolation mass would be about 20 $M_\oplus$. Because this appears to exceed the threshold for runaway gas accretion, disks around A stars would seem most able to produce Jupiter-mass planets, consistent with the higher frequency of jovian planets around A stars (Ribas et al. 2015).

In each of these cases, the first planet to form and open a pebble gap, thereby affecting the system architecture, is likely to do so near r_{vp}, where the heating in the

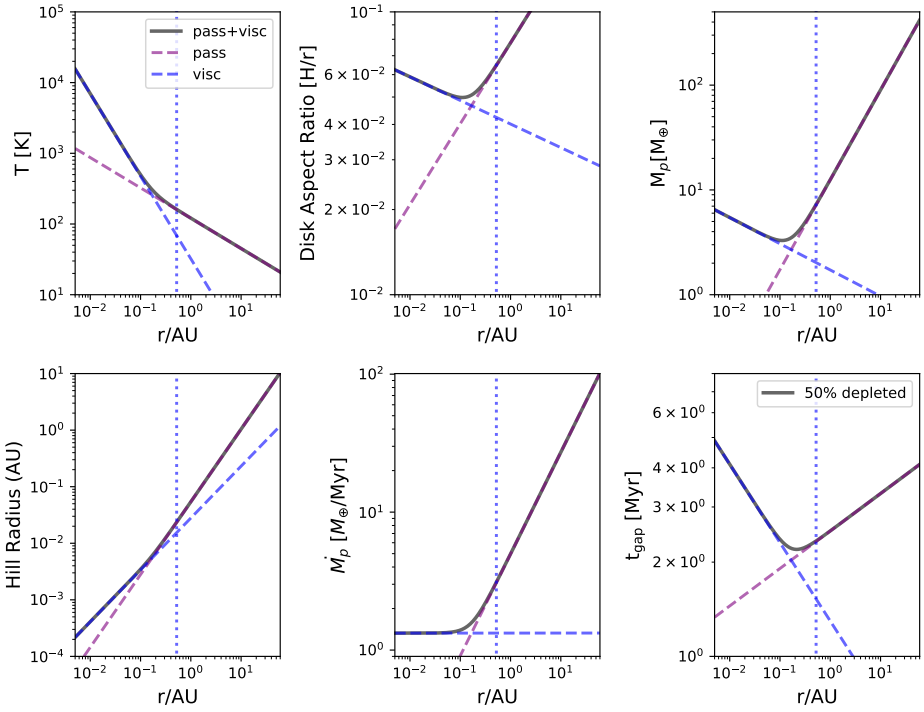

Figure 45: Same as Figure 43, but for the case of a disk around an M dwarf.

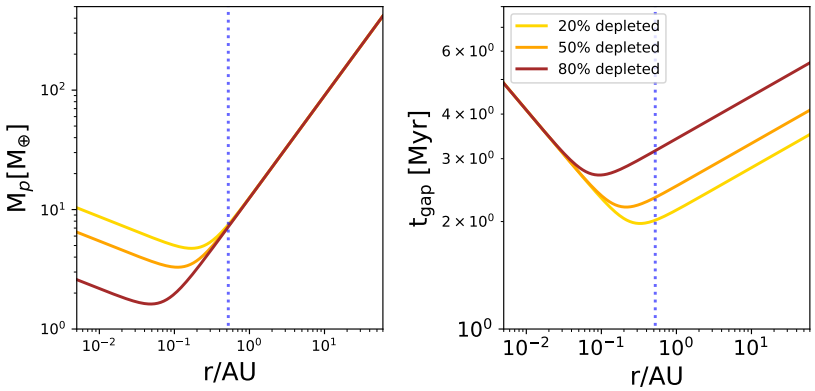

Figure 46: Same as Figure 44, but for the case of a disk around an M dwarf. The first planet to form and open a pebble gap is likely to do so at about 0.3 AU, inside the snow line at 0.5 AU.

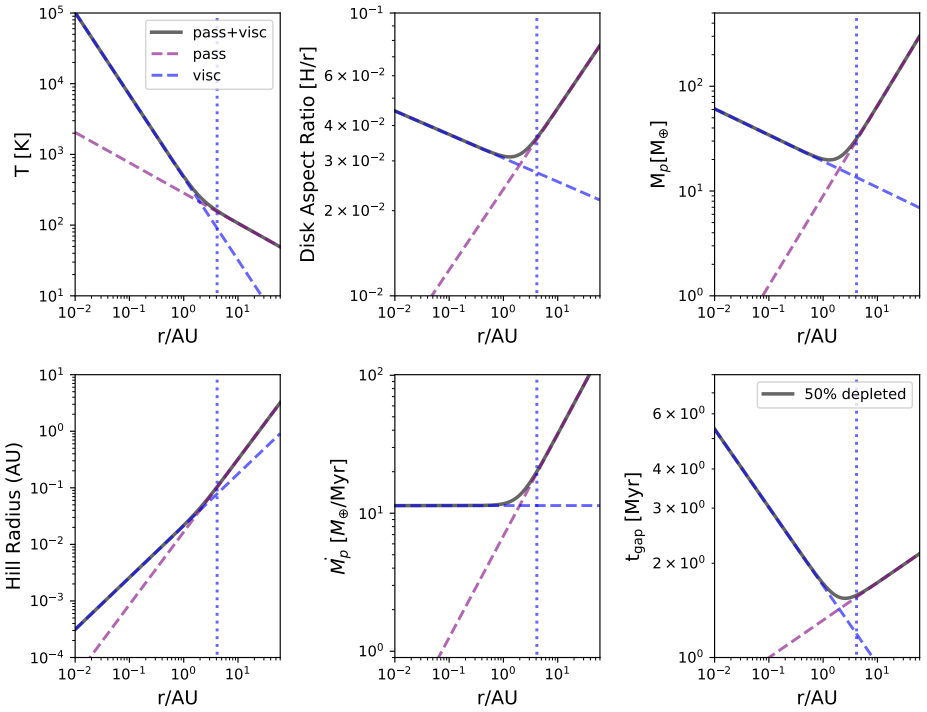

Figure 47: The case of a disk around an A star.

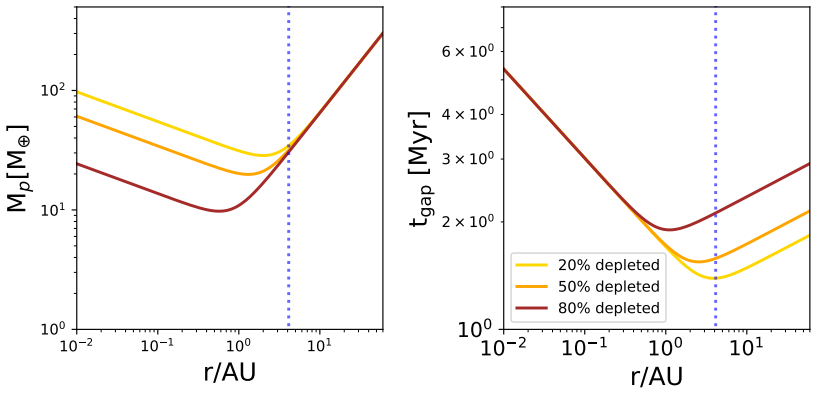

Figure 48: The case of a disk around an A star. The first planet to form and open a pebble gap is likely to do so at about 2 AU, inside the snow line at 4 AU.

disk transitions from viscous dissipation to passive irradiation. The temperature at $r_{\rm vp}$ is not dissimilar to the ice sublimation temperature, so $r_{\rm vp}$ tends to be close to $r_{\rm snow}$, but not coincident with it. In fact, the first large planets likely form inside $r_{\rm snow}$ in disks around M and A stars, unless the presence of ice beyond the snow line significantly increases growth rates. In G star disks, $r_{\rm vp}$ lies closer to the snow line. Both $r_{\rm vp}$ and $r_{\rm snow}$ tend to move inward over time as temperatures in the disk decrease.

4.3 Conclusions and Summary

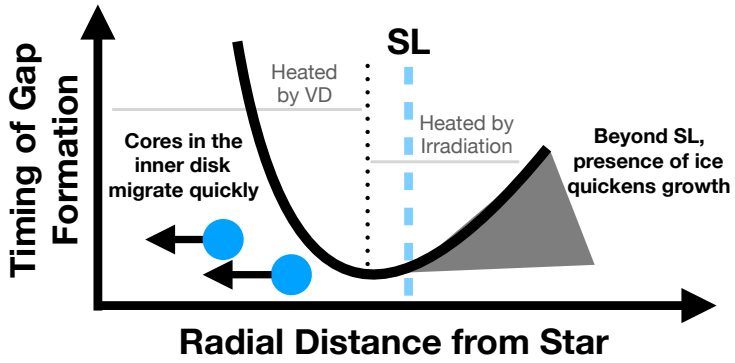

Figure 49: Schematic of radial variation of the timing of formation of pebble isolation mass planets.

In this work, we performed analytical and numerical calculations to determine the radial variation of the ability of pebble accretion to create a planet large enough to reverse the pressure gradient in the disk and achieve pebble isolation mass. We conducted these calculations for disks around stars of spectral type M, G and A. We made a few assumptions to simplify our calculations: i) that cores of planets are rapidly formed by pebble accretion; and ii) that once pebble isolation mass is achieved, a gap is created in the disk soon after. The latter allows us to compute the timing of gap formation from the knowledge of rate of core growth by pebble accretion. We

therefore make the implicit assumption that attainment of isolation mass is sufficient for pebble gap formation; this may or may not coincide with an opening of a gap in the gas disk. The following are the main conclusions of the presented work, that are also summarized by the schematic in Figure 49:

1. The radius of transition between viscous heating and passive irradiation appears to dictate the most favorable radii for formation of the first protoplanets. It is at $r_{\rm vp}$ that any forming protoplanetary core is able to attain pebble isolation mass in the shortest duration, concurrent with the minimum $t_{\rm gap}$ in the Figures.

2. In a disk around a G-dwarf (eg., the Sun), $r_{\rm vp} \sim r_{\rm snow}$, implying that the first protoplanets may form at the water snow line itself.

3. In disks around M and A stars, $r_{\rm vp} < r_{\rm snow}$, implying that the first protoplanets in these disks may form within the snow line.

4. This scenario does not preclude the existence of massive cores interior to the gap. Rather, it is unlikely that these cores are able to attain pebble isolation mass and thereby form a gap in the denser more massive inner disk, especially as the first planet to form may cutoff the inward flow of pebbles. Planetary embryos form in the inner disk also may be unlikely to survive rapid Type-I migration, and may be lost to the star.

4.4 Future Work

We plan to undertake detailed numerical simulations of water transport in disks around M, G and A stars, to understand what may be the consequences to volatile transport of forming a gap within the snow line in disks around M and A stars, epsecially to test the hypothesis of Morbidelli et al. (2016) that the formation of the

first planet to open a pebble gap may starve its disk's inner regions of drifting ice particles. In the present study, we have assumed that pebble accretion occurs in the 2D regime and that migration of the protoplanetary core can be ignored. These assumptions would require further investigation to test their validity.

Chapter 5

CONCLUSIONS AND FUTURE WORK

This chapter summarizes the main conclusions of the research work presented in this thesis. I end with a discussion of some potential future research that I plan to undertake in my career.

5.1 Conclusions of Presented Work

5.1.1 Effect of α and Photoevaporation

Chapter II (Paper I) investigates the effect of both variable α and external photoevaporation (due to the presence of a nearby massive star) on the density structure of the disk, as well as its evolution over several Myr. The main conclusions of this work are highlighted below:

Non-uniform α disks have different density structures

In Figure 16, one sees the striking changes that different radial α profiles produce in the density structure of the disk. In plot (a), one can note that a globally constant $\alpha = 3 \times 10^{-4}$ produces a smooth and shallow $\Sigma(r)$ profile with a slope $p \sim 1$ in the 1 - 20 AU planet forming region. In plot (b) of the same figure, an MRI-α profile with an active inner disk and a radially increasing α profile (discussed in detail in Paper I) is seen to result in a disk with a depleted inner disk and a steep slope for the outer disk. In plot (c), a radially decreasing α profile results in a disk with an almost flat $\Sigma(r)$ as far as 20 AU. Here, we note that plot (b) reveals a structure similar to that of a transition disk, as pointed out by Pinilla et al. (2016).

Without the knowledge of what physical mechanism is responsible for angular momentum transport in the disk, disk evolution models have for a long time adopted a globally uniform α. $\Sigma(r)$ profiles used for comparison with observations are taken to be smooth monotonic power laws with an exponential taper near the disk edge (Andrews et al. 2009). So far, this assumption has worked very well, as it has only been possible to observe resolved disk structure for radial regions greater than $\sim$ tens of AU. $\Sigma(r)$ in the innermost few AU disk may help reveal more of the physical mechanism that drives accretion. A steep slope may betray a radially increasing $\alpha(r)$ and therefore a disk probably driven by the MRI; a shallow slope or flat $\Sigma(r)$ may reveal a radially decreasing α profile possible in a wind-driven disk.

Protoplanetary disks with non-uniform α may have steeper density profiles

Lower α in the inner disk may lead to a structure where mass piles up in the central regions of the disk. This gives rise to steep Σ profiles with $p > 2-3$ in the outer disk.

External Photoevaporation pushes the transition radius inward

In a viscously evolving disk, the transition radius ($r_{\rm trans}$; where the bulk mass flow switches direction from inward into the star to outward) moves outward with time. This is a consequence of the conservation of angular momentum; momentum lost due to disk mass accreting onto the central rotating star is balanced by the momentum gained by a small mass of the disk transported far outwards. A photoevaporated disk sees mass removed from the outer edge of the disk. As a consequence, the viscously evolving disk is not only truncated in size, $r_{\rm trans}$ is pushed inward. This is an interesting behavior observed in the photoevaporated disk, which may have interesting implications for the transport of volatiles in the protoplanetary disk. For example, if $r_{\rm snow} > r_{\rm trans}$, then significant quantities of water vapor may be drawn out

from the outer edge of the disk by external photoevaporation, potentially dehydrating the inner disk.

Externally Photoevaporated Disks have steeper density profiles

Because $r_{\rm trans}$ moves inward in a photoevaporated disk, mass in such disks are shuffled such that photoevaporated disks can have steeper density profiles in the outer regions where planets may form, i.e., between 1-30 AU. Steeper slopes may provide ample mass for planet formation closer in, but little mass for planets further out. Disks with such steep slopes may probably have more exoplanets in close-in orbits.

5.1.2 Water Transport and α

Water exists both as vapor within the water snow line, and as ice on solids outside of it. Vapor diffuses most quickly across a sharper concentration gradient, while particles drift in the direction of a negative pressure gradient. α determines how quickly water in each phase in transported at each r, interior and exterior to the snow line where each of these phases dominate. Moreover, the snow line is anything but stationary, and moves inward with time as mass accretion rates fall. All of these processes produce a complex radial distribution of water in the disk. The following are the main conclusions that emerge from research work presented in Chapter III (Paper II):

Water Transport in Disks with Different Global α Viscosity

1. Less viscous disks show sharper volatile gradients at the snow line, with a large but narrow peak in chondrule ice fraction just beyond the snow line.

2. More viscous disks show shallower volatile gradients at the snow line, with a small but broad peak of chondrule ice fraction just beyond the snow line.

3. As α influences the temperature in the inner disk and mass accretion rates, higher α allows for the snow line to sweep a larger region inward into the disk with time. This is likely to produce a more diverse population of asteroids with different water content.

4. Disks with lower α are able to retain local enhancements or depletions of water distribution in the disk. Such regions may lead to interesting localized disk chemistry.

5. The order of importance of the various factors determining the magnitude of the peak ice fraction in chondrules beyond the snow line is as follows: $a_{\rm chon} > t_{\rm growth} > \alpha > Sc > \kappa$, i.e., planetary properties are more important than disk properties. The order of importance of factors affecting the peack ice fraction in asteroids beyond the snow line is as follows: $\alpha > t_{\rm growth} >$ everything else. In other words, both disk and planetary parameters are both almost as important as the other. In determining the water content of planetesimals, the details of how planetesimals grow is at least as important as the traditionally investigated processes of how water is distributed in the disk.

Water Transport in Disks with radially varying α

1. Radially varying α profiles change the underlying gas structure in the disk significantly. Radial water distribution shaped by the transport processes that move vapor and ice in the gas disk are therefore significantly influenced by the gas density structure. Different $\alpha(r)$ profiles therefore give rise to distinct radial water distributions, with different peak ice fractions in chondrules and asteroidal bodies.

2. $\alpha(r)$ inspired by the MRI yields large ice-rock ratios in chondrules beyond the

snow line. In this disk, the snow line moves only a small distance inward.

3. $\alpha(r)$ inspired by a wind-driven disk yield smalls ice-rock ratios in chondrules beyond the snow line. In this disk, the snow line sweeps inward several AU in 5 Myr. Such a disk is also likely to produce a diverse population of asteroidal bodies with various amounts of water.

5.1.3 Formation of the First Planets via Pebble Accretion at the Water Snow Line

First Protoplanets form at active/passive transition radius in the disk

We find that it is at $r_{\rm vp}$ (where the disk transitions from being dominantly heated by accretion to dominantly heated by stellar irradiation) where protoplanets are able to form and grow large enough to open a gap (at least in the pebble distribution) in the shortest duration. Therefore, it is likely here where the first protoplanets are formed in the disk that can affect the overall system architecture.

In our numerical calculations, we find that for a G-dwarf disk, $r_{\rm snow} \sim r_{\rm vp}$, whereas for disks around both less and more massive stars, $r_{\rm snow} > r_{\rm vp}$. This suggests that while the first protoplanets perhaps form near the snow line around a G-dwarf, the first protoplanets may form well inside it around M and A stars. This has interesting implications for volatile content in planets around M and A stars, that should be thoroughly studied with numerical simulations of water transport in these disks.

5.1.4 Possible Observational Tests

$\Sigma(r)$ as a diagnostic for $\alpha(r)$

Though a crude proxy, $\Sigma(r)$ can yield considerable insight into the variation of α with radius. A radially increasing $\alpha(r)$ may betray a steep slope in Σ vs. r, while a decreasing $\alpha(r)$ may betray a very shallow slope in the Σ profile. $\Sigma(r)$ slopes

may therefore be insightful in confirming the dominant mode of angular momentum transport in the disk.

$c_{\rm vap}$ as a diagnostic for $\alpha(r)$

$c_{\rm vap}$ may also be another crude proxy for a radial variation in α in the warm inner disk within the snow line. We find a notable depletion (factor 2) in vapor content just before the snow line that may be observable in a disk driven by the MRI (CASE II; as can be noted in Figure 37a.)

5.2 Future Work

5.2.1 Transport of Water in Pre-transitional Disks around Different Stars

Recent research studies (eg. Morbidelli et al., 2016) suggest that gaps carved by the formation of massive planets beyond the water snow line are capable of inhibiting the continuous inward drift of icy pebbles. This would likely result in formation of relatively dry planets interior to the gap, even if they formed outside the snow line. Our own numerical study (presented in Chapter IV) has found that a gap may be formed by planets well within the snow line as well. Thorough numerical investigation is required to understand the possible consequences to water transport and distribution across the disk.

5.2.2 Water in Chondrites

A planned follow-up to D18, this work would investigate the transport of water in the disk model developed in D18 by incorporating the water transport implemented in work presented in Chapter III (Paper II) into this disk model. Our motivation will be to fit known constraints regarding water content in meteorites to an evolutionary

disk model.

5.2.3 Chemistry in Disks with Different Radially Varying α Profiles

Radially varying α may yield chemical signatures that may be more accessible for observations than direct measurements of turbulent broadening at different radii, which are already inherently difficult to perform. Coupling evolutionary disk models presented in this thesis with sophisticated disk chemistry models may yield interesting insights relating to chemistry in the disk.

5.2.4 Oxygen isotopes and variable α

Related to our understanding of the radial distribution of water, it is also important to study the radial distribution of oxygen isotopes, formed from the production of heavy water in the outer disk. Different isotopologues of CO ($C^{16}O$, $C^{17}O$ and $C^{18}O$) photodissociate with slightly varying dissociating wavelengths in the far-ultraviolet (FUV). FUV entering the surface layers of the disk dissociate much of the common $C^{16}O$ in the surface layers, but have to penetrate deeper to photolyze less abundant $C^{17}O$ and $C^{18}O$ molecules (Lyons & Young 2005). ^{17}O and ^{18}O atoms then immediately combine with H_2 to freeze out as heavy water ($H_2^{17}O$, $H_2^{18}O$) ice, which are then incorporated into chondrites and achondritic differentiated meteorites. Understanding the radial distribution of oxygen isotopes would provide another clue to the formation location of these bodies in the solar nebula. It would be interesting to understand how the distribution of O-isotopes may be affected with change in the FUV radiation environment.

5.2.5 Exploring Condensation Fronts of Other Volatiles

It would also be interesting to extend this work to other volatiles such as H_2S in the inner disk in order to investigate the origin of iron-rich enstatite chondrites. Troilite, a dominant Fe-bearing mineral in enstatite chondrites forms in reducing conditions when the inner disk is depleted in water vapor, from the solid-gas reaction of H_2S with Fe. Comparing timescales of diffusion and location of the chemical condensation front of H_2S and the water snowline may provide more insight into the formation of enstatite chondrites. I am also interested in including NH_3 into these investigations as the NH_3 condensation front in the disk is believed to be closely related to the H_2O condensation front in the nebula (Dodson-Robinson et al. 2009).

BIBLIOGRAPHY

Alexander, C. M. O., Barber, D. J., & Hutchison, R. 1989, Geochim. Cosmochim. Acta, 53, 3045

Alexander, C. M. O. '., Howard, K. T., Bowden, R., & Fogel, M. L. 2013, Geochim. Cosmochim. Acta, 123, 244

Anderson, K. R., Adams, F. C., & Calvet, N. 2013, ApJ, 774, 9

Adams, F. C., Hollenbach, D., Laughlin, G., & Gorti, U. 2004, ApJ,611, 360

Adams, F. C., Proszkow, E. M., Fatuzzo, M., & Myers, P. C. 2006, ApJ, 641, 504

Adams, F. C. 2010, ARA&A, 48, 47

ALMA Partnership, Brogan, C. L., Pérez, L. M., et al. 2015, ApJl, 808, L3

Andrews, S. M., & Williams, J. P. 2005, ApJ, 631, 1134

Andrews, S. M., & Williams, J. P. 2007, ApJ, 659, 705

Andrews, S. M., Wilner, D. J., Hughes, A. M., Qi, C., & Dullemond, C. P. 2009, ApJ, 700, 1502

Andrews, S. M., Wilner, D. J., Hughes, A. M., Qi, C., & Dullemond, C. P. 2010, ApJ, 723, 1241

Ansdell, M., Williams, J. P., Manara, C. F., et al. 2017, AJ, 153, 240

Ansdell, M., Williams, J. P., Trapman, L., et al. 2018, ApJ, 859, 21

Armitage, P. J. 2007, ApJ, 665, 1381

Ataiee, S., Baruteau, C., Alibert, Y., & Benz, W. 2018, arXiv:1804.00924

Bai, X. N., & Stone, J. M. 2011, ApJ, 736, 144

Bai, X. N., & Stone, J. M. 2013, ApJ, 769, 76

Bai, X. N., Ye, J., Goodman, J., & Yuan, F. 2016, ApJ, 818, 152

Bai, X. N. 2013, Protostars and Planets VI Posters, 2

Bai, X. N. 2014, ApJ, 791, 137

Bai, X. N. 2015, ApJ, 798, 84

Bai, X. N. 2016, ApJ, 821, 80

Balbus, S. A., & Hawley, J. F. 1991, ApJ, 376, 214

Balbus, S. A., & Hawley, J. F. 1998, Reviews of Modern Physics, 70, 1

Baraffe, I., Chabrier, G., Allard, F., & Hauschildt, P. H. 2002, A&A, 382, 563

Beckwith, S. V. W., & Sargent, A. I. 1991, ApJ, 381, 250

Beckwith, S. V. W., Sargent, A. I., Chini, R. S., & Guesten, R. 1990, AJ, 99, 924

Bell, J. F., Davis, D. R., Hartmann, W. K., & Gaffey, M. J. 1989, Asteroids II, 921

Birnstiel, T., Dullemond, C. P., & Brauer, F. 2010, A&A, 513, A79

Bitsch, B., Lambrechts, M., & Johansen, A. 2015, A&A, 582, A112

Bitsch, B., Lambrechts, M., & Johansen, A. 2018, AAP, 609, C2

Blaes, O. M., & Balbus, S. A. 1994, ApJ, 421, 163

Bockelée-Morvan, D., Gautier, D., Hersant, F., Huré, J.-M., & Robert, F. 2002, A&A, 384, 1107

Bouvier, J., Alencar, S. H. P., Harries, T. J., Johns-Krull, C. M., & Romanova, M. M. 2007, Protostars and Planets V, 479

Chapman, C. R., & Salisbury, J. W. 1973, Icarus, 19, 507

Chiang, E. I., & Goldreich, P. 1997, ApJ, 490, 368

Chiang, E., & Laughlin, G. 2013, MNRAS, 431, 3444

Ciesla, F. J., & Cuzzi, J. N. 2006, Icarus, 181, 178

Ciesla, F. J. 2014, ApJl, 784, L1

Cieza, L. A., Casassus, S., Tobin, J., et al. 2016, Nature, 535, 258

Clarke, C. J., & Pringle, J. E. 1988, MNRAS, 235, 365

Clarke, C. J., & Pringle, J. E. 1993, MNRAS, 261, 190

Cleeves, L. I., Bergin, E. A., & Adams, F. C. 2014, ApJ, 794, 123

Cleeves, L. I., Bergin, E. A., Qi, C., Adams, F. C., &Oumlberg, K. I. 2015, ApJ, 799, 204

Crida, A., Morbidelli, A., & Masset, F. 2007, A&A, 461, 1173

Cuzzi, J. N., & Zahnle, K. J. 2004, ApJ, 614, 490

Cuzzi, J. N., Hogan, R. C., Paque, J. M., & Dobrovolskis, A. R. 2001, ApJ, 546, 496

Cuzzi, J. N., Davis, S. S., & Dobrovolskis, A. R. 2003, Icarus, 166, 385

Dauphas, N. 2017, Nature, 541, 521

Davis, A. M., & McKeegan, K. D. 2014, Meteorites and Cosmochemical Processes, 361

Davis, S. S. 2005, ApJ, 620, 994

DeMeo, F. E., & Carry, B. 2014, Nature, 505, 629

Desch, S. J. 2007, ApJ, 671, 878

Desch, S. J., Estrada, P. R., Kalyaan, A., & Cuzzi, J. N. 2017, ApJ, 840, 86

Desch, S. J., Kalyaan, A., & OD́. Alexander, C. M. 2018, ApJS, 238, 11

Dodson-Robinson, S. E., Willacy, K., Bodenheimer, P., Turner, N. J., & Beichman, C. A. 2009, Icarus, 200, 672

Draine, B. T., & Sutin, B. 1987, ApJ, 320, 803

Draine, B. T., Roberge, W. G., & Dalgarno, A. 1983, ApJ, 264, 485

Dullemond, C. P., & Dominik, C. 2004, A&A, 421, 1075

Estrada, P. R., Cuzzi, J. N., & Morgan, D. A. 2016, ApJ, 818, 200

Flaherty, K. M., Hughes, A. M., Rosenfeld, K. A., et al. 2015, ApJ, 813, 99

Flaherty, K. M., Hughes, A. M., Rose, S. C., et al. 2017, ApJ, 843, 150

Flaherty, K. M., Hughes, A. M., Teague, R., et al. 2018, ApJ, 856, 117

Flock, M., Nelson, R. P., Turner, N. J., et al. 2017, ApJ, 850, 131

Fromang, S., Terquem, C., & Balbus, S. A. 2002, MNRAS, 329, 18

Gail, H.-P. 2001, A&A, 378, 192

Gammie, C. F. 1996, ApJ, 457, 355

Garaud, P., & Lin, D. N. C. 2007, ApJ, 654, 606

Gillon, M., Jehin, E., Lederer, S. M., et al. 2016, Nature, 533, 221

Glassgold, A. E., Najita, J., & Igea, J. 1997, ApJ, 480,344

—. (Erratum) 1997, ApJ, 485, 920

Gomes, R., Levison, H. F., Tsiganis, K., & Morbidelli, A. 2005, Nature, 435, 466

Gradie, J., & Tedesco, E. 1982, Science, 216, 1405

Gressel, O., Turner, N. J., Nelson, R. P., & McNally, C. P. 2015, ApJ, 801, 84

Guillot, T., & Hueso, R. 2006, MNRAS, 367, L47

Guilloteau, S., Dutrey, A., Wakelam, V., et al. 2012, A&A, 548, A70

Gundlach, B., & Blum, J. 2015, ApJ, 798, 34

Haisch, K. E., Jr., Lada, E. A., & Lada, C. J. 2001, ApJL, 553, L153

Hartmann, L., Calvet, N., Gullbring, E., & D'Alessio, P. 1998, ApJ, 495, 385

Hayashi, C. 1981, Progress of Theoretical Physics Supplement, 70, 35

Henney, W. J., & O'Dell, C. R. 1999, AJ, 118, 2350

Hollenbach, D., & Adams, F. C. 2004, Debris Disks and the Formation of Planets, 324, 168

Hueso, R., & Guillot, T. 2005, A&A, 442, 703

Hughes, A. M., Wilner, D. J., Andrews, S. M., Qi, C., & Hogerheijde, M. R. 2011, ApJ, 727, 85

Hutchison, R., Alexander, C. M. O., & Barber, D. J. 1987, Geochim. Cosmochim. Acta, 51, 1875

Ida, S., & Makino, J. 1993, Icarus, 106, 210

Ida, S., & Guillot, T. 2016, A&A, 596, L3

Ida, S., Guillot, T., & Morbidelli, A. 2016, A&A, 591, A72

Ilgner, M., & Nelson, R. P. 2006, A&A, 445, 205

Jacquet, E., Piani, L., & Weisberg, M. K. 2017, Chondrules and the Protoplanetary Disk, 1963, 2001

Johansen, A., Oishi, J. S., Mac Low, M.-M., et al. 2007, Nature, 448, 1022

Johansen, A., & Lambrechts, M. 2017, Annual Review of Earth and Planetary Sciences, 45, 359

Kalyaan, A., Desch, S. J., & Monga, N. 2015, ApJ, 815, 112

Kenyon, S. J., & Bromley, B. C. 2004, Nature, 432, 598

Kley, W. 1999, MNRAS, 303, 696

Kley, W., & Nelson, R. P. 2012, ARA&A, 50, 211

Kobayashi, H., & Ida, S. 2001, Icarus, 153, 416

Kokubo, E., & Ida, S. 2002, ApJ, 581, 666

Kretke, K. A., & Lin, D. N. C. 2007, ApJl, 664, L55

Kuchner, M. J. 2004, ApJ, 612, 1147

Lada, C. J., & Lada, E. A. 2003, ARA&A, 41, 57

Lambrechts, M., & Johansen, A. 2014, A&A, 572, A107

Lambrechts, M., Johansen, A., & Morbidelli, A. 2014, A&A, 572, A35

Landry, R., Dodson-Robinson, S. E., Turner, N. J., & Abram, G. 2013, ApJ, 771, 80

Lee, U., Osaki, Y., & Saio, H. 1991, MNRAS, 250, 432

Lesniak, M. V., & Desch, S. J. 2011, ApJ, 740, 118

Lin, D. N. C., & Pringle, J. E. 1990, ApJ, 358, 515

Lynden-Bell, D., & Pringle, J. E. 1974, MNRAS, 168, 603

Lyons, J. R., & Young, E. D. 2005, Nature, 435, 317

Lyons, J. R., Bergin, E. A., Ciesla, F. J., et al. 2009, Geochim. Cosmochim. Acta, 73, 4998

Lyra, W., & Umurhan, O. 2018, arXiv:1808.08681

Lyra, W. 2014, ApJ, 789, 77

Machida, M. N., Kokubo, E., Inutsuka, S.-I., & Matsumoto, T. 2010, MNRAS, 405, 1227

Malygin, M. G., Klahr, H., Semenov, D., Henning, T., & Dullemond, C. P. 2017, A&A, 605, A30

Mann, R. K., Di Francesco, J., Johnstone, D., et al. 2014, ApJ, 784, 82

Marcus, P. S., Pei, S., Jiang, C.-H., & Hassanzadeh, P. 2013, Physical Review Letters, 111, 084501

Marcus, P. S., Pei, S., Jiang, C.-H., et al. 2015, ApJ, 808, 87

Marti, J., & Mauersberger, K. 1993, Geophys. Res. Lett., 20, 363

Mauersberger, K., & Krankowsky, D. 2003, Geophys. Res. Lett., 30, 1121

McCaughrean, M. J., & O'dell, C. R. 1996, AJ, 111, 1977

Meijerink, R., Pontoppidan, K. M., Blake, G. A., Poelman, D. R., & Dullemond, C. P. 2009, ApJ, 704, 1471

Min, M., Dullemond, C. P., Kama, M., & Dominik, C. 2011, Icarus, 212, 416

Mitchell, T. R., & Stewart, G. R. 2010, ApJ, 722, 1115

Monga, N., & Desch, S. 2015, ApJ, 798, 9

Morbidelli, A., Levison, H. F., Tsiganis, K., & Gomes, R. 2005, Nature, 435, 462

Morbidelli, A., Bitsch, B., Crida, A., et al. 2016, Icarus, 267, 368

Mottl, M., Glazer, B., Kaiser, R., & Meech, K. 2007, Chemie der Erde / Geochemistry, 67, 253

Najita, J. R., Carr, J. S., Pontoppidan, K. M., et al. 2013, ApJ, 766, 134

Najita, J. R., & Ádámkovics, M. 2017, ApJ, 847, 6

Nakamura, T., Noguchi, T., Tanaka, M., et al. 2011, Science, 333, 1113

Notsu, S., Nomura, H., Ishimoto, D., et al. 2016, ApJ, 827, 113

Notsu, S., Nomura, H., Ishimoto, D., et al. 2017, ApJ, 836, 118

Notsu, S., Nomura, H., Walsh, C., et al. 2018, ApJ, 855, 62

Oka, A., Nakamoto, T., & Ida, S. 2011, ApJ, 738, 141

Oppenheimer, M., & Dalgarno, A. 1974, ApJ, 192, 29

Ouellette, N., Desch, S. J., & Hester, J. J. 2010, ApJ, 711, 597

Pan, L., Desch, S. J., Scannapieco, E., & Timmes, F. X. 2012, ApJ, 756, 102

Paardekooper, S.-J., & Mellema, G. 2006, AAP, 453, 1129

Pinilla, P., Flock, M., Ovelar, M. d. J., & Birnstiel, T. 2016, A&A, 596, A81

Pinte, C., Dent, W. R. F., Ménard, F., et al. 2016, ApJ, 816, 25

Pollack, J. B., Hubickyj, O., Bodenheimer, P., et al. 1996, Icarus, 124, 62

Pontoppidan, K. M., Salyk, C., Bergin, E. A., et al. 2014, Protostars and Planets VI, 363

Pringle, J. E. 1981, ARA&A, 19, 137

Rafikov, R. R. 2017, ApJ, 837, 163

Raymond, S. N., & Cossou, C. 2014, MNRAS, 440, L11

Raymond, S. N., & Izidoro, A. 2017, Icarus, 297, 134

Ribas, Á., Bouy, H., & Merín, B. 2015, AAP, 576, A52

Ribas, I., Tuomi, M., Reiners, A., et al. 2018, Nature, 563, 365

Ros, K., & Johansen, A. 2013, A&A, 552, A137

Sano, T., Miyama, S. M., Umebayashi, T., & Nakano, T. 2000, ApJ, 543, 486

Sasselov, D. D., & Lecar, M. 2000, ApJ, 528, 995

Schoonenberg, D., & Ormel, C. W. 2017, A&A, 602, A21

Scott, E. R. D., & Krot, A. N. 2014, Meteorites and Cosmochemical Processes, 65

Semenov, D., Henning, T., Helling, C., Ilgner, M., & Sedlmayr, E. 2003, A&A, 410, 611

Semenov, D., Wiebe, D., & Henning, T. 2004, A&A, 417, 93

Shakura, N. I., & Sunyaev, R. A. 1973, A&A, 24, 337

Silverberg, S. M., Kuchner, M. J., Wisniewski, J. P., et al. 2018, arXiv:1809.09663

Simon, J. B., Hughes, A. M., Flaherty, K. M., Bai, X.-N., & Armitage, P. J. 2015, ApJ, 808, 180

Simon, J. B., Bai, X.-N., Flaherty, K. M., & Hughes, A. M. 2017, arXiv:1711.04770

Stevenson, D. J., & Lunine, J. I. 1988, Icarus, 75, 146

Stoll, M. H. R., & Kley, W. 2014, A&A, 572, A77

Suzuki, T. K., Ogihara, M., Morbidelli, A., Crida, A., & Guillot, T. 2016, A&A, 596, A74

Takeuchi, T., & Lin, D. N. C. 2002, ApJ, 581, 1344

Teague, R., Guilloteau, S., Semenov, D., et al. 2016, A&A, 592, A49

Trujillo, C. A., & Brown, M. E. 2001, ApJl, 554, L95

Tsiganis, K., Gomes, R., Morbidelli, A., & Levison, H. F. 2005, Nature, 435, 459

Turner, N. J., Fromang, S., Gammie, C., et al. 2014, Protostars and Planets VI, 411

Umebayashi, T., & Nakano, T. 1981, PASJ, 33, 617

Umebayashi, T., & Nakano, T. 2009, ApJ, 690, 69

Unterborn, C. T., Desch, S. J., Hinkel, N. R., & Lorenzo, A. 2018, Nature Astronomy, 2, 297

van der Marel, N., van Dishoeck, E. F., Bruderer, S., Pérez, L., & Isella, A. 2015, AAP, 579, A106

van der Marel, N. 2017, Astrophysics and Space Science Library, 445, 39

Wadhwa, M., Amelin, Y., Davis, A. M., et al. 2007, Protostars and Planets V, 835

Walsh, K. J., Morbidelli, A., Raymond, S. N., O'Brien, D. P., & Mandell, A. M. 2011, Nature, 475, 206

Dreibus, G., & Wänke, H. 2001, Meteoritics and Planetary Science Supplement, 36, A51

Warren, P. H. 2011, Geochim. Cosmochim. Acta, 75, 6912

Weidenschilling, S. J. 1977, MNRAS, 180, 57

Weidenschilling, S. J. 1977, Ap&SS, 51, 153

Wu, J., Desch, S. J., Schaefer, L., et al. 2018, JGR: Planets, 123, 2691

Xu, Z., Bai, X.-N., & Murray-Clay, R. A. 2017, ApJ, 847, 52

Yang, L., & Ciesla, F. J. 2012, Meteoritics and Planetary Science, 47, 99

Youdin, A. N., & Goodman, J. 2005, ApJ, 620, 459

Youdin, A. N., & Lithwick, Y. 2007, Icarus, 192, 588

Zhang, K., Pontoppidan, K. M., Salyk, C., & Blake, G. A. 2013, ApJ, 766, 82